Journal Pre-proof

How many subductions in the Variscan orogeny? Insights from numerical models

Regorda Alessandro, Jean-Marc Lardeaux, Manuel Roda, Anna Maria Marotta, Maria Iole Spalla

PII: S1674-9871(19)30200-2

DOI: https://doi.org/10.1016/j.gsf.2019.10.005

Reference: GSF 900

To appear in: *Geoscience Frontiers*

Received Date: 24 January 2019

Revised Date: 26 August 2019

Accepted Date: 8 October 2019

Please cite this article as: Alessandro, R., Lardeaux, J.-M., Roda, M., Marotta, A.M., Spalla, M.I., How many subductions in the Variscan orogeny? Insights from numerical models, *Geoscience Frontiers*, https://doi.org/10.1016/j.gsf.2019.10.005.

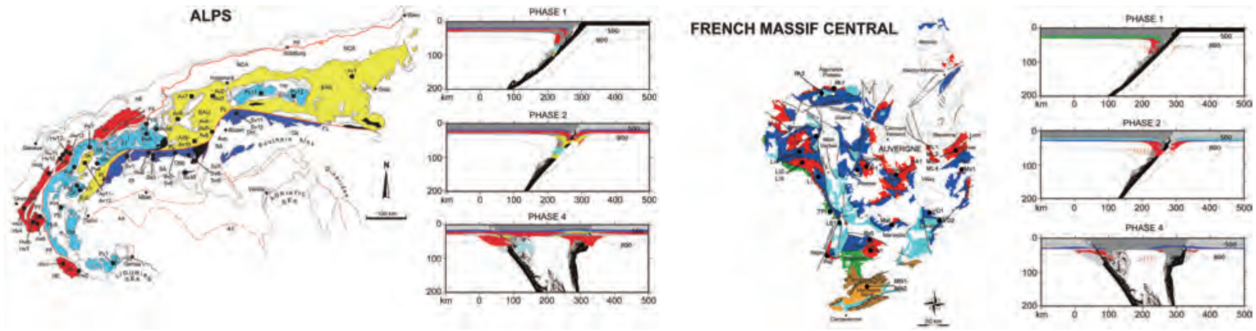

ALPS
PHASE 1
PHASE 2
PHASE 4
km
0
100
200
300
400
500
FRENCH MASSIF CENTRAL
AUVERGNE

How many subductions in the Variscan orogeny? Insights from numerical models

Regorda Alessandro[a,*], Jean-Marc Lardeaux[b], Manuel Roda[a], Anna Maria Marotta[a], Maria Iole Spalla[a]

[a] *Università degli Studi di Milano, Dipartimento di Scienze della Terra 'A. Desio', via Mangiagalli 34, I-20133 Milano, Italy*

[b] *Université Nice Sophia-Antipolis, UMR Geoazur, 250 Rue A. Einstein, Sophia-Antipolis, 06560, Valbonne, France*

* Corresponding author. E-mail address: alessandro.regorda@unimi.it

Abstract

We developed a 2D numerical model to simulate the evolution of two superposed ocean-continent-ocean subduction cycles with opposite vergence, both followed by continental collision, aiming to better understand the evolution of the Variscan belt. Three models with different velocities of the first oceanic subduction have been implemented. Striking differences in the thermo-mechanical evolution between the first subduction, which activates in an unperturbed system, and the second subduction, characterised by an opposite vergence, have been enlighten, in particular regarding the temperature in the mantle wedge and in the interior of the slab. Pressure and temperature (P-T) conditions predicted by one cycle and two cycles models have been compared with natural P-T estimates of the Variscan metamorphism from the Alps and from the French Massif Central (FMC). The comparative analysis supports that a slow and hot subduction well reproduces the P-T

conditions compatible with data from the FMC, while P-T conditions compatible with data of Variscan metamorphism from the Alps can be reproduced by either a cold or hot oceanic subduction models. Analysing the agreement of both double and single subduction models with natural P-T estimates, we observed that polycyclic models better describe the evolution of the Variscan orogeny.

Key words: Alps; Double subduction; French Massif Central; Numerical modelling; Variscan orogeny

1 Introduction

The Variscan belt is the result of the Pangea accretion that most marks the European continental lithosphere from Iberian Peninsula to Poland (von Raumer et al., 2003; Lardeaux et al., 2014) and, as in all collisional belts, the debate on the number of oceans and subduction systems that have been active during the orogen formation is open (Pin, 1990; Faure et al., 1997; Franke et al., 2017). It is part of a 1000 km broad and 8000 km long Paleozoic mountain system (Matte, 2001) and results from the successive collision of Gondwana and Gondwana-derived microcontinents, such as Avalonia, Mid-German Crystalline Rise (MGCR) and Armorica, against Laurussia during Devonian–Carboniferous times (e.g. Giorgis et al., 1999; Matte, 2001; von Raumer et al., 2003; Marotta and Spalla, 2007; Compagnoni and Ferrando, 2010; Cocks and Torsvik, 2011; Edel et al., 2013; Lardeaux et al., 2014). The final convergence between the supercontinents of Laurussia, to the north, and Gondwana, to the south, was associated with an intensive deformation of the assembled Avalonia and Armorican terranes (Edel et al., 2013, 2018).

Avalonia comprises the northern foreland of the Variscan belt and is geologically well defined because it lies between major sutures: the Iapetus and the Tornquist Caledonian sutures to the north separating Avalonia from North America and from Baltica, respectively, and the Rheic Variscan suture to the south (Fig. 1). Avalonia drifted northward independently from Armorica during the Early Palaeozoic (Trench and Torsvik, 1991; Cocks and Torsvik, 2011), detaching from Gondwana during Ordovician times originating the Rheic Ocean, while the Iapetus closed southward and then northward by subduction beneath the Taconic arc of Newfoundland (Pickering, 1989). Armorica is not defined precisely on the basis of palaeomagnetic data, but it has been interpreted as a small continental plate between the northern Rheic suture and the southern Galicia-southern Brittany suture (Eo-Variscan suture, e.g. Faure et al., 2005; Fig. 1).

Two scenarios concerning the geodynamic evolution of the Variscan orogeny have been proposed:

(1) Monocyclic scenario: for some authors (e.g. Torsvik, 1998) Armorica remained more or less closed to Gondwana during its northward drift, from Ordovician to Devonian times, in agreement with the lack of biostratigraphic and paleomagnetic data that suggest a short-lived narrow oceanic domain, smaller than 500–1000 km (Matte, 2001; Faure et al., 2009; Lardeaux, 2014a). This type of geodynamic reconstruction assumes a single long-lasting south-dipping subduction of a large oceanic domain, as proposed for the Bohemian Massif (e.g. Schulmann et al., 2009, 2014; Lardeaux et al., 2014);

(2) Polycyclic scenario: this geodynamic scenario envisages two main oceanic basins opened by the successive northward drifting of two Armorican microcontinent (Pin, 1990; Faure et al., 1997; Franke et al., 2017) and closed by opposite subductions (Lardeaux, 2014a; Lardeaux et al., 2014; Franke et al., 2017), as suggested by the occurrence of HP/UHP metamorphism (approximately at 400 and 360 Ma) on both sides of the Variscan belt. The northern oceanic basin is identified as the Saxothuringian ocean, while the southern basin can be identified as the Medio-European (Lardeaux, 2014a; Lardeaux et al., 2014) or Galicia-Moldanubian (Franke et al., 2017) ocean. The width and the duration of the Medio-European oceanic domain are debated, due to discrepancies between metamorphic and paleo-geographic data. However, the duration of the southern ocean is testified by the records of low temperature (LT) and high to ultrahigh pressure (HP/UHP)

metamorphism produced under a low-thermal regime that last for at least 30 Myr, which implies the subduction of a significant amount of oceanic lithosphere. For the French Massif Central (FMC) many authors (e.g. Faure et al., 2005, 2008, 2009; Lardeaux, 2014a) proposed a Silurian north-dipping subduction of Medio-European ocean and the northern margin of Gondwana underneath a magmatic arc developed on continental crust of either the southern margin of Armorica or an unknown and lost microcontinent (e.g. the Ligerian arc; Faure et al., 2008), followed by a late Devonian south-dipping subduction of the Saxothuringian ocean. The evolution inferred from the pre-Alpine basement of the External Crystalline Massifs of the Western Alps has been interpreted as compatible with the one proposed for the FMC (Guillot et al., 2009).

Recently, Baes and Sobolev (2017) have demonstrated the possibility that a continental collision following the closure of an oceanic domain on a continental side can induce external compressional forces on the passive margin on the other continental side, with a consequent spontaneous initiation of a new subduction with opposite vergence. Numerical models characterised by multiple subductions have been widely studied (e.g., Mishin et al., 2008; Cizkova and Bina, 2015; Dai et al., 2018) to better understand geodynamics processes characterising complex subduction systems, such as the western Dabie orogen (Dai et al., 2018) and the Mariana-Izu-Bonin arc (Cizkova and Bina, 2015). On the other hand, there are few studies regarding the interaction of two opposite verging subductions and only for systems characterised by very distant subductions (Holt et al., 2017), without a focus on the thermo-mechanical processes of the mantle wedge. Numerical models characterised by two opposite verging ocean/continent subduction systems at short distance, have been developed for the first time and here proposed to verify if such a scenario better fit with Variscan P-T evolutions. Our discussion focuses at first on the main features characterising a first oceanic subduction; then we enlighten the effects of the velocity of this first subduction on the thermal state and on the dynamics of the system during a second oceanic subduction and the following continental collision.

P-T conditions inferred from Variscan metamorphic rocks of the Alps and the FMC have been compared with those predicted for different lithospheric markers by the different models of double subductions. For the comparison we used P_{max}-T_{Pmax} estimates because they are the most representative to investigate the interaction between two active oceanic subductions. Differences in the agreement with one subduction model are then discussed, to shed light on the more reliable scenario on the basis of the best fit with natural data from these two portions of the European Variscan belt.

2 Variscan geological outline of the ALPS and of the FMC

The main sections of the Variscan belt show opposite vergences of nappes and recumbent folds migrating toward external Carboniferous basins. Three sutures have been described on both sides of the belt (Fig. 1) and they consist of discontinuous ophiolitic massifs and/or HP/UHP metamorphic relics, mainly eclogitized metabasalts (Matte, 2001):

(1) On the southern side of the belt, the Galicia-Southern Brittany suture is located between the north Gondwana margin and the Gondwana-derived microcontinents runs from the Coimbra-Cordoba Shear Zone in central Iberia (CCSZ) to southern Brittany, northern FMC and further east to the southern Bohemian nappes. The CCSZ is considered as the root zone of the western Iberian nappes. In Southern Brittany, the South Armorican Shear Suture Zone (SASZ) partly superimposes on the Eo-Variscan suture that crops out in the Armorican massif as the Nort-sur-Erdre fault. Ophiolitic rocks are dated between 500 and 470 Ma and the HP/UHP metamorphism between 430 and 360 Ma (Matte, 2001). This suture may be related to a N–S suture, running from the French external Alps to Sardinia and interpreted as the root of W-verging pre-Permian nappes. The translation toward SW of the French external Alps from Northern Europe, in prolongation with the Bohemian Massif, is related to the dextral wrenching from Carboniferous to Permian times along a N030° strike-slip

fault, in response to oblique collision between Laurussia and Gondwana (Matte, 2001; Guillot et al., 2009; Edel et al., 2013);

(2) On the northern side of the belt, two sutures are relatively well defined from southern England, through Germany to Poland: the Teplà suture, located between the Saxothuringian domain and the southern Gondwana-derived fragments, and the Rheic suture, located between Avalonia and Armorica (Franke, 2000; Matte, 2001; Schulmann et al., 2009, 2014; Edel et al., 2013). They are interpreted as the roots of NW-transported nappes, showing HP/UHP metamorphism in the ophiolitic rocks of the Teplà suture and its continental foot-wall (Konopásek and Schulmann, 2005). The oceanic rocks are dated at around 450–500 Ma and the HP metamorphism took place between 380 and 330 Ma (Schulmann et al., 2005; Skrzypek et al., 2014; Will et al., 2018). The Rheic suture is considered as corresponding to a younger oceanic basin, which opened during Lower Devonian and closed during the Late Viséan (Franke, 2000; Matte, 2001; Edel et al., 2013).

2.1. Variscan tectono-metamorphic evolution in the Alps

The Alps (Fig. 2) are the product of the Tertiary continental collision between the Adriatic promontory of the African plate and the southern continental margin of the European-Iberian plate and extends from the Gulf of Genoa to the Vienna basin. South of Genoa the Alpine range stops, because it has been fragmented during the opening of the Neogene Ligurian-Provencal-Algero basin and Late Neogene Tyrrhenian basin (e.g. Cavazza and Wezel, 2003; Dal Piaz et al., 2003; Dal Piaz, 2010; Gosso et al., in press).

Most of the pre-Alpine continental lithosphere recycled during the Alpine subduction shows a pre-Mesozoic metamorphic evolution compatible with the evolution of the European Variscan belt (von Raumer et al., 2003; Spalla and Marotta, 2007; Spiess et al., 2010; Spalla et al., 2014; Roda et al, 2018a). von Raumer et al. (2003) suggested that the present day Alpine domains (Helvetic, Penninic, Austroalpine and Southalpine) were probably located along the northern margin of Gondwana. In many Alpine basement areas, polymetamorphic assemblages comparable to those of the contemporaneous European geological framework prevail, testifying a polyphase metamorphic evolution accompanied by nappe stacking during different periods (Stampfli et al., 2002; von Raumer et al., 2013; Roda et al., 2018b).

Pre-Alpine HP metaophiolite remnants described in Helvetic to Austroalpine domains (e.g. Miller and Thöni, 1995; Guillot et al., 1998; Nussbaum et al., 1998; Spalla et al., 2014; Roda et al., 2018a) indicate that segments of the Variscan suture zone, incorporating the records of oceanic lithosphere subduction, were included in the Alpine belt. Oldest ages of Variscan HP metamorphic imprints range from Silurian to Middle-Devonian (437–387 Ma) and HP-UHP rocks display ages up to Upper Missisipian (~330 Ma) (e.g. Ligeois and Duchesne, 1981; Latouche and Bogdanoff, 1987; Vivier et al., 1987; Paquette et al., 1989; Messiga et al., 1992; Guillot et al., 1998; von Raumer et al., 1999; Spalla and Marotta, 2007; Liati et al., 2009; Spalla et al., 2014) accounting for a long period characterised by transformation of metabasites into eclogites during oceanic subduction. The preserved witness of the oceanic crust is represented by the Chamrousse ophiolite, that escaped the HP conditions (Fréville et al., 2018 and refs. therein). In some portions of this pre-Alpine basement a subsequent recrystallisation under granulite facies conditions took place at about 340 Ma (Ferrando et al., 2008; Liati et al., 2009; Rubatto et al., 2010). P-T estimates of the Variscan metamorphism in the Alps are presented in Table 1. More details concerning the Variscan metamorphism in the different domains of the Alps are synthesised in Appendix A (Table A1).

2.2. Variscan tectono-metamorphic evolution in the FMC

The European basement of the Variscan Belt experienced a long-lasting evolution from Cambrian–Ordovician rifting to Carboniferous collision and post-orogenic thinning (Bard et al., 1980; Matte, 2001; Faure et al., 2005, 2008). In France, the Variscan Belt is well exposed in the FMC and

Armorican Massif, where two contrasted paleogeographic and tectonic domains are recognized. The Nord-sur-Erdre Fault in the Armorican Massif corresponds to the main tectonic contact separating the Armorican domain to the north and the Gondwana margin to the south (Eo-Variscan or Galicia-Southern Brittany suture) (Matte, 2001; Faure et al., 2008; Ballèvre et al., 2009). The FMC (Fig. 3) belongs to the western part of the Variscan chain and it is the largest area where Variscan metamorphic and plutonic rocks are exposed, with the entire massif attributed to the northern Gondwanian margin (Burg and Matte, 1978; Matte, 1986; Mercier et al., 1991; Faure et al., 2005, 2009). P-T estimates of the Variscan metamorphism in the FMC are presented in Table 2.

The FMC is a stack of metamorphic nappes, in which six main units are recognized, from the bottom to the top and from the south to the north (Ledru et al., 1989; Faure et al., 2009; Lardeaux et al., 2014; Lardeaux, 2014a): (1) the southernmost turbidites fore-land basin (middle to late Mississippian); (2) the Palaeozoic fold-and-thrust belt of the Montagne Noire area, composed of weakly metamorphosed sediments (early Cambrian to early Carboniferous); (3) the Para-autochthonous unit (PAU) over-thrusting the southern fold-and-thrust belt and metamorphosed under greenschist to epidote-amphibolite facies conditions; (4) the Lower Gneiss Unit (LGU), metamorphosed under amphibolite facies conditions; (5) the Upper Gneiss Unit (UGU), which experienced upper Silurian/lower Devonian to middle Devonian HP to UHP metamorphism, and characterised by the occurrence, in the lowermost part, of a bimodal association called 'Leptyno-Amphibolitic Complex' (LAC) that is interpreted as a subducted and exhumed Cambro–Ordovician ocean-continent transition (OCT); (6) the uppermost units are identified by the Brévenne and Morvan units in the eastern FMC and by the Thiviers-Payzac unit (TPU) in the western FMC. The tectonic architecture of the FMC can be well illustrated by three mainly NS-orientated cross-sections over the eastern, the central and western parts, through which the main metamorphic and tectonic stages can be reconstructed. A detailed description of the main units in the cross-sections of the FMC is in Appendix A (Table A2).

The stack of nappes recognised in the FMC is the result of successive tectonic and metamorphic stages. Considering the period from Silurian to Visean, which is the time span covered by our models, four stages can be distinguished:

(1) The D0 event is coeval with a Silurian–Early Devonian HP to UHP metamorphism recorded in the whole FMC in the eclogites of the LAC at pressures higher than 2 GPa and temperatures of 700–800 °C, as in the eclogites of Mont du Lyonnais (Lardeaux et al., 2001);

(2) The D1 event is coeval with a Middle Devonian metamorphism recorded in both the UGU and the LGU and associated to isothermal decompression in the western FMC and decompression with an increase of temperature in the eastern FMC, up to pressure of 0.7–1 GPa and temperatures of 650–750 °C, such as in the UGU of Mont du Lyonnais (Lardeaux et al., 2001) and in the LGU of southern Limousine (Faure et al., 2008);

(3) The D2 is a Late Devonian–Early Carboniferous event is coeval with the emplacement in the northeastern FMC of volcanic rocks (Morvan magmatic arc) and Brévenne-Beaujolais ophiolite. The relative position of the Morvan arc to the north and the Brévenne-Beaujolais back-arc to the south argues for a south-dipping subduction;

(4) The D3 event is coeval to low- and very low-grade Visean metamorphism and the progressive exhumation of the tectonic units previously involved in the nappe stack, with the exception of high temperatures recorded in the southern and southeastern FMC.

3 Model setup

The proposed models of two opposite subductions (now on "models DS") simulate the thermo-mechanical evolution of an ocean/continent/ocean/continent subduction complex during four tectonic phases over a period of 130 Myr (Fig. 4):

(1) a first active oceanic subduction (phase 1) that lasts 51.5 Myr (from 425 to 373.5 Ma), until the continental collision, and characterised by three different velocities of plate subduction O1: 1, 2.5 and 5 cm/yr;

(2) a post-collisional phase (phase 2), which lasts 10 Myr (from 373.5 to 363.5 Ma) and is controlled by sole gravitational forces;

(3) a second opposite active oceanic subduction (phase 3) that lasts 26.5 Myr (from 363.5 to 337 Ma), until the second continental collision, with a prescribed velocity of 5 cm/yr of plate O2;

(4) a final post-collisional phase (phase 4) that lasts 42 Myr (from 337 to 295 Ma) and, as phase 2, is controlled by sole gravitational forces.

The time span covered by the four phases covers the same time span of one cycle model (now on "models SS") after Regorda et al. (2017), which is characterised by two tectonic phases: (1) an initial oceanic subduction (phase 1) lasting 51.5 Myr (from 425 to 373.5 Ma), with a prescribed velocity of 5 cm/yr; (2) a post-collisional phase (phase 2) lasting 78.5 Myr (from 425 to 295 Ma).

For what concerns phase 1 of models DS, the width of the oceanic domain involved in the first north verging subduction (plate O1), representing here the Medio-European ocean, is different for the three models. The oceanic domain is assumed to be 500, 1250 and 2500 km wide for velocities of 1, 2.5 and 5 cm/yr, respectively. The dimensions of the ocean for velocities of subduction of 1 and 2.5 cm/yr are compatible with the paleo-geographic reconstructions proposed for the FMC. The first subduction collision cycle consists of phases 1 and 2. The oceanic domain involved in the second subduction (plate O2 during phase 3), representing here the Saxothuringian ocean, is 1250 km wide in all models, according to a duration of the oceanic subduction of approximately 25 Myr (Lardeaux, 2014a; Lardeaux et al., 2014). The second subduction collision cycle consists of phases 3 and 4. The continent between the two oceanic domains (C3) is 400 km wide, in agreement with the dimension of Armorica inferred balancing the cross-sections through the Variscan belt in France

(Matte, 2001). The assumed time lag of 10 Myr between the first continental collision and the initiation of the second oceanic subduction (phase 2) is compatible with the results obtained by Baes and Sobolev (2017) concerning the spontaneous oceanic subduction initiation close to a continental collision.

For what concerns phase 1 of model SS, the oceanic domain involved in the long-lasting south-dipping subduction represents the Rheic ocean. Mono-cyclic scenarios of the Variscan orogeny suggest that a ~2500 km-wide ocean closed in approximately 50 Myr (Malavieille, 1993; Tait et al., 1997; Torsvik, 1998; von Raumer et al., 2003; Marotta and Spalla, 2007). Accordingly, we assumed a velocity of subduction of 5 cm/yr.

The list of acronyms and setup of the models are summarised in the insets in Fig. 4.

The physics of the crust-mantle system is described by the equations of continuity, of conservation of momentum and of conservation of energy, which include the extended Boussinesq approximation (e.g., Christensen and Yuen, 1985) for incompressible fluids. These equations are expressed as follows:

$$\nabla \cdot u = 0 \qquad (1)$$

$$-\nabla P + \nabla \cdot \tau + \rho g = 0 \qquad (2)$$

$$\rho c_p \left(\frac{\partial T}{\partial t} + u \cdot \nabla T \right) = \nabla \cdot (K \nabla T) + H_r + H_s + H_a \qquad (3)$$

where u is the velocity, P is the pressure, τ is the deviatoric stress, ρ is the density, g is gravity acceleration, c_p is the specific heat at a constant pressure, T is the temperature, K is the thermal conductivity, H_r is the radiogenic heating, $H_s = \tau_{ij} \dot{\epsilon}_{ij}$ is the heating due to viscous dissipation, $H_a = T\alpha \frac{DP}{Dt} \approx -\alpha T \rho g v_y$ is the adiabatic heating and α is the volumetric thermal expansion coefficient. Specific heat has been fixed to 1250 J kg^{-1} K^{-1} and the thermal expansion coefficient has bee fixed to $3 \cdot 10^{-5}$ K^{-1}.

Equations 1, 2 and 3 are numerically integrated via the 2D finite element (FE) thermo-mechanical code SubMar (Marotta et al., 2006), which uses the penalty function formulation to integrate the conservation of momentum equation and the Petrov-Galerkin method to integrate the conservation of energy equation. The numerical integration has been performed in a rectangular domain, 1400 km wide and 700 km deep (Fig. 4), discretized by a non-deforming irregular grid composed of 4438 quadratic triangular elements and 9037 nodes, with a denser nodal distribution near the contact region between the plates, where the most significant gradients in temperature and velocity fields are expected. The size of the elements varies horizontally from 10 to 80 km and vertically from 5 to 20 km, and smaller elements are located close to the active margin regions. To differentiate the crust from the mantle, we use the Lagrangian particle technique (e.g., Christensen, 1992) as implemented in Marotta and Spalla (2007), Meda et al. (2010) and Roda et al. (2010, 2012). At the beginning of the evolution, 288,061 markers identified by different indexes are spatially distributed at a density of 1 marker per 0.25 km^2 to define the upper oceanic crust, the lower oceanic crust and the continental crust. Material properties and rheological parameters are summarised in Table 3. During the evolution of the system, each particle is advected using a 4th-order Runge-Kutta scheme. Being $C_i^e = N_i^e / N_0^e$, with N_i^e the number of particles of type *i* inside the element *e* and N_0^e the maximum number of particles that element *e* can contain, the density of each element may be expressed as:

$$\rho^e(C^e, T) = \rho_0 [1 - \alpha (T - T_0)] - \sum_i \Delta\rho_i^e C_i^e \qquad (4)$$

where the index *i* identifies the particle type, ρ_0 is the reference density of the mantle at the reference temperature T_0, and $\Delta\rho_i^e$ is the differences between ρ_0 and the density of the upper oceanic crust, $(\Delta\rho_i^e = \rho_{oc_U} - \rho_0)$, of the ower oceanic crust, $(\Delta\rho_i^e = \rho_{oc_L} - \rho_0)$, and of the continental crust, $(\Delta\rho_i^e = \rho_{cc} - \rho_0)$.

Similarly, the viscosity of each element may be expressed as:

$$\mu^e(C^e, T) = \mu_m \left[1 - \sum_i C_i^e\right] + \sum_i \mu_i C_i^e \qquad (5)$$

with

$$\mu_i = \mu_{0,i}\, e^{\left[\frac{E_i}{R}\left(\frac{1}{T}-\frac{1}{T_0}\right)\right]} \qquad (6)$$

where $\mu_{0,i}$ is the reference viscosity at the reference temperature T_0, and E_i and n_i are the activation energy and the exponent, respectively, of the power law for the mantle, upper oceanic crust, lower oceanic crust and continental crust.

Free slip conditions have been assumed along the upper boundary of the 2D domain and no-slip conditions have been assumed along the other boundaries (Fig. 4). In addition, a velocity is prescribed along the bottom of the oceanic crust during the active subduction phase (O1 during phase 1 and O2 during phase 3). The same velocity is also prescribed along a 45° dipping plane that extends from the trench to a depth of 100 km to facilitate the subduction of the oceanic lithosphere. Differently, no velocities are prescribed during the two post-collisional phases (phases 2 and 4) and the system undergoes a pure gravitational evolution.

Fixed temperatures have been assumed at the top (300 K) and at the bottom (1600 K) of the model. Zero thermal flux is imposed at the vertical side-wall facing the subduction and fixed temperature along the opposite vertical side. The initial thermal structure corresponds to a conductive thermal gradient throughout the lithosphere, with temperatures that vary from 300 K at the surface to 1600 K at its base and a uniform temperature of 1600 K below the lithosphere. The base of the lithosphere is located at a depth of 80 km under both the oceanic and continental domains. This thermal configuration corresponds to either an oceanic lithosphere of approximately 40 Myr (based on the cooling of a semi-infinite half space model, Turcotte and Schubert, 2002) and a thinned continental passive margin based on a medium to slow spreading rate of 2–3 cm/yr (e.g., Marotta et al., 2016). The 1600 K isotherm defines the base of the lithosphere throughout the evolution of the system.

Models also account for mantle hydration associated to the dehydration of H_2O-satured MORB basalt, which transport water in their hydrous phases up to 300 km deep, as implemented in Regorda et al. (2017). The maximum depth at which dehydration takes place is identifiable by the depth of the deepest oceanic marker in the stability field of lawsonite. The progressive hydration of the mantle wedge is defined by the stability field of the serpentine (Schmidt and Poli, 1998). In the hydrated domains we assume a viscosity of 10^{19} Pa·s and a density of 3000 kg/m^3 (Schmidt and Poli, 1998; Honda and Saito, 2003; Arcay et al., 2005; Gerya and Stockhert, 2006; Roda et al., 2010).

4 Model predictions

Below, the presentation will focus initially on the first cycle of oceanic subduction and continental collision (phases 1 and 2, Chapter 4.1) and afterwards on the thermo-mechanics evolution characterising the second cycle of oceanic subduction and continental collision (phases 3 and 4, Chapter 4.2). Being the thermo-mechanic evolution of systems characterised by a single subduction activated in an unperturbed environment, widely described and discussed in a previous work of the same authors (e.g., Regorda et al., 2017), for phases 1 and 2 we will enlighten only the main features. For phases 3 and 4 we will enlighten differences in the dynamics and in the thermal state predicted by models characterised by different prescribed velocities of the first subduction. The thermal states predicted by models DS during phases 2, 3 and 4 will be then compared to the post-collisional phase of Regorda et al. (2017)'s model (SS.5 model).

4.1. First subduction-collision cycle (phases 1 and 2)

Results will be discussed in relation to three values of subduction velocities: 1, 2.5 and 5 cm/yr (models DS.1, DS.2.5 and DS.5, respectively). One major effect that deserves to be enlighten here is that the higher the velocity of subduction, the lower the temperature in the slab and in the mantle wedge (see isotherms 800 and 1100 K in Fig. 5), since cold material is buried more rapidly than it can be warmed by heat conduction, mantle convection, viscous heating or other heat sources. The consequence of the higher temperatures for lower velocities is that the area in which the P-T conditions are compatible with the stability field of the serpentine is smaller (blue areas in Fig. 5a–c) and the convective cells in the mantle wedge are less efficient for recycling subducted oceanic and continental crustal material. In particular, the slab of the first subduction of model DS.1 is characterised by temperatures too high to promote hydration in large domains of the mantle wedge and, therefore, recycling of subducted crust (see streamlines in Fig. 5a).

During phase 2, models evolve in a similar way regardless of the prescribed subduction velocity during phase 1 because their dynamics is controlled only by gravitational forces. Briefly, the large-scale convective flow gradually expands laterally towards the overriding plate, reducing the slab dip. At the same time, the convective flow underneath the upper continental plate disappears provoking a thermal re-equilibration in the entire system, with a warming of the subducted lithosphere and a cooling of the mantle wedge. The general dynamics is characterised by a rising of all the subducted material because of the lower density with respect to the surrounding mantle, which determines the doubling of the crust at the end of the phase 2.

4.2. Second subduction-collision cycle (phases 3 and 4)

The sinking of slab 2 determines a gradual backward bending of slab 1 (Fig. 6), associated to a thinning below a depth of approximately 150 km. The mantle flow above the slab is very weak, with the exception of model DS.5 in which it intensifies at about 15.5 Myr (Fig. 6b_3). The lack of an intense large-scale mantle flow in models DS.1 and DS.2.5 can be related to the presence of the slab 1 that prevents its activation. Differently, the mantle flow enhancing in model DS.5 after 15.5 Myr is ascribable to the higher dip angle of the slab with a consequent wider area available above it. In addition, the presence of the short-lived convective flow in the model DS.5 (Fig. 6b_3) determines an increase of temperature at the bottom of the slab 1 with respect to models DS.1 and DS.2.5 (Fig. 6b_1 and b_2, respectively) and a decrease of its dip. However, since large-scale mantle flow is limited above slab 2 and below slab 1, the area between the two subduction complexes is not thermally affected by the large-scale mantle flow, as occurs during phase 1. Differently, the large-scale convective cell below the second slab is of the same order of magnitude for all models and comparable with the flow activated during phase 1 below the slab 1 (Fig. 6).

Fig. 7 shows that at the beginning of the second active oceanic subduction (phase 3) the upper plate is still thermally perturbed. In particular, slab 1 is not yet thermally re-equilibrated, as shown by the depression of isotherms 1100 K (dashed lines in Fig. 7a). Comparing the isotherm 1100 K predicted by models DS.1, DS.2.5 and DS.5 during phase 3 inside slab 1 (dashed black, red and blue lines, respectively, in Fig. 7a and b) is evident that during the early stages model DS.5 is the coldest, while model DS.1 is the warmest. This is the consequence of the colder thermal state for higher velocities at the end of phase 1. During the early stages of phase 3, isotherms 800 K predicted by models DS.1, DS.2.5 and DS.5 in the micro-continent C3 show no differences (continuous black, red and blue lines in Fig. 7a and b, respectively) and they are shallower than in an unperturbed system (phase 1 of model SS.5, continuous green line in Fig. 7c and d). This because the geotherm at the beginning of phase 1 is colder than the geotherm at the beginning of phase 3 (Fig. 7a). Consequently, the difference between DS and SS models diminishes during the evolution (Fig. 7b) and it disappears in the latter stages of phase 3 (Fig. 7c and d). Further from the second subduction (x>250 km in Fig. 7), model DS.1 shows the lowest temperatures while model DS.5 is the warmest. This is due to the amount of continental material of the lower plate subducted during the collision (Fig. 6). In fact, for higher velocities of subduction (i.e. models DS.2.5 and DS.5) the larger amount of continental material subducted determined the thickening of the crust and the consequent higher temperatures due to higher radiogenic energy (see also Regorda et al., 2017).

For what concerns slab 2, the isotherm 800 K shows only a slight difference after 5.5 Myr, when it is slightly deeper in model DS.1 (continuous black line in Fig. 7b) with respect to models DS.2.5 and DS.5 (continuous red and blue lines in Fig. 7b, respectively). The thermal state begins to clearly differentiate after 15.5 Myr from the beginning of phase 3 (Fig. 7c), when isotherm 800 K is the deepest in model DS.1 and it is the shallowest in model DS.5. Further differences can be observed at the continental collision at the end of phase 3 (continuous lines in Fig. 7d), when model DS.5 (continuous blue line) is warmer than models DS.1 and DS.2.5 (continuous black and red lines) but is colder than model SS.5 (continuous green line). In the same way, 1100 K isotherm begins to show differences in the portion of the wedge close to the second subduction after approximately 15.5 Myr (dashed lines in Fig. 7c), with a colder thermal state for models DS.1, DS.2.5 and DS.5 (dashed black, red and blue lines, respectively) with respect to the phase 1 of model SS.5 (dashed green line). The colder thermal state in the wedge predicted during phase 3 could be related to the lack of heat supply due to the mantle flow that, in case of double subduction, does not reach the portion of the wedge close to slab 2. In correspondence of the doubled crust related to the first continental collision, isotherms 1100 K (dashed black, red and blue lines, respectively, in Fig. 7c and d) are shallower than the isotherm in a non-thickened crust (dashed green line in Fig. 7c and d), because of the higher energy supplied by radioactive decay.

Focusing on the wedge area (Fig. 8a, b and c for models DS.1, DS.2.5 and DS.5, respectively) we can observe that the local dynamics is comparable to that characterising phase 1, with slight differences due to the lower temperatures predicted during phase 3 inside slab 2. In fact, the hydrated area is more extended in models DS.1 and in DS.2.5 (blue areas in Fig. 8a$_1$ and b$_1$, respectively) with respect to model DS.5 (blue area in Fig. 8c$_1$), because of the colder thermal state and the consequent larger portion of mantle wedge in which the serpentine in stable. Differences in the extension of the hydrated area are more evident at the end of the subduction, when differences of the thermal conditions in the slab are more pronounced (blue areas in Fig. 8a$_2$, b$_2$ and c$_2$ for models DS.1, DS.2.5 and DS.5, respectively).

After the second continental collision, for all models the large-scale convective flow shows a decrease in the intensity below slab 2 of approximately two orders of magnitude (streamlines in Fig. 9). On the other hand, above slab 2 the activation of a feeble convective cell of the same order of magnitude occurs and it decreases its intensity at the end of phase 4 (streamlines in Fig. 9b$_1$, b$_2$ and b$_3$ for models DS.1, DS.2.5 and DS.5, respectively). The combined action of these two large-scale convective cells determines the increase of the dip angle of the deep portion of both subducted slabs. At the same time, both the subducted portion of the continental crust of the lower plate and the recycled material in the wedge rise to shallower depths, because of their lower densities with respect to the mantle.

The portion of the slab characterised by temperatures below 800 K thermally re-equilibrates by the first 10 Myr of phase 4, as shown by the isotherm 800 K (continuous black, red and blue lines in Fig. 7e and f) that does not show differences with respect to isotherm 800 K predicted by model SS.5 during phase 2 (green continuous line in Fig. 7e and f). Differently, isotherms 1100 K have different maximum depths for the models until the last stages of the evolution. In particular, isotherm 1100 K reach a depth of approximately 150 km in DS.1 model (black dashed line in Fig. 7f), more than 150 km in DS.2.5 model (red dashed line in Fig. 7f), of approximately 100 km in DS.5 model (blue dashed line in Fig. 7f) and of less than 100 km during phase 2 of SS.5 model (green dashed line in Fig. 7f). The slower thermal re-equilibration and the final colder thermal states of model DS.2.5 and, to a lesser extent, of models DS.1 and DS.5 with respect to model SS.5 are related to the lower temperatures predicted at the end of phase 3.

Fig. 10 shows differences in temperature, in terms of isotherms 800 (continuous lines) and 1100 K (dashed lines), between models DS.1, DS.2.5 and DS.5 (black, red and blue lines, respectively) and model SS.5 (green lines) after the first continental collision. Model SS.5 remains warmer than models DS.1, DS.2.5 and DS.5 during the whole evolution, due to the constant warming that characterises the post-collisional phase (phase 2) of model SS.5 (green lines in Fig. 10). Differently, phase 3 of models DS is characterised by a cooling of the subduction complex because of the activation of the second oceanic subduction (black, red and blue lines in Fig. 10a), followed by a thermal re-equilibration during phase 4 (black, red and blue lines in Fig. 10b).

5 Comparisons with natural P-T-t estimates

The P-T conditions estimated for rocks of the Variscan crust from the Alps and the FMC are compared with predictions of double subductions models, for the first subduction-collision cycle (phases 1 and 2, Chapter 5.1) and for the second subduction-collision cycle (phases 3 and 4, Section 5.2). We also enlighten the differences in the agreement with respect to model with a single subduction (Section 5.3) to infer the best fitting geodynamic scenario responsible for the building of the Variscan chain.

The French Massif Central is an example of a Silurian metamorphic evolution in relation with hotter subduction system (Lardeaux, 2014). The high thermal state inferred by natural data during the first Silurian–early Devonian subduction is in agreement with the thermal states predicted during phase 1 by models DS.1, DS.2.5 and DS.5, which is higher than that predicted during phase 3. However, model DS.1 does not show recycling of subducted crust during the first subduction and model DS.5 has a wider oceanic domain than that proposed by paleo-geographic reconstructions that consider two successive oceanic subductions. Therefore, assuming a geodynamic reconstruction for the Variscan orogeny characterised by two opposite subductions during Silurian–early Devonian and late Devonian–Carboniferous, model DS.2.5 appears as the most adequate to make a comparison with natural P-T estimates of the Variscan metamorphism recorded in the Alps and in the FMC.

The P-T conditions recorded by the markers of the models DS.2.5 and SS.5 have been compared with P_{max}-T_{Pmax} estimates related to the Variscan metamorphism inferred from both continental basement rocks of the Alpine domain (Table 1) and of the FMC (Table 2). The distribution of the data is represented in Figs. 2 and 3, respectively.

We assume that there could be a complete agreement between geological data and model predictions only if the following three conditions are satisfied contemporaneously:

(1) coincident lithological affinity with oceanic crust, continental crust and mantle;

(2) comparable P_{max}-T_{Pmax} estimates and P-T conditions predicted by the model. P-T estimates have different precisions; for example, the minimum pressure only has been

estimated for datum Pv1 from the Savona massif in the Penninic domain and datum Av9 from the Languard-Campo nappe in the Austroalpine domain, or the minimal pressure only has been estimated for datum ML1 from Mont du Lyonnais, while all data from the Southalpine domain in the Alps and from Rouergue in the FMC have more precise P-T estimates, including both minimal and maximal values;

(3) same ages of the P_{max}-T_{Pmax} estimates and the P-T conditions predicted by the model. Data in red in Fig. 11 have an estimated geological age, such as data Sv11 and Sv12 from the Eisecktal in the Southalpine domain and data Ar1 and Ar2 from Artense in the FMC; data in black have a radiometric well-constrained age, such as data Pv8 and Pv9 from the Adula nappe in the Penninic domain and data Li3, Li4 and Li5 from Limousin in the FMC. The latter more precise proposed ages make their fitting with model predictions more significant.

Data from the Alps will be discussed considering their distribution in the present domains (Helvetic, Penninic, Austroalpine and Southalpine domains) as in Fig. 2, while data from the FMC will be discussed considering their belonging to the main units recognised in the FMC (Upper Gneiss Unit, Lower Gneiss Unit, Para-autochthonous Unit, Thiviers-Payzac Unit and Montagne Noire) as showed in Fig. 3.

5.1. First subduction-collision cycle (phases 1 and 2)

The first subduction-collision cycle consists of phase 1, corresponding to a north verging oceanic subduction and lasting between 425 and 373.5 Ma (i.e. upper Silurian to Frasnian), and of the successive phase 2, controlled by sole gravitational forces and lasting between 373.5 and 363.5 Ma. These two phases can be related to deformation events D0 and D1 observed in the FMC.

5.1.1. Alps

Helvetic domain – Data Hv3 and Hv4 from Belledonne and data from Pelvoux (data Hv6 and Hv7) and Aiguilles Rouges (data Hv11 and Hv12) in the Helvetic domain that fit with the model predictions during phase 1 (Fig. 11a) recorded pressures over 0.8 GPa in a wide range of temperatures (between 530 and 930 °C) and have lithological affinities only with continental markers (brown and red points in Fig. 12a). During the early stages of phase 1, P_{max}-T_{Pmax} estimates fit with both subducted markers eroded by the upper plate, as samples Hv6 and Hv7 from Pelvoux and samples Hv11 and Hv12 from Aiguilles Rouges (Fig. 13a) and markers at the bottom of the crust of the upper plate, as sample Hv12 from Aiguilles Rouges (Fig. 13a), depending on their estimated pressure. Differently, no agreement with the oceanic markers occurs, because their predicted temperatures are too low (below 530 °C) for all the estimated P-T conditions in rocks from the Helvetic domain. Proceeding with the evolution, the upper plate warms up and markers in the deep portion of the crust start fitting with sample Hv4 from Belledonne (Fig. 13b–d), while sample Hv12 from Aiguilles Rouges fits only in the colder, internal and shallow portion of the wedge (Fig. 13b–d). During the last stages of phase 1 P-T values estimated from samples from Belledonne (Hv3 and Hv4), Pelvoux (Hv6) and Aiguilles Rouges (Hv11 and Hv12) agree also with the subducted portion of the lower continental plate (Fig. 13d).

Penninic domain – In the early stage of phase 1 there is correspondence between P-T values inferred from rocks of the Gran Paradiso massif (Pv3), Suretta (Pv10) and the Tauern window (Pv11 and Pv12) and model predictions (Fig. 11a). Pv3 estimated conditions from the Gran Paradiso massif are characterised by intermediate P/T ratio (Fig. 12b) and show the agreement with markers in the external and shallow portion of the wedge. Differently, data from Suretta (Pv10) and the Tauern window (Pv11 and Pv12) are characterised by high P/T ratio (Fig. 12b) and fit with markers either in the internal and shallow portion of the wedge, as estimates Pv11 from Suretta, or in the deeper portion, as estimates Pv10 and Pv12 from the Tauern window (Fig. 13a and b). In the second part of phase 1, data that fit with the model can be divided in two groups: the first group is composed by rocks with re-equilibrations characterised by intermediate P/T ratio, pressures below

0.8 GPa and temperatures between 530 and 630 °C (Fig. 12b), from the Gran Paradiso massif (Pv2, Pv3), Monte Rosa (Pv4) and the Grand St. Bernard nappe (Pv7); the second group is, instead, characterised by high P/T ratio, pressures above 1.8 GPa and temperature over 630 °C (Fig. 12b), from the Savona massif (Pv1), the Central Adula nappe (Pv8) and Suretta (Pv10). P-T values estimated from rocks of the first group show correspondences with continental markers in the shallow and external portion of the wedge, as Pv3 from the Orco valley in the Gran Paradiso massif (Fig. 13c and d) or at the bottom of the crust of the upper plate, as Pv2 from Gran Paradiso, Pv4 from Monte Rosa and Pv7 from the Grand St. Bernard nappe (Fig. 13c and d). Differently, P-T conditions inferred from rocks of the second group show an agreement with recycled oceanic and continental markers on the deep and external portion of the wedge, as in samples Pv1 from the Savona massif, Pv8 from the Central part of the Adula nappe and Pv10 from Suretta (Fig. 13c and d).

Austroalpine domain – Rocks from the Hochgrossen massif (Av1), the Silvretta nappe (Av7) and the Languard-Campo nappe (Av9) of the Austroalpine domain have recorded the peak of the Variscan metamorphism between 375 and 425 Ma (Fig. 11a) and they are characterised by high P/T ratios (Fig. 12c). All these data fit during phase 1 with deeply subducted oceanic and continental markers. In particular, data from the Hochgrossen and the Silvretta nappe (Av1 and Av7, respectively) have correspondences with oceanic and continental markers in the external portion of the wedge, during their recycling (Fig. 13b and c). In addition, at the end of phase 1, Av4 from the Tonale Zone fits both with the subducted portion of the lower plate and with recycled markers in the external portion of the wedge (Fig. 13d).

Southalpine domain – P-T conditions recorded in rocks from the Domaso-Cortafò Zone and the Eisecktal (Sv2 and Sv12, respectively) of the Southalpine domain were recorded under intermediate P/T ratios while those from Tre Valli Bresciane (Sv10) are characterised by high P/T ratio (Fig. 12d). Among these metamorphic records, the one from the Eisecktal (Sv12) has the lowest P/T ratio and it fits with markers in the deep portion of the crust of the upper plate (Fig. 13b–d) during phase

1. Differently, those from Sv10 of Tre Valli Bresciane have the highest P/T ratio and are in agreement with the model predictions characterising the external portion of the wedge, at a depth of about 45 km (Fig. 13d). Peak-conditions estimated from rocks of the Domaso-Cortafò Zone (Sv2) developed under a intermediate P/T ratio between those deriving from Tre Valli Bresciane and the Eisecktal estimates and find correspondences with markers at the bottom of the crust of the upper plate (deeper than Sv12 from the Eisecktal) and in the wedge, in a shallower area with respect to Sv10 from Tre Valli Bresciane (Fig. 13c and d). All of these estimated P-T values show an agreement also with the lower plate: metamorphic conditions available for the Domaso-Cortafò Zone and the Eisecktal fit with those predicted for continental markers in the deep portion of the non-subducted plate, while Sv10 from Tre Valli Bresciane fit with the thermal state predicted for continental markers in the subducted portion of the lower plate (Fig. 13d).

Given the short duration of the phase 2, the subduction complex is not completely thermally re-equilibrated and the thermal state is similar to that recorded at the end of phase 1. Then, all data from the Alps show the same agreement with the model with respect to phase 1 (Figs. 11a and 13e).

5.1.2 French Massif Central

Upper Gneiss Unit – In the early stage of phase 1, the model predictions show agreement only with data from the UGU (red dots in Fig. 14), in particular from Limousin (Li2), Mont du Lyonnais (ML1), Rouergue (Ro3), Artense (Ar1) and Maclas (Mc1, Fig. 11b). All of them are characterised by high P/T ratios, with pressures above 1.2 GPa and temperatures over 700 °C (Fig. 12e). With the exception of ML1 from Mont du Lyonnais, which consist of a garnet-bearing peridotite, therefore with mantle affinity, all the data fit both with continental subducted markers eroded from the base of the crust of the upper plate and with recycled oceanic markers (Fig. 14a). Proceeding with the evolution, both data from the UGU characterised by high P/T ratios, such as those from Limousin (Li2), La Bessenoits (LB1), Mont du Lyonnais (ML2), Rouergue (Ro2), Artense (Ar1) and Maclas (Mc1), and data from the UGU with intermediate P/T ratios, such as those from Limousin (Li5) and from Mont du Lyonnais (ML4), agree with the predicted thermal state (Fig. 11b). In particular, values characterised by intermediate P/T ratios find correspondences with continental markers at the bottom of the upper plate, while those characterised by high P/T ratios fit with both subducted and recycled markers (Fig. 14b–d). LB1 from La Bessenoits fits with subducted continental markers in the external portion of the slab (Fig. 14b), while Ma1 does not fit with predictions of the model even though is characterised by similar P-T conditions, because rocks in Maclas area have an oceanic affinity and in the model predictions no oceanic markers are located in the PT-field compatible with the natural data. On the other hand, datum Ro2 from Rouergue fit also with oceanic markers in the internal portion of the slab (Fig. 14c), characterised by a lower estimated temperature with respect to datum Ma1. Data from Limousin (Li2), Haut Allier (HA1), Artense (Ar1), Maclas (Ma1) and Mont du Lyonnais (ML2) have a high P/T ratio and temperatures higher than data LB1, Ma1 and Ro3. Consequently, they begin to fit with continuity after 25–30 Myr from the beginning (Fig. 14c–e), when there is an increase of crustal material in the external and warmer portion of the hydrated wedge. All data with intermediate-to-high and intermediate P/T ratios, such as PA1 from Plateau d'Aigurande, Ro3 from Rouergue, ML4 from Mont du Lyonnais and Li5 from Limousin, show a good fit at the bottom of the upper plate and in the external and shallower portions of the wedge during the second half of phase 1 (Fig. 14c). During phase 2, re-equilibration conditions of rocks from Artense (Ar1), Maclas (Mc1) and Rouergue (Ro1), characterised by high P/T ratios, continue to fit also with markers in the wedge, while P-T values characterised by intermediate P/T ratios, such as data ML4 and Ro3, fit at the bottom of the crust of both the upper and the lower plate (Fig. 14d and e).

Lower Gneiss Unit – Data from the LGU (blue dots in Fig. 14) with estimated geological ages compatible with phases 1 and 2 are only Li1 and Li4 from Limousin and Ar2 from Artense. Data Li1 and Ar2 are characterised by intermediate P/T ratios and fit with continuity during the entire phase 1 with continental markers at the bottom of the upper plate, up to the most internal and shallowest portion of the wedge (Fig. 14a–c). After the collision and during phase 2, datum Ar2 fits also with continental markers of the bottom of the lower plate (Fig. 14d and e). Datum Li4 is one of the two data characterised by high P/T ratio not in the UGU (the other is MN1 from Montagne Noire). It is also characterised by the highest P/T ratio and shows a very good fit with oceanic markers in the internal portion of the slab (Fig. 14b).

Para-autochthonous Unit – Only datum PA2 belonging to PAU from Plateau d'Aigurande has proposed ages compatible with phases 1 and 2 and it is characterised by intermediate P/T ratios. It has estimated ages compatible with the last stages of phase 1, fitting very well at the bottom of the upper plate, up to the most internal and shallowest portion of the wedge (Fig. 14). Moreover, PA2 continues to fit during the entire phase 2 at the bottom of the continental crust of both plates (Fig. 14d and e). Its fitting during D0 and D1 events is due both to uncertainty of age and to the PT conditions at the bottom of the upper plate that do not change significatly during the evolution of the model. In fact, it shows a fit also during phase 3 (D2 event).

5.2. Second subduction-collision cycle (phases 3 and 4)

The second subduction-collision cycle consists of phase 3, corresponding to a south verging oceanic subduction and lasting between 363.5 and 337 Ma (i.e. Famennian to lower Carboniferous), and the successive post-collisional phase 4, lasting between 337 and 295 Ma. These phases can be related to deformation events D2 and D3 observed in the FMC.

5.2.1. Alps

Helvetic domain – Estimated P-T values characterised by high P/T ratios (Fig. 12a), as Hv11 in Aiguilles Rouge, shows a good agreement both with continental markers scraped from the upper plate and subducted at the beginning of phase 3 (Figs. 11a and 15a) and with subducted continental markers of the lower plate after the continental collision (Figs. 11a and 15c). At the end of phase 3, the same fitting is shown also by Hv2, from Lake Frisson in Argentera, which is characterised by similar P-T conditions. However, neither Hv11 nor Hv2 fits only with markers involved in the second oceanic subduction. Similarly, data Hv3 from Belledonne and Hv12 from Aiguilles Rouge, that are characterised by intermediate-to-high P/T ratios, show a continuous fitting from the beginning of phase 3 (compatibly with their estimated ages, in Fig. 11a) with continental markers in the shallow portion of the wedge of the second active oceanic subduction (Fig. 15a–c). Differently, Hv6 from Pelvoux is characterised by a re-equilibration under an intermediate-to-high P/T ratio and temperature above 730 °C (Fig. 12a): at the beginning of phase 3 thermal conditions and lithologic affinities allow the fitting both with subducted markers in the shallow portion of the wedge related to slab 2 and with markers at a depth of approximately 50 km belonging to slab 1 (Fig. 15a). Successively, the temperature in the slab 2 decreases while it gradually increases in the slab 1; consequently, Hv6 from Pelvoux does not fit anymore with markers of slab 2 while it fits with shallower markers in slab 1 (Fig. 15b). Proceeding with the evolution of phase 3 and during phase 4, Hv6 fits gradually with a larger amount of markers (Fig. 11a) belonging to markers nearby the doubled crust in correspondence of both slabs (Fig. 15c–e). Moreover, Hv4 from Belledonne has intermediate P/T ratio and fits with markers at the bottom of the continental crust of all plates for the all duration of phase 3 and 4 (Figs. 11a and 15a–e). Data Hv3b, Hv4b and Hv4c from Belledonne are characterised by intermediate P/T ratios and fit with the model at the end of phase 3 and at the beginning of phase 4, therefore during the early phases of the continental collision, with continental markers in the proximity of the subduction complex. This is in agreement with the geodynamics reconstruction proposed by Fréville et al. (2018). Lastly, data Hv5 and Hv8 from Pelvoux have low-to-intermediate P/T ratios (Fig. 12a), therefore, they only fit in correspondence of the doubled crust related to the first subduction that, at the end of phase 4, is completely thermally re-equilibrated (Fig. 14d and e).

Penninic domain – Rocks from Gran Paradiso (Pv2 and Pv3), Monte Rosa (Pv4) and Grand St. Bernard (Pv5, Pv6 and Pv7) reveal conditions indicating intermediate P/T ratios, with temperatures below 730 °C, and their fit with the model predictions is uninterrupted during both phase 3 and 4, coherently with their estimated ages (Fig. 11a). In particular, during the first half of phase 3 they show fit with continental markers at the bottom of both plates and in the shallowest portion of the wedge related to the second subduction (Fig. 15a and b), while during the last stages of phase 3 and whole phase 4, they show fit with markers from the continental crust of all the three plates (Fig. 15d and e). Datum Pv8 from the Adula nappe is the only one characterised by a high P/T ratio (Fig. 12b) that finds correspondences with subducted markers of both slabs at the beginning of phase 3, when the system is not still completely thermally re-equilibrated (Fig. 15a). Proceeding with the evolution the first slab warms up and metamorphic conditions characterised by high P/T ratios, such as those of Adula and Suretta (Pv8 and Pv10) are in agreement only with those predicted for subducted and recycled markers in the second slab (Fig. 15b). At the collision, P-T values from rocks re-equilibrated under high P/T ratio (Pv9 and Pv10 from Adula and Suretta) accomplish the agreement only with markers belonging to the deeper portion of the subducted lower plate (Fig. 15c), while during last stages of phase 4 the agreement is with the thermal state of the recycled continental markers in the shallower portion of the wedge, after the thermal re-equilibration (Fig. 15d and e).

Austroalpine domain – Datum Av10 from Mortirolo is characterised by intermediate P/T ratio (Fig. 12c) and at the beginning of phase 3 fits only with shallow continental markers in the warmer portion of the hydrated wedge related to the second subduction (Fig. 15a). Proceeding with the evolution, the temperature in the wedge decreases while it increases in correspondence of the doubled crust of the first slab; consequently, Av10 cease to fit with continental markers nearby the second slab and begins to fit with thermally re-equilibrated markers of the first subduction (Fig. 15c and d). Variscan metamorphic rocks from the Dent Blanche nappe in the Austroalpine domain (data Av11 and Av12) reveal conditions marked by an intermediate P/T ratio (Fig. 12c) with an estimated age that correspond to the last stages of evolution of phase 4 (Fig. 11a) and they show fit with continental markers of the upper plate nearby slab 1 and slab 2, respectively (Fig. 15e). Data Av2 and Av3 from the Oetztal and Av4 from the Tonale Zone are characterised by high P/T ratios (Fig. 12c). Av4 is in good agreement with conditions predicted for markers in the external portion of the second slab at the beginning of phase 3 (Fig. 15a) and in the deep portion of the doubled crust during the first half of phase 3 (Fig. 15a and b). Differently, data Av2 and Av3 fit only with subducted markers of the second slab during the first half of phase 3, compatibly with their pressures (Fig. 15b).

Southalpine domain – All rocks from the Southalpine domain, with the exception of Sv10 (Fig. 12d), reveal conditions indicating intermediate P/T ratios, with temperatures below 730 °C. Their fit with the model predictions is continuous during both phase 3 and 4, compatibly with their estimated ages (Fig. 11a). In particular, during the first half of phase 3 they fit with continental markers at the bottom of both plates (Fig. 15a and b), while during the last stages of phase 3 and whole phase 4, they show fit with markers at the bottom of the continental crust of all the three plates (Fig. 15c–e). Datum Sv10 from Tre Valli Bresciane is characterised by high P/T ratio (Fig. 12d) and an estimated age compatible with the first half of phase 3 (Fig. 11a), showing compatibility only with subducted and recycled markers in the second slab (Fig. 15b).

5.2.2 French Massif Central

Upper Gneiss Unit – Rocks from Artense (Ar1), Maclas (Mc1), Rouergue (Ro1 and Ro3) are characterised by P-T conditions that reveal intermediate-to-high and high P/T ratios (Fig. 12e) and they fit with subducted and recycled crustal markers in the course of the second subduction only during the early stages of phase 3 (Figs. 11b and 16a, b). Moreover, Ro3 fits also both in correspondence of the deep portion of the doubled crust related to the first subduction during phases 3 and 4 (Fig. 16a–e), and in the subducted portion of the continental crust of the lower plate during phase 4 (Fig. 16c–e). Going on with the subduction, the temperature in the slab and in the wedge decreases and no rocks show fit with recycled markers in the mantle wedge related to slab 2. This is due to the higher temperatures characterising estimated P-T conditions from rocks of the FMC with respect to those from the Alps. On the other hand, the temperature in the doubled crust of the first slab increases gradually and data characterised by intermediate P/T ratios Mont du Lyonnais (ML3) fits at the bottom of the continental crust of the upper plate and in correspondence of the doubled crust related to the first slab (Fig. 16b).

Lower Gneiss Unit – Ar2 from Artense is characterised by an intermediate P/T ratio (Fig. 12e) and finds fitting at the bottom of the continental crust of the upper plate during phase 3 before the beginning of the continental collision (Fig. 16a and b), while after the collision (Fig. 16c–e) it shows fit at the bottom of the crust of the lower plate in correspondence of the second subduction and with the doubled thermally re-equilibrated crust related to the first subduction. Differently, data Li3 from Limousin and VD1 from the Velay Dome are characterised by low-to-intermediate P/T ratios (Fig. 12e) and do not show any fitting with the predictions of the model (Fig. 11b). This is because the model does not predict a sufficient increase of the temperatures at shallow depths following the continental collision.

Para-autochthonous Unit, Montagne Noire and Thiviers-Payzac Unit - Estimates with intermediate P/T ratios, such as TP1 from the Thiviers-Payzac unit, PA2 from Plateau d'Aigurande, VD2 from the Velay Dome and MN2 from Montagne Noire (Fig. 12e), show correspondences with the thermal state predicted for continental markers of the upper plate during phase 3 (Fig. 16a and b). Moreover, VD2 fits with continuity in the continental crust of all the three plates for the entire duration of phases 3 and 4 (Fig. 16a–e). MN1 from the Montagne Noire is characterised by a high P/T ratio (Fig. 12e) and does not find thermal and lithologic correspondences with the model.

5.3. Single subduction model

5.3.1. Alps

Helvetic domain – Data of the Helvetic domain show a worsening of the agreement with P-T predictions of model SS.5 with respect to model DS.2.5. In particular, data with estimated ages compatible with phase 1, continental affinities and temperatures above 650 °C, such as Pv6 and Pv7 from Pelvoux and Pv11 from Aiguilles Rouges (Fig. 17a), worsen their fit, because of the lower temperatures predicted in the slab and in the wedge by faster models. During the phase 2 of model SS.5, at approximately 350–365 Ma (beginning of phase 3 of model DS.2.5), data characterised by intermediate-to-high P/T ratios and continental affinities (Fig. 12a), such as Hv3 from Belledonne and Hv11 from Aiguilles Rouges, worsen their agreement (Fig. 17a). This because of the higher thermal state predicted by model SS.5, due to the post-collisional re-equilibration, with respect to the lower thermal state predicted in model DS.2.5, associated to the beginning of the second subduction. In fact, Hv3 and Hv11 show a fitting with DS.2.5 model only in correspondence of slab 2 but they do not show agreement with continental markers of slab 1 (Fig. 15a and b). In addition, at approximately 330–340 Ma (end of phase 3 of model DS.2.5) also Hv2 and Hv11 from the Argentera massif and Aiguilles Rouges, respectively, worsen their agreement with respect to model DS.2.5 (Fig. 17a). This occurs because both data are characterised by intermediate-to-high P/T ratios (Fig. 12a) but model SS.5 is almost completely thermally re-equilibrated and markers nearby the subduction complex are characterised by intermediate P/T ratios.

Hv8 from Pelvoux is the sole datum that improves its agreement with model predictions during the latest stages of evolution (phase 4 of model DS.2.5) because it is characterised by low P/T ratio, and the longer post-collisional thermal re-equilibration of model SS.5 with respect to model DS.2.5 determines higher temperatures in the subduction complex.

Penninic domain – During phase 1, Pv8, from the central part of the Adula nappe, and Pv10, from Suretta, worsen their agreement with P-T predictions of model SS.5 with respect to model DS.2.5 (Fig. 17a). Both of them are characterised by high P/T ratios (Fig. 12b), fitting with predictions of model DS.2.5 for continental subducted markers at different depths in the external portion of the hydrated wedge (Fig. 15–d); then the worsening of the agreement is due to the cooling for the higher velocities of subduction. Between 365 and 350 Ma and from 340 Ma to the end of the evolution (beginning and end of phase 3 in model DS.2.5, respectively) Pv9 and Pv10 from the nothern part of the Adula nappe and from Suretta, respectively, do not show fit with predictions of model SS.5 (Fig. 17a), differently than model DS.2.5. It occurs because of lack of high P/T ratios predicted by SS.5 model during the last part of the post-collisional phase.

Austroalpine domain – The lower thermal state characterising model SS.5 with respect of model DS.2.5 during phase 1 determines a worsening of the agreement of Av9 from the Languard-Campo nappe (Fig. 17a) that has a high P/T ratio and is characterised by high temperature (Fig. 12c). On the other hand, Av8 from Silvretta improves its agreement, being characterised by high P/T ratio but low temperature (Fig. 12c), so more compatible with the thermal state predicted for higher velocities of subduction. Between 365 and 350 Ma, Av2 and Av3 from Oetztal and Av5 from the Tonale Zone have a worse agreement with respect to model DS.2.5 (Fig. 17a), because they are characterised by high P/T ratios (Fig. 12c), which are not predicted by model SS.5 during the post-collisional phase. Av10 from the Languard-Campo nappe, characterised by intermediate P/T ratio, also worsen its agreement with predictions of model SS.5 (Fig. 17a) approximately 5–10 Myr from the beginning of phase 2. This occurs because its fit with predictions of model DS.2.5 occurs in correspondence of slab 1, which, in the early stage of phase 2, is warmer than for model SS.5.

Southalpine domain – The only PT value that shows differences in the agreement with predictions of model SS.5 and those of model DS.2.5 is Sv10, from Tre Valli Bresciane. Sv10 is characterised by high P/T ratio (Fig. 12d) and its fit worsen at beginning of phase 3 of model DS.2.5, between 365 and 350 Ma (Fig. 17a), when the initiation of the second subduction determines a cooling of the subduction system.

5.3.2 French Massif Central

Upper Gneiss Unit – As for P-T conditions estimated in the different present-day domains of the Alps, those from the FMC show a general worsening in the agreement with predictions of model SS.5 with respect to model DS.2.5. During phase 1, all data characterised by intermediate-to-high and high P/T ratios and temperatures above 650 °C, such as HA1 from Haut Allier, Li2 from Limousin, ML2 from Mont du Lyonnais, Ar1 from Artense, Ro3 from Rouergue and Mc1 from Maclas (Fig. 12e), worsen their agreement with model predictions (Fig. 17b with respect to Fig. 11b), because of the lower thermal state characterising slab 1 of model SS.5 with respect to model DS.2.5. In addition, rocks from Maclas (Mc1) and Artense (Ar1) worsen their agreement with model predictions also during the last stages of phase 2 with respect to phase 4 of model DS.2.5. In fact, during phase 4 of model DS.2.5 they fit with continental subducted markers of slab 2 in a portion of the wedge not completely thermally re-equilibrated, while the wedge during last stages of phase 2 of model SS.5 is completely re-equilibrated and only intermediate P/T ratios are predicted. Moreover, Ro3 decreases the number of markers with which has a compatibility (Fig. 17b with respect to Fig. 11b), because in model DS.2.5 it fitted both with continental markers in doubled crust of the first slab (as in model SS.5) and with subducted continental markers of the lower plate related to the second oceanic subduction. Lastly, data ML3 and ML4 from Mont du Lyonnais and Li5 from Limousin, characterised by intermediate P/T ratios, show the same fitting than in model DS.2.5 (Fig. 17b with respect to Fig. 11b), having compatibilities with continental markers at the bottom of the plates, where P-T conditions are not strongly affected by the second active oceanic subduction or by the velocity of subduction.

Lower Gneiss Unit, *Para-autochthonous Unit*, *Montagne Noire and Thiviers-Payzac Unit* – All data, with exception for Li4, show intermediate P/T ratios and show the same fitting with respect to model DS.2.5 (Fig. 17b with respect to Fig.11b). All of them, as for data ML3, ML4 and Li5 of the

UGU, fit with continuity at the bottom of the continental crust of all plates, as shown for example by the continuous fitting of PA2 from the PAU in the Plateau d'Aigurande throughout phases 1, 2 and 3 and of Ar2 from the LGU in the Limousin (Fig. 17b). Datum, Li4 from the LGU in the Limousin has a high P/T ratio but, as seen for data of the UGU, worses its fit with respect to model DS.2.5 (Fig. 17b with respect to Fig.11b). This behaviour is the same observed for data Av7 of the Austroalpine domain in the Alps and is due to the high estimated temperature for Li4 (650 °C) that is in contrast with the lower thermal state predicted in model SS.5 with respect to model DS.2.5.

6 Discussion

Three models of double subduction, identified by a first subduction phase (phase 1) with different prescribed velocities, have been developed to test if a model characterised by two opposite verging subductions may better represent the evolution of the Variscan orogeny with respect to a single subduction. Such approach allowed the analysis of the activation and the evolution of an oceanic subduction in a geodynamic scenario previously perturbed by an early subduction/collision history.

A main result is that, during phase 1 of double subduction models, differences in the thermal state inside the slab are influenced by differences in subduction velocities. In particular, a velocity decrease determines a temperature increase due to the lower amount of cold material subducted during the same time span. Then, the temperatures predicted by model DS.1 in the slab and in the mantle wedge result too high to have P-T conditions compatible with the stability field of serpentine. The consequence is that there is no hydration of the mantle wedge and therefore no activation of small-scale convective cells allowing the recycling of subducted material. On the contrary, the subduction velocity does not influence the thermal state of the upper plate.

In all models, large scale mantle flows activate during both oceanic subduction phases (phases 1 and 3), but during phase 3 it is less intense, due to the occurrence of the first slab constituting a barrier that prevents the large-scale mantle flow to reach the area between the two subducted slabs. The lack of the mantle flow up to the external boundaries of the hydrated area, and the consequent absence of its heat supply, determines a temperature decrease in the mantle wedge and in the slab interior. In particular, in all models slab 2 is colder than slab 1 of model DS.5, in which the first subduction has the same velocity as the second. During the second post-collisional phase there is an increase of the dip angle of both slabs.

Considering the polycyclic scenario proposed for the geodynamic evolution generating the Variscan chain, the most appropriate model to compare the predicted thermal evolutions with P-T conditions inferred for Variscan rocks from the Alps and the FMC appears to be model DS.2.5, taking both paleo-geographic and metamorphic evidences into account. In fact, model DS.5 is characterised by a wide ocean involved in the first subduction (2500 km), in contrast with paleo-geographic reconstructions suggesting a maximum oceanic width of 1000 km (e.g., Lardeaux, 2014a). On the other hand, DS.1 model is not accompanied by the hydration of mantle wedge and therefore does not show recycling of subducted material associated with the first subduction. Monocyclic scenarios account for a wide ocean (~2500 km) closing in ~50 Myr (Malavieille, 1993; Tait et al., 1997; Torsvik, 1998; von Raumer et al., 2003; Marotta and Spalla, 2007), so for the comparison with natural P-T estimates we used model SS.5.

The comparison with natural data shows a different agreement for rocks from the Alps and from the French Massif Central (Fig. 18). Metamorphic conditions recorded by the rocks with high P/T ratios from the Alps show a good agreement with P-T predicted in both hot and cold subductions, being characterised by both different metamorphic gradients and different estimated ages; some of them, such as Pv12, from the Penninic domain of the Tauern Window, and Av7, from the Silvretta nappe in the Austroalpine domain (see light blue and yellow dots in panels a2 and b2 of Fig. 18), have better correspondences with a hot subduction, such as phase 1 of model DS.2.5, while others, such as Pv8 and Pv10 from the central Adula and the Suretta nappes in the Penninic domain and Av2 from the Oetztal in the Austroalpine domain, with a cold subduction, such as phase 1 of model SS.5 and phase 3 of model DS.2.5 (see light blue and yellow dots in panels d2, e2 and f2 of Fig. 18). However, the present day distribution of Variscan records in the Alps is affected by Permian-

Triassic rifting, Jurassic oceanisation and a successive Alpine subduction and collision events that inhibits the reconstruction of a coherent geographic distribution of data.

Differently, data from the French Massif Central with high P/T ratios fit better with P-T predicted in hot subductions. In particular, data Mc1 and Ar1 from the UGU in Maclas and in Artense, respectively, worsen their agreement during both phase 3 of model DS.2.5 and phase 1 of model SS.5, with respect to phase 1 of model DS.2.5 (see red dots in panels a1 and b1 of Fig. 18). Moreover, data HA1, Li2, PA1, LB1, Ro3 and ML2 from the UGU and Li4 from the LGU worsen their agreement during phase 1 of model SS.5 with respect to model DS.2.5. This suggests that either a hotter subduction is necessary to develop P-T conditions compatible with these data or that the amount and accuracy of the available radiometric data are insufficient to propose a comparison between natural geological data and model predictions. In addition, we must say that some P-T estimates of the FMC of the early works should be refined with new methods of petrologic modeling to be more significant in the comparison with the models. On the other hand, it would be beneficial to determine the uncertainty of the models in order to reduce the ambiguity between different geodynamics settings (e.g. following the procedure proposed by Barzaghi et al., 2014; Marotta et al. 2015; Splendore et al., 2015).

The agreement of data characterised by intermediate P/T ratios is slightly influenced by the activation of the second subduction. This because they are compatible with P-T conditions predicted by the models at the bottom of the continental crust of the plates, where the second subduction does not have a significant impact on the thermal state. Therefore, only data characterised by high P/T ratios that have estimated ages compatible with phases 3 and 4 of model DS.2.5 are valid to discriminate between mono- and polycyclic scenarios.

Data with high P/T ratios from the Alps show a general improvement in their agreement with phases 3 and 4 of model DS.2.5 with respect to phase 2 of model SS.5. In particular, data Hv3 from Belledonne and Hv11 from Aiguilles Rouge in the Helvetic domain are characterised by intermediate-to-high P/T ratios and fit with continental markers in the shallow portion of the wedge related to the second subduction (see red dots in panels d2, e2 and f2 of Fig. 18); in addition, Pv10 from the Suretta nappe in the Penninic domain has a high P/T ratio and improve its agreement fitting with subducted markers in the deep portion of the second slab (see light blue dots in panels d2, e2 and f2 of Fig. 18). However, all these data have not precise geological ages, fitting with model D.2.5 from phase 1 to phase 4, and, consequently, they are not significant for the discrimination among the possible geodynamic scenarios. Similarly, datum Av3 from Oetztal in the Austroalpine domain is characterised by a high P/T ratio and improve its agreement during phase 3 of model DS.2.5 fitting in the shallow portion of the wedge of the second subduction (see yellow dots in panels d2 and e2 of Fig. 18). This datum has an estimated age with a narrower range and, therefore, is more significant than the previous data, even if it is a geological and not a radiometric age. Data Pv9 from the Adula nappe in the Penninic domain and Sv10 from Tre Valli Bresciane in the Southalpine domain have high P/T ratios and show a good improvement in model DS.2.5 during phases 3 and 4, fitting with subducted markers related to the second subduction (see blue dots in panels d2, e2 and f2 of Fig. 18). Their radiometric-measured ages make them more significant than the previous, suggesting that a polycyclic scenario is more appropriate for the geodynamic reconstruction of the Variscan orogeny. In general, the fitting improvement between predictions of model DS.2.5 and data from the Alps with an estimated age compatible with the beginning of phase 2 of model SS.5 and phases 3 and 4 of model DS.2.5 is related to the activation of the second subduction that produces a lower thermal state, more compatible with data characterised by intermediate-to-high and high P/T ratios. On the other hand, data Hv8 from Pelvoux in the Helvetic domain and Av10 from Mortirolo in the Austroalpine domain worsen the agreement in model DS.2.5, because a completely thermally re-equilibrated model better fit with data characterised by low-to-intermediate P/T ratios, such is the case in model SS.5 at the end of the evolution.

Few data from the FMC can help to discriminate among mono- and polycyclic scenarios. In particular, data Mc1 and Ar1 from the UGU in Maclas and in Artense are characterised by high P/T ratios and are the unique to show differences in the fit during phases 3 and 4 of model DS.2.5 with respect to phase 2 of model SS.5, having ages compatible with recycled markers in the wedge related to the second subduction (see red dots in panels d1, e1 and f1 of Fig. 18). However, both of them have not precise geological estimated ages, ranging between 295 and 425 Ma, and, therefore, they are not significant for geodynamic reconstructions of the Variscan orogeny. On the other hand, data with more accurate calculated ages compatible with phases 3 and 4 of model DS.2.5 neither fit nor show differences in the fit with the models. In particular, data with a complete agreement with both models (ML3 from the UGU in Mont du Lyonnais and VD2 and PA2 from the PAU in the Velay Dome and in the Plateau d'Aigurande, respectively) are characterised by intermediate P/T ratios and are compatible with P-T conditions at the bottom of the whole continental crust. The lack of data with high P/T ratios from the FMC in continuous agreement with the slab of the second subduction during phase 3 is in contrast with the good agreement during phase 1. In particular, data from the UGU, such as HA1 from Haut Allier, Li2 from Limousin, PA1 from Plateau d'Aigurande, LB1 form La Bessenoits and ML2 from Mont du Lyonnais, and from the LGU, such as Li4 from Limousin, have precise estimated ages and have a good fit during phase 1 with subducted and recycled markers of the first slab (see red dots in panels a1 and b1 of Fig. 18). This behaviour is in agreement with the geographic distribution of the data, because evidences of HP metamorphism related to the second subduction should be located further north than the FMC (see the Eo-Variscan suture in Fig. 18). In particular the suture lies either in the NW part of theArmorican Massif (Léon block) or in the Channel (Faure et al., 2005; Ballèvre et al., 2009; Faure et al., 2010), and, to the east, between North Vosges and Ardennes (Faure et al., 2010; Edel et al., 2018). Data from Montagne Noire must be discussed separately. Datum MN2 from Montagne Noire has an intermdiate P/T ratio and fits well during phase 4 with continental markers of upper plate (see orange dots in panel f1 of Fig. 18), then it could be related to D3 event developed in an intracontinental post-collisional setting. On the other hand datum MN1 is characterised by a high P/T ratio and it does not fit with our model. However, it can not be considered indicative because the discussion regarding the interpretation of the HP imprint is still open. Our results clearly highlight the fact that, nowadays, our understanding of Variscan orogeny is limited by a crucial lack of chronologic constraints on FMC metamorphic P-T paths.

Although the ocean-continent margins in our model do not include an OCT, data belonging to the UGU with accurate proposed ages compatible with the first subduction (HA1 from Haut Allier, ML2 from Mont du Lyonnais, Ro2 from Rouergue and PA1 from Plateau d'Aigurande; see red dots in panels a1, b1 and c1 of Fig. 18) show very good fitting with both continental markers eroded from the upper plate, representing here a magmatic arc developed on continental crust of either the southern margin of Armorica or an unknown and lost microcontinent (Faure et al., 2008; Lardeaux, 2014a), and oceanic markers of the lower plate, coupled at the trench and successively subducted and exhumed in the mantle wedge. Consequently, our model shows the possibility that rocks from the UGU could have an origin different from an OCT. This result opens a new perspective on the understanding of the pre-orogenic, Cambro-Ordovician, structural restoration of the FMC. Indeed, taking into account the consequences of thermal modelling presented above, in the FMC, as it is the case for more than two decades in the Alps (see discussions in Platt, 1986; Polino et al., 1990; Spalla et al., 1996; Schmid et al., 2004; Rosenbaum and Lister, 2005; Stöckhert and Gerya, 2005; Beltrando et al., 2010; Roda et al., 2012; Lardeaux, 2014b), the origin of high-pressure metamorphic rocks can be described in the framework of two significantly contrasted conceptual geodynamic models: (i) these rocks derive from a subducted OCT, thus from the lower plate, or (ii) they derive, at least in part, from the upper plate as the result of mass-transfers during ablative subduction.

7 Conclusions

We have investigated the thermo-mechanics of an oceanic subduction complex in a system perturbed by a previous ocean-continent subduction. Results from models of double subduction indicate that:

(1) there is a correlation between the thermal state of both the slab and the mantle wedge and the velocity of subduction; in particular lower temperatures can be observed for higher velocities of subduction. On the other hand, the velocity of subduction does not have a significant impact on the thermal state of the upper plate;

(2) high temperatures observed in the slowest model prevent the hydration of the mantle wedge, with a consequent lack of recycling of subducted material deriving both from the lower plate and from the continental margin of the upper plate;

(3) for same subduction velocities, the second subduction complex is colder than the first, due to the lack of large-scale mantle flow with the consequent heat supply.

From the successive comparison between thermal model predictions and natural Variscan P-T-t estimates from the Alps and the FMC results that:

(1) data from the Alps with high P/T ratios fit well with both hot and cold subductions, while data from the FMC with high P/T ratios have a better compatibility with hot subductions;

(2) some data from the Alps with high P/T ratios and accurate radiometric ages, compatible with a younger (Famennian to lower Carboniferous) subduction event, show a better fit with the double subduction model, suggesting that a polycyclic scenario is more suitable for the Variscan orogeny;

(3) the data of the FMC with high P/T ratios that show different fit in single and double subduction models have poorly constrained geological ages and, therefore, are not suitable to discriminate between mono- and polycyclic scenarios. This reflects also the fact that the high-pressure metamorphic rocks compatible with a Famennian to lower Carboniferous subduction event are located north of the FMC (e.g. in the NW part of the Armorican Massif Léon or even more likely in the Channel);

(4) considering the FMC, the compatibility of the model with data from the UGU open to the possibility that rocks of this unit could derive from tectonic erosion of the upper plate and not only from a lower plate OCT.

Acknowledgements

This work was partially supported by the MIUR-PRIN 2011 project (2010AZR98L) ‘Birth and death of oceanic basins: geodynamic processes from rifting to continental collision in Mediterranean and Circum-Mediterranean orogens’ and by the SISMA-Pilot Project ‘SISMA-Information System for Monitoring and Alert’ (ASI contract No. I/093/06/0). All of the figures were created using the Generic Mapping Tool (GMT) plotting software (Wessel and Smith, 1998). We thank the Editor Yoshida Masaki, Michel Faure and an anonymous reviewer for providing useful suggestions.

References

Afonso, J. C., Ranalli, G., 2004. Crustal and mantle strengths in continental lithosphere: is the jelly sandwich model obsolete? Tectonophysics 394, 221–232.

Arcay, D., Tric, E., Doin, M. P., 2005. Numerical simulation of subduction zones. Effect of slab dehydration on the mantle wedge dynamics. Physics of the Earth and Planetary Interiors 149, 133–153.

Baes, M., Sobolev, S. V., 2017. Mantle flow as a trigger for subduction initiation: a missing element of the Wilson Cycle concept. Geochemistry, Geophysics, Geosystems, DOI 10.1002/2017GC006962.

Ballèvre, M., Bosse, V., Ducassou, C., Pitra, P., 2009. Palaeozoic history of the Armorican Massif: Models for the tectonic evolution of the suture zones. Tectonics 341, 174-201.

Barbey, P., Villaros, A., Marignac, C., Montel, J.-M., 2015. Multiphase melting, magma emplacement and P-T-time path in late-collisional context: the Velay example (Massif Central, France). Bulletin de la Societe Géologique de France 186(2-3), 93–116.

Bard, J.-P., Burg, J.-P., Matte, P., Ribeiro, A., 1980. La chaîne hercynienne d'Europe occidentale en termes de tectonique des plaques. Mem. B.R.G.M. 108, 233–246.

Barzaghi, R., Marotta, A.M., Splendore, R., De Gaetani, C., Borghi, A., 2014. Statistical assessment of predictive modelling uncertainty: a geophysical case study. Geophysical Journal International 127, 22-32.

Bellot, J. P., Roig, J. Y., 2007. Episodic exhumation of HP rocks inferred from structural data and P-T paths from the southwestern Massif Central (Variscan belt, France). Journal of Structural Geology 29(9), 1538–1557.

Beltrando, M., Compagnoni, R., Lombardo, B., 2010. (Ultra-) High-pressure metamorphism and orogenesis: An Alpine perspective. Gondwana Research 18, 147-166.

Benciolini, L., Poli, M. M. E., Visonà, D., Zanferrari, A., 2006. Looking inside late Variscan tectonics: structural and metamorphic heterogeneity of the Eastern Southalpine basement (NE Italy). Geodinamica Acta 19(1), 17–32.

Berger, J., Féménias, O., Mercier, J.-C. C., Demaiffe, D. 2005. Ocean-floor hydrothermal metamorphism in the Limousin ophiolites (western French Massif Central): evidence of a rare preserved Variscan oceanic marker. Journal of Metamorphic Geology 23, 795–812.

Berger, A., Féménias, O., Ohnenstetter, D., Bruguier, O., Plissart, G., Mercier, J.-C. C., Demaiffe, D., 2010. New occurrence of UHP eclogites in Limousin (French Massif Central): Age, tectonic setting and fluid–rock interactions. Lithos 118, 365-382.

Bergomi, M. A., Dal Piaz, G. V., Malusà, M. G., Monopoli, B., Tunesi, A., 2017. The Grand St Bernard - Briançonnais nappe system and the Paleozoic inheritance of the Western Alps unravelled by zircon U-Pb dating. Tectonics 36, 2950-2972.

Bertotti, G., Siletto, G. B., Spalla, M. I., 1993. Deformation and metamorphism associated with crustal rifting: Permian to Liassic evolution of the Lake Lugano-Lake Como area (southern Alps). Tectonophysics 226, 271–284.

Best, M. G., Christiansen, E. H., 2001. Igneous Petrology, Blackwell Science, Oxford, 455 pp.

Bogdanoff, S., Ménot, R., Vivier, G., 1991. Les massif cristallins externes des Alpes occidentales françaises, un fragment de la zone interne varisque. Science Géologique Bullettin 44, 237–285.

Bonin, B., Brändlein, P., Bussy, F., Desmons, J., Eggenberger, U., Finger, F., Graf, K., Marro, C., Mercolli, I., Oberhänsli, R., Ploquin, A., von Quadt, A., von Raumer, J., Schaltegger, U., Steyrer, H. P., Visonà, D., Vivier, G., 1993. Late Variscan magmatic evolution of the Alpine basement. In: Von Rumer, J. F., Neubauer, F. (eds.), Pre-Alpine Basement in the Alps. Springer-Verlag, Heildelberg, pp. 171-201.

Borghi, A., 1989. L'evoluzione metamorfico-strutturale del settore nord-orrientale della Serie dei Laghi (Alpi Meridionali). PhD thesis, Università di Torino.

Borghi, A. 1991. Structural evolution of the north-eastern sector of the Serie dei Laghi (Southern Alps). Bollettino della Società Geologica Italiana 110, 639– 647.

Borghi, A., Gattiglio, M., Mondino, F., Zaccone, G., 1999. Structural and metamorphic evidence of pre-Alpine basement in the Ambin nappe (Cottian Alps, Italy). Memorie della Società Geologica Italiana 51(1), 205–220.

Boriani, A., Burlini, L., Sacchi, R. 1990. The Cossato-Mergozzo-Brissago line and the Pogallo line (Southern Alps, Northern Italy) and their relationships with late-Hercynian magmatic and metamorphic events. Tectonophysics 140, 193–212.

Boriani, A., Villa, I., 1997. Geochronology of regional metamorphism in the Ivrea-Verbano zone and Serie dei Laghi, Italian Alps. Schweizerische Mineralogische Und Petrographische Mitteilungen 77, 381–401.

Boutin, R., Montigny, R., 1993. Datation $^{39}Ar/^{40}Ar$ des amphibolites du complexe leptyno-amphibolique du plateau d'Aigurande: collision varisque à 390 Ma dans le Nord-Ouest du Massif central français. Compte Rendu Academie des Sciences de Paris 316, 1391–1398.

Brodie, K. H., Rex, D., Rutter, E. H., 1989. On the age of deep crustal extensional faulting in the Ivrea zone, Northern Italy. In: Coward, M. P., Dietrich, D., Park, R. G. (eds.), Alpine Tectonics. Geological Society, London, Special Publications, vol. 45, pp. 203-210.

Burg, J. P., Delor, C., Leyreloup, A., 1986. Le massif du Lévézou et les séries adjacentes du Rouergue Oriental. Nouvelles données pétrographiques et structurales. Bulletin du Bureau de Recherge Géologiques et Minières Série 2: Geologie de la France 3, 229-272.

Burg, J. P., Delor, C. P., Leyreloup, A. F., Romney, F., 1989. Inverted metamorphic zonation and Variscan thrust tectonics in the Rouergue area (Massif Central, France): P-T-t record from mineral to regional scale. In: Daly, J. S., Cliff, R. A., Yardley, B. W. D. (eds.), Evolution of Metamorphic Belts. Geological Society, London, Special Publication, vol. 43, pp. 423-439.

Burg, J.-P., Matte, P., 1978. A cross-section through the french Massif central and the scope of its Variscan geodynamic evolution. Z. Dtsch. Geol. Ges. 129, 429–460.

Bussy, F., Sartori, M., Thélin, P., 1996. U-Pb zircon dating in the middle Penninic basement of the Western Alps (Valais, Switzerland). Schweizerische Mineralogische Und Petrographische Mitteilungen 76, 81–84.

Carminati, E., Siletto, G. B., Battaglia, D., 1997. Thrust kinematics and internal deformation in basement-involved fold and thrust belts: The eastern Orobic Alps case (Central Southern Alps, northern Italy). Tectonics 16(2), 259-271.

Cassinis, G., Massari, F., Neri, C., Venturini, C., 1988. The continental Permian in the southern alps (Italy) - a review. Zeitschrift fur geologische Wissenschaften 16, 1117-1126.

Catalàn, J. R. M., 2011. Are the oroclines of the Variscan belt related to late Variscan strike-slip tectonics? Terra Nova 23, 241-247.

Cavazza, W., Wezel, F. C., 2003. The Mediterranean region - a geological primer. Episodes 26(3), 160-168.

Chenevoy, M., 1970. Carte Géologique de la France à 1/50.000, feuille de St Etienne. BRGM, Orléans.

Chopra, P. N., Peterson, M. S., 1981. The experimental deformation of dunite. Tectonophysics 78, 453–473.

Christensen, U. R., 1992. An Eulerian tecnique for thermo-mechanical model of lithospheric extension. Journal of Geophysical Research 97, 2015-2036.

Christensen, U. R., Yuen, D. A., 1985. Layered Convection Induced by Phase Transitions. Journal of Geophysical Research 90(B12), 10291-10300.

Cizkova, H, Bina, C.R., 2015. Geodynamics of trench advance: Insights from a Philippine-Sea-style geometry. Earth and Planetary Science Letters 430, 408–415.

Cocks, L. R. M., Torsvik, T. H., 2011.The Palaeozoic geography of Laurentia and western Laurussia: A stable craton with mobile margins. Earth-Science Reviews 106, 1-51.

Compagnoni, R., Ferrando, S., 2010. Paleo-European crust of the Italian western Alps: Geological history of the Argentera Massif and comparison with Mont Blanc–Aiguilles Rouges and Maures. Journal of the Virtual Explorer Electronic Edition 36(3), 1-32.

Costa, S., 1990. De la collision continentale à l'extension tardiorogénique: 100 millions d'années d'histoire varisque dans le Massif Central Français: Une étude chronologique par la méthode $^{40}Ar/^{39}Ar$. Ph.D. Thesis, Univ. Montpellier, 441 p.

Costa, S., Maluski, H., Lardeaux, J.-M., 1993. $^{40}Ar/^{39}Ar$ chronology of Variscan tectono-metamorphic events in an exhumed crustal nappe: the Monts du Lyonnais complex (Massif Central, France). Chemical Geology 105(4), 339–359.

Dai, L., Li, S., Li, Z-.H., Somerville, I., Suo, Y., Liu, X., Gerya, T.V., Santosh, M., 2018. Dynamics of exhumation and deformation of HP-UHP orogens in double subduction-collision systems:

Numerical modeling and implications for the Western Dabie Orogen. Earth-Science Reviews 182, 68–84.

Dal Piaz, G. V., 2010. Geological outline of the Alps, focusing on the Italian north-western side. In: Beltrando, M., Peccerillo, A., Mattei, M., Conticelli, S., Doglioni, C. (eds.), The Geology of Italy: tectonics and life along plate margins. Journal of the Virtual Explorer Electronic Edition, vol. 36(8), pp. 1-28.

Dal Piaz, G. V., Bistacchi, A., Massironi, M., 2003. Geological outline of the Alps. Episodes 26(3), 175-180.

Dale, J., Holland, T. J. B., 2003. Geothermobarometry, P-T paths and metamorphic field gradients of high-pressure rocks from the Adula Nappe, Central Alps. Journal of Metamorphic Geology 21(8), 813–829.

Delleani, F., Rebay, G., Zucali, M., Tiepolo, M., Spalla, M. I., 2018. Insights on Variscan geodynamics from the structural and geochemical characterization of a Devonian-Carboniferous gabbro from the Austroalpine domain (Western Alps). Ofioliti 43(1), 23-39.

Delor, C., Burg, J.P., Guiraud, M., Leyreloup, A., 1987. Les métapélites à phengite-chloritoïde-grenat-staurotide-disthène de la klippe de Najac-Carmaux: nouveaux marqueurs d'un métamorphisme de haute pression varisque en Rouergue occidental. Comptes Rendus de l'Académie des Sciences 305, 589–595.

Demange, M., 1985. The eclogite-facies rocks of the Montagne Noire, France. Chemical Geology 50(1-3), 173-188.

Desmons, J., Compagnoni, R., Cortesogno, L., Frey, M., Gaggero, L., 1999. Pre-Alpine metamorphism of the Internal zones of the Western Alps. Schweizerische Mineralogische Und Petrographische Mitteilungen 79, 23-39.

Desmons, J., and D. Mercier, 1993. Passing Through the Briancon Zone. In: von Raumer, J. F., Neubauer, F. (eds.), Pre-Mesozoic Geology in the Alps. Springer-Verlag, Heidelberg, pp. 279–296.

di Paola, S., 2001. Eredità litostratigrafica, strutturale e metamorfica paleozoica nel margine interno Europeo (Grandes Rousses e Argentera), ristrutturato durante l'orogenesi Alpina. Ph.D. Thesis, Università degli Studi di Milano and Université Claude Bernard Lyon.

di Paola, S., Spalla, M. I., 2000. Contrasting tectonic records in pre-Alpine metabasites of the Southern Alps (lake Como, Italy). Journal of Geodynamics 30(1-2), 167–189.

di Paola, S., Spalla, M. I., Gosso, G. 2001. New structural mapping and metamorphic evolution of the Domaso-Cortafò Zone (Southern Alps - Lake Como). Memorie di Scienze Geologiche 53, 1– 14.

Diella, V., Spalla, M. I., Tunesi, A., 1992. Contrasted thermo-mechanical evolutions in the South-alpine metamorphic basement of the Orobic Alps (Central Alps, Italy). Journal of Metamorphic Geology 10, 203–219.

Droop, G. T. R., 1983. Pre-Alpine eclogites in the Pennine Basement Complex of the Eastern Alps. Journal of Metamorphic Geology 1(1), 3–12.

Droop, G. T. R., Lombardo, B., Pognante, U., 1990. Formation and distribution of eclogite facies rocks in the Alps. In: Carswell, D. A. (ed.), Eclogite Facies Rocks. Blackie and Son Ltd, London, pp. 225-256.

Dubois, J., Diament, M., 1997. Gèophysique, Masson, Paris, 205 pp.

Dubuisson, G., Mercier, J.-C. C., Girardeau, J., Frison, J.-Y., 1989. Evidence for a lost ocean in Variscan terranesof the Western Massif Central, France. Nature 337, 729-732.

Ducrot, J., Lancelot, J. R., Marchand, J., 1983. Datation U-Pb sur zircons de l'éclogite de La Borie (Haut-Allier, France) et conséquences sur l'évolution ante-hercynienne de l'Europe occidentale. Earth and Planetary Science Letters 62(3), 385–394.

Dufour, E., 1982. Pétrologie et géochimie des formations ortho-métamorphiques acides des monts du lyonnais (Massif Central français). Ph.D. Thesis, Univ. Lyon 1, 241 pp.

Dufour, E., Lardeaux, J.-M., Coffrant, D., 1985. Eclogites ert granulites dans les Monts du Lyonnais: une èvolution métamorphique plurifaciale éohercynienne. Compte Rendu Academie des Sciences de Paris 300(4), 141–144.

Duguet, M., Le Breton, N., Faure, M., 2007. P–T paths reconstruction of a collisional event: The example of the Thiviers-Payzac Unit in the Variscan French Massif Central. Lithos 98, 210-232.

Duthou, J.L., Chenevoy, M., Gay, M., 1994. Age Rb/Sr Dévonien moyen des migmatites à cordiérite du Lyonnais (Massif Central français). Compte Rendu Academie des Sciences de Paris 319, 791-796.

Edel, J. B., Maurer, V., Dalmais, E., Genter, A., Richard, A., Letourneau, O., Hehn, R., 2018. Structure and nature of the Palaeozoic basement based on magnetic, gravimetric and seismic investigations in the central Upper Rhinegraben. Geotherm Energy 6:13, 1-25.

Edel, J. B., Schulmann, K., Skrzypek, E., Cocherie, A., 2013.Tectonic evolution of the European Variscan belt constrained by palaeomagnetic, structural and anisotropy of magnetic susceptibility data from the Northern Vosges magmatic arc (eastern France). Journal of the Geological Society 170(5), 785-804.

Faryad, S. W., Melcher, F., Hoinkes, G., Puhl, J., Meisel, T., Frank, W., 2002. Relics of eclogite facies metamorphism in the Austroalpine basement, Hochgroessen (Speik complex), Austria. Mineralogy and Petrology 74, 49–73.

Faure, M., Bé Mézème, E., Cocherie, A., Rossi, P., Chemenda, A., Boutelier, D., 2008. Devonian geodynamic evolution of the Variscan Belt, insights from the French Massif Central and Massif Armoricain. Tectonics 27, TC2005, 1-19.

Faure, M., Bé Mézème, E., Duguet, M., Cartier, C., Talbot, J. Y., 2005. Paleozoic tectonic evolution of medio-Europa from the example of the French Massif Central and Massif Armoricain. Journal of the Virtual Explorer 19(5), 1-26.

Journal Pre-proof

Faure, M., Cocherie, A., Bé Mézème, E., Charles, N., Rossi, P., 2010. Middle Carboniferous crustal melting in the Variscan Belt: New insights from U–Th–Pb$_{tot.}$ monazite and U–Pb zircon ages of the Montagne Noire Axial Zone (southern French Massif Central). Gondwana Research 18, 653–673.

Faure, M., Cocherie, A., Gaché, J., Esnault, C., Guerrot, C., Rossi, P., Wei, L., Qiuli, L., 2014. Middle Carboniferous intracontinental subduction in the Outer Zone of the Variscan Belt (Montagne Noire Axial Zone, French Massif Central): multimethod geochronological approach of polyphase metamorphism. Geological Society, London, Special Publications 405(1), 289–311.

Faure, M., Lardeaux, J. M., Ledru, P., 2009. A review of the pre-Permian geology of the Variscan French Massif Central. Comptes Rendus Geoscience 341, 202-213.

Faure, M., Leloix, C., Roig, J-.Y., 1997. L'Evolution polycyclique de la chaine hercynienne. Bulletin de la Société Géologique de France 168(6), 695-705.

Faure, M., Prost, A. E., Lasne, E., 1990. Déformation ductile extensive d'âge namuro-westphalien dans le plateau d'Aigurande, Massif central français. Bulletin de la Societe Geologique de France 1(8), 189–197.

Ferrando, S., Lombardo, B., Compagnoni, R., 2008. Metamorphic history of HP mafic granulites from the Gesso-Stura Terrain (Argentera Massif, Western Alps, Italy). Eur. J. Mineral. 20, 777–790.

Feybesse, J.-L., Lardeaux, J.-M., Johan, V., Tegyey, M., Dufour, E., Lemière, B., Delfour, J., 1988. La série de la Brévenne (Massif central francais): une unité dévonienne charriée sur le complexe métamorphique des Monts du Lyonnais à la fin de la collision varisque. Compte Rendu Academie des Sciences de Paris 307(2), 991–996.

Feybesse, J.L., Lardeaux, J.M., Tegyey, M., Gardien, V., Peterlongo, J.M., Kerrien, Y., Becq-Giraudon, J.F., 1996. Carte géologique de France (1/50,000), feuille St-Symphorien sur Coise (721). BRGM, Orléans.

Franke, W., 2000. The mid-European segment of the Variscides: tectonostratigraphic units, terrane boundaries and plate tectonic evolution. Geological Society, London, Special Publications 179(1), 35-61.

Franke, W., Cocks, L. R. M., Torsvik, T. H., 2017. The Palaeozoic Variscan oceans revisited. Gondwana Research 48, 257-284.

Fréville, K., Trap, P., Faure, M., Melleton, J., Li, X.H., Lin, W., Blein, O., Bruguier, O., Poujol, M., 2018. Structural, metamorphic and geochronological insights on the Variscan evolution of the Alpine basement in the Belledonne Massif (France). Tectonophysics 726, 14-42.

Fumasoli, M., 1974. Geologie des Gebietes nördlich und südlich der Jorio-Tonale-Linie im Westen von Gravedona (Como, Italia). Ph.D. Thesis, Zurich.

Gardien, V., 1990. Reliques de grenat et de staurotide dans la série métamorphique de basse pression du mont Pilat (Massif Central français): témoins d'une évolution tectono-métamorphique polyphasée. Compte Rendu Academie des Sciences Paris 310(2), 233-240.

Gardien, V., Lardeaux, J.-M., 1991. Découverte d’éclogites dans le synforme de Maclas: extension de l’Unité Supérieure des Gneiss à l’Est du Massif Central. Compte Rendu Academie des Sciences Paris 312, 61–68.

Gardien, V., Lardeaux, J.M., Ledru, P., Allemand, P., Guillot, S., 1997. Metamorphism during late orogenic extension: insights from the French Variscan belt. Bull. Soc. Géol. France 168(3), 271-286.

Gardien, V., Reusser, E., Marquer, D., 1994. Pre-Alpine metamorphic evolution of the gneisses from the Valpelline series (Western Alps, Italy). Schweizerische Mineralogische Und Petrographische Mitteilungen 74, 489–502.

Gardien, V., Lardeaux, J.-M., Misseri, M., 1988. Les péridotites des Monts du Lyonnais (Massif Central Français): témoins privilégiés d’une subduction de lithosphère océanique paléozoique. Compte Rendu Academie des Sciences de Paris 307, 1967–1972.

Gasco, I., Borghi, A., Gattiglio, M., 2010. Metamorphic evolution of the Gran Paradiso Massif: A case study of an eclogitic metagabbro and a polymetamorphic glaucophane–garnet micaschist Lithos 115(1-4), 101–120.

Gasco, I., Borghi, A., Gattiglio, M., 2011a. P–T Alpine metamorphic evolution of the Monte Rosa nappe along the Piedmont Zone boundary (Gressoney Valley, NW Italy). Lithos 127(1-2), 336–353.

Gay, M., Peterlongo, J.M., Caen-Vachette, M., 1981. Age radio-métrique des granites allongés et en feuillets minces syntectoniques dans les Monts du Lyonnais (Massif Central français). Compte Rendu Academie des Sciences de Paris 293(2), 993-996.

Gébelin, A., Martelet, G., Brunel, M., Faure, M., Rossi, P., 2004. Late Hercynian leucogranites modelling as deduced from new gravity data: The example of the Millevaches massif (Massif Central, France). Bulletin de la Societe Geologique de France 175(3), 239–248.

Gébelin, A., Roger, F., Brunel, M., 2009. Syntectonic crustal melting and high-grade metamorphism in a transpressional regime, Variscan Massif Central, France. Tectonophysics 477(3-4), 229–243.

Genier, F., Bussy, F., Epard, J.-L., Baumgartner, L., 2008. Water-assisted migmatization of metagraywackes in a Variscan shear zone, Aiguilles-Rouges massif, western Alps. Lithos 102(3-4), 575–597.

Gerya, T. V., Stöckhert, B., 2006. Two-dimensional numerical modeling of tectonic and metamorphic histories at active continental margins. Int. J. Earth Sci. (Geol. Rundsch.) 95(2), 250–274.

Gerya, T. V., Yuen, D. A., 2003. Rayleigh-Taylor instabilities from hydration and melting propel 'cold plumes' at subduction zones. Earth planet. Sci. Lett. 212, 47–62.

Giacomini, F., Braga, R., Tiepolo, M., Tribuzio, R., 2007. New constraints on the origin and age of Variscan eclogitic rocks (Ligurian Alps, Italy). Contributions to Mineralogy and Petrology 153(1), 29–53.

Giobbi, M. E., Boriani, A., Villa, I., 2003. Pre-Alpine ophiolites in the basement of Southern Alps: the presence of a bimodal association (LAG-Leptyno-Amphibolitic group) in the Serie dei Laghi (N-Italy, Ticino-CH). Rendiconti Accademia Lincei 9(14), 79–99.

Giobbi, O. E., Gregnanin, A., 1983. The crystalline basement of the “Massiccio delle Tre Valli Bresciane”: new petrographic and chemical data. Memorie della Società Geologica Italiana 26, 133–144.

Giorgis, D., Thélin, P., Stampfli, G., Bussy, F., 1999. The Mont-Mort metapelites: Variscan metamorphism and geodynamic context (Brianconnais basement, Western Alps, Switzerland). Schweizerische Mineralogische Und Petrographische Mitteilungen 79(3), 381-398.

Girardeau, J., Dubuisson, G., Mercier, J.-C. C., 1986. Cinématique de la mise en place des ophiolite et nappes cristallophylliennes du Limousin, Ouest du Massif central français. Bull. Soc. Géol. France 8, 849-860.

Godard, G., 1990. Découverte d'éclogites, de péridotites à spinelle et d'amphibolites à corindon dans le Morvan. Compte Rendu Academie des Sciences de Paris 310, 227-232.

Godard, G., Martin, S., Prosser, G., Kienast, J., Morten, L., 1996. Variscan migmatites, eclogites and garnet-peridotites of the Ulten zone, Eastern Austroalpine system. Tectonophysics 259, 313–341.

Gosso, G., Messiga, B., Spalla, M. I., 1995. Dumortierite-kyanite relics within the HT-LP country rocks of the Sondalo Gabbro: a record of extension related uplift of HP-rocks. International Ophiolite Symposium, Abstract volume, 55.

Gosso, G., Lardeaux, J. M., Zanoni, D., Volante, S., Corsini, M., Bersezio, R., Mascle, J., Spaggiari, L., Spalla, M. I., Zucali, M., Giannerini, G., Caméra, L. Progressive versus finite geological mapping: a key for understanding the geodynamic evolution of the Maritime Alps. Journal of Maps, in press.

Grandjean, V., Guillot, S., Pecher, A., 1996. Un nouveau témoin de l’évolution métamorphique BP-HT post-orogénique hercynienne: l’unité de Peyre-Arguet (Haut-Dauphiné): A new record of the LP-HT late-Variscan metamorphism: the Peyre-Arguet unit (Haut-Dauphiné). Comptes Rendus de l'Academie de Sciences - Serie IIa: Sciences de la Terre et des Planetes 322(3), 189–195.

Guillot, S., di Paola, S., Ménot, R.-P., Ledru, P., Spalla, M. I., Gosso, G., Schwartz, S., 2009. Suture zones and importance of strike-slip faulting for Variscan geodynamic reconstructions of the External Crystalline Massifs of the western Alps. Bulletin de la Societe Geologique de France 180(6), 483-500.

Guillot, S., Ménot, R. P., 1999. Nappe stacking and first evidence of Late Variscan extension in the Belledonne Massif (External Crystalline Massifs, French Alps). Geodinamica Acta 12(2), 97–111.

Guillot, S., Ménot, R. P., 2009. Paleozoic evolution of the External Crystalline Massif of the Western Alps. Tectonics 341, 253-265.

Guillot, S., Ménot, R. P., Fernandez, A., 1998. Paleozoic evolution of the external crystalline massifs along the Belledonne-Oisans transect (Western Alps). Acta Universitatis Carolinae Geologica 42, 257–258.

Haenel, R., Rybach, L., Stegena, L., 1988. Handbook of Terrestrial Heatflow Density Determination. Kluwer Academic Publisher, Dordrecht, 486 pp.

Hauzenberger, C. A., Holler, W., Hoinkes, G., 1996. Transition from eclogite to amphibolite-facies metamorphism in the Austroalpine Ulten Zone. Mineralogy and Petrology 58, 111–130.

Hauzenberger, C. A., Höller, W., Hoinkes, G., Klözli, U., Thöni, M. 1993. Metamorphic evolution of the Austroalpine basement in Nonsberg area, Ultental (Val d'Ultimo), Southern Tyrol. Terra Nova 5, 13.

Herzberg, C., Riccio, L., Chiesa, A., Fornoni, A., Gatto, G. O., Gregnanin, A., Piccirillo, E. M., Scolari, A., 1977. Petrogenetic evolution of a spinelgarnet-lherzolite in the austridic crystalline basement from Val Clapa (Alto Adige, northeastern Italy). Memorie degli Istituti d Geologia e Mineralogia dell'Università di Padova XXX, 6–23.

Holt, A.F., Royden, L.H., Becker, T.W., 2017. The dynamics of double slab subduction. Geophysical Journal International 209, 250–265.

Honda, S., Saito, M., 2003. Small-scale convection under the back-arc occurring in the low viscosity wedge. Earth and Planetary Science Letters 216, 703–715.

Kirby, S. H., 1983. Rheology of the lithosphere. Rev. Geophys. 21(6), 1459-1487.

Konopasek, J., Schulmann, K., 2005. Contrasting Early Carboniferous field geotherms: evidence for accretion of a thickened orogenic root and subducted Saxothuringian crust (Central European Variscides). Journal of the Geological Society of London 162, 463-470.

Konzett, J., Miller, C., Armstrong, R., Thöni, M., 2005. Metamorphic evolution of iron-rich mafic cumulates from the Ötztal-Stubai crystalline complex, Eastern Alps, Austria. Journal of Petrology 46(4), 717–747.

Lafon, J.-M., 1986. Géochronologie U-Pb appliquée à deux segments du Massif central français: Le Rouergue oriental et le Limousin central. Ph.D. thesis, Université Montpellier.

Lardeaux, J.-M., 2014a. Deciphering orogeny: a metamorphic perspective. Examples from European Alpine and Variscan belts. Part II: Variscan metamorphism in the French Massif Central – A review. Bull. Soc. géol. France 185(5), 281-310.

Lardeaux, J.-M., 2014b. Deciphering orogeny: a metamorphic perspective. Examples from European Alpine and Variscan belts. Part I: Alpine metamorphism in the western Alps – A review. Bull. Soc. géol. France 185(2), 93-114.

Lardeaux, J.-M., Dufour, E., 1987. Champs de déformation superposés dans la chaine varisque. Exemple de la zone nord des Monts du Lyonnais (Massif Central francais). Compte Rendu Academie des Sciences de Paris 305(2), 61–64.

Lardeaux, J.-M., Ledru, P., Daniel, I., Duchene, S., 2001. The Variscan French Massif Central - a new addition to the ultra-high pressure metamorphic ‘club’: exhumation processes and geodynamic consequences. Tectonophysics 332, 143-167.

Lardeaux, J.-M., Reynard, B., Dufour, E., 1989. Granulites à kornérupine ert décompression post-orogénique des Monts du Lyonnais (M.C.F.). Compte Rendu Academie des Sciences de Paris 308(2), 1443–1449.

Lardeaux, J. M., Schulmann, K., Faure, M., Janousek, V., Lexa, O., Skrzypek, E., Edel, J. B., Stipska, P., 2014. The Moldanubian Zone in the French Massif Central, Vosges/Schwarzwald and Bohemian Massif revisited: differences and similarities. Geological Society of London, Special Publications 405, 7-44.

Latouche, L., Bogdanoff, S., 1987. Évolution précoce du massif de l’Argentera: apport des éclogites et des granulites. Géologie alpine 63, 151–164.

Le Bayon, B., Pitra, P., Ballevre, M., Bohn, M., 2006. Reconstructing P-T paths during continental collision using multi-stage garnet (Gran Paradiso nappe, Western Alps). Journal of Metamorphic Geology 24(6), 477–496.

Le Fort, P., 1973. Geologie du Haut-Dauphine cristallin (Alpes Francaise): Etudes petrologique et structurale de la partie occidentale. Ph.D. thesis, Université Nancy.

Ledru, P., Autran, A., Santallier, D. 1994. Lithostratigraphy of Variscan terranes in the French Massif Central. A basis for paleogeographical reconstruction. In: Chantraine, J., Rolet, J., Santallier, D. S., Piqué, A., Keppie J.D. (eds.), Pre-Mesozoic Geology in France and Related Areas., IGCP-Project 233 (Terranes In The Circum-Atlantic Paleozoic Orogens), Springer Verlag, Berlin, pp. 276-288.

Ledru, P., Courrioux, G., Dallain, C., Lardeaux, J.-M., Montel, J. M., Vanderhaeghe, O., Vitel, G., 2001. The Velay dome (French Massif Central): Melt generation and granite emplacement during orogenic evolution. Tectonophysics 342(3-4), 207–237.

Ledru, P., Lardeaux, J.-M., Santallier, D., Autran, A., Quenardel, J.-M., Floch, J.-P., Lerouge, G., Maillet, N., Marchand, J., Ploquin, A., 1989. Où sont les nappes dans le Massif central francais? Bulletin de la Societe Geologique de France 8(3), 605-618.

Liati, A., Gebauer, D., Fanning, M., 2009. Geochronological evolution of HP metamorphic rocks of the Adula nappe, Central Alps, in pre-Alpine and Alpine subduction cycles. Journal of Geological Society 166, 797-810.

Liégeois, J. P., Duchesne, J. C., 1981. The Lac Cornu retrograded eclogites (Aiguilles Rouges massif, Western Alps, France): evidence of crustal origin and metasomatic alteration. Lithos 14(1), 35–48.

Lotout, C., Pitra, P., Poujol, M., Anczkiewicz, R., Van Den Driessche, J., 2018. Timing and duration of Variscan high-pressure metamorphism in the French Massif Central: A multimethod geochronological study from the Najac Massif. Lithos 308-309, 381-394.

Lotout, C., Pitra, P., Poujol, M., Van Den Driessche, J., 2017. Ordovician magmatism in the Lévézou massif (French Massif Central): tectonic and geodynamic implications. Int. Journal of Earth Science 106, 501-515.

Maillet, N. 1987. Dualité d'origine des massifs ultra-basiques limousins. Ph.D. Thesis, Université de Lyon I.

Maino, M., Dallagiovanna, G., Gaggero, L., Seno, S., Tiepolo, M., 2012. U-Pb zircon geochronological and petrographic constraints on late to post-collisional Variscan magmatism and metamorphism in the Ligurian Alps, Italy. Geological Journal 47(6), 632–652.

Malavieille, J., Guihot, P., Costa, S., Lardeaux, J.M., Gardien, V., 1990. Collapse of the thickened Variscan crust in the french Massif Central: Mont Pilat extensional shear zone and St Etienne late carboniferous basin. Tectonophysics 177, 139-149.

Manzotti, P., Zucali, M., 2013. The pre-Alpine tectonic history of the Austroalpine continental basement in the Valpelline unit (Western Italian Alps). Geological Magazine 150(1), 153–172.

Marotta, A. M., Roda, M., Conte, K., Spalla, M. I., 2016. Thermo-mechanical numerical model of the transition from continental rifting to oceanic spreading: the case study of the Alpine Tethys. Geological Magazine, 1-30.

Marotta, A. M., Spalla, M. I., 2007. Permian-Triassic high thermal regime in the Alps: Result of late Variscan collapse or continental rifting? Validation by numerical modeling. Tectonics 26, 1–27.

Marotta, A. M., Spelta, E., Rizzetto, C., 2006. Gravity signature of crustal subduction inferred from numerical modelling. Geophys. J. Int. 166, 923–938.

Marotta, A.M., Splendore, R., Barzaghi, R., 2015. An application of model uncertainty statistical assessment: A case study of tectonic deformation in the Mediterranean. Journal of Geodynamics 85, 24-31.

Marshall, D., Kirschner, D., Bussy, F., 1997. A Variscan pressure-temperature-time path for the N-E Mont Blanc massif. Contributions to Mineralogy and Petrology 126(4), 416–428.

Matte, P., 1986. Tectonics and plate tectonics model for the Variscan belt of Europe. Tectonophysics 126, 329–374.

Matte, P., 2001. The Variscan collage and orogeny (480-290 Ma) and the tectonic definition of the Armorica microplate: A review. Terra Nova 13(2), 122-128.

Meda, M., Marotta, A. M., Spalla, M. I. 2010. The role of mantle hydration into continental crust recycling in the wedge region. In: Spalla, M. I., Marotta, A. M., Gosso, G. (eds.), Advances in Interpretation of Geological Processes. Geological Society, London, Special Publications, vol. 332, pp. 149-171.

Melcher, F., Meisel, T., Puhl, J., Koller, F., 2002. Petrogenesis and geotectonic setting of ultramafic rocks in the Eastern Alps: constraints from geochemistry. Lithos 65(1-2), 69-112.

Ménot, R.-P., Bonhommem, M., Vivier, G., 1987. Structuration tecto-métamorphique carbonifère dans le massif de Belledonne (Alpes occidentales françaises). Apport de la geochronologie K/Ar des amphiboles. Schweizerische mineralogische und petrographische Mitteilungen 67, 273–284.

Mercier, L., Johan, V., Lardeaux, J.-M., Ledru, P., 1989. Découverte d'éclogites dans l'artense (M.C.F.) Implications pour la définition des nappes à l'Est du Sillon Houiller. Compte Rendu Academie des Sciences de Paris 308(2), 315–320.

Mercier, L., Johan, V., Lardeaux, J.-M., Ledru, P., 1992. Evolutions tectono-métamorphiques des nappes de l'Aretense (Massif central francais): nouveaux marquers de la collision dans la chaine varisque. Bulletin de la Societe Géologique de France 163(3), 293–308.

Mercier, L., Lardeaux, J.-M., Davy, P., 1991. On the tectonic significance of retrograde P-T-t paths in eclogites of the French Massif Central. Tectonics 10(1), 131-140.

Mercier, L., van Roermund, H. L. M., Lardeaux, J.-M., 1991a. Comparison of Ptt paths in allochthonous high pressure metamorphic terrains from the Scandinavian Caledonides and the French Massif Central: Contrasted thermal structures during uplift. Geologische Rundschau 80(2), 333–348.

Messiga, B., Tribuzio, R., Caucia, F., 1992. Amphibole evolution in Variscan eclogite-amphibolites from the Savona crystalline massif (Western Ligurian Alps, Italy): controls on the decompressional P-T-t path. Lithos 27, 215–230.

Milano, P., Pennacchioni, G., Spalla, M. I., 1988. Alpine and pre-Alpine tectonics in the Central Orobic Alps (Southern Alps). Eclogae Geologicae Helvetiae 81, 273-293.

Miller, C., Thöni, M., 1995. Origin of eclogites from the Austroalpine Ötztal basement (Tirol, Austria): geochemistry and Sm–Nd vs. Rb–Sr isotope systematics. Chemical Geology 122, 199–225.

Mishin, Y.A., Gerya, T.V., Burg, J.-P., Connolly, J.A.D., 2008. Dynamics of double subduction: Numerical modeling. Physics of the Earth and Planetary Interiors 171, 280–295.

Monié, P., 1990. Preservation of Hercynian $^{40}Ar/^{39}Ar$ ages through high-pressure low-temperature Alpine metamorphism in the Western Alps. European Journal of Mineralogy 2(3), 343–361.

Morten, L., Nimis, P., Rampone, E., 2004. Records of mantle–crust exchange processes during continental subduction–exhumation in the Nonsberg-Ultental garnet peridotites (eastern Alps). A review. Periodico di Mineralogia 73, 119–129.

Mottana, A., Nicoletti, M., Petrucciani, C., Liborio, G., De Capitani, L., Bocchio, R., 1985. Pre-alpine and alpine evolution of the South-alpine basement of the Orobic Alps. Geologische Rundschau 74(2), 353–366.

Nussbaum, C., Marquer, D., Biino, G. G., 1998. Two subduction events in a polycyclic basement: Alpine and pre-Alpine high-pressure metamorphism in the Suretta nappe, Swiss Eastern Alps. Journal of Metamorphic Geology 16, 591-605.

Paquette, J. L., Ballèvre, M., Peucat, J.-J., Cornen, G., 2017. From opening to subduction of an oceanic domain constrained by LA-ICP-MS U-Pb zircon dating (Variscan belt, Southern Armorican Massif, France). Lithos 294-295, 418-437.

Paquette, J. L., Ménot, R. P., Peucat, J. J., 1989. REE, Sm-Nd and U-Pb zircon study of eclogites from the Alpine External Massifs (Western Alps): evidence for crustal contamination. Earth and Planetary Science Letters 96(1-2), 181–198.

Paquette, J.-L., Monchoux, P., Couturier, M., 1995. Geochemical and isotopic study of a norite-eclogite transition in the European Variscan belt: Implications for U-Pb zircon systematics in metabasic rocks. Geochimica et Cosmochimica Acta 59(8), 1611–1622.

Pickering, K. T., 1989. The destruction of Iapetus and Tornquist's Oceans. Geology Today 5, 160-166.

Pin, C., 1990. Variscan oceans: Ages, origins and geodynamic implications inferred from geochemical and radiometric data. Tectonophysics 17(1), 215-227.

Pin, C., Lancelot, J., 1982. U-Pb dating of an early Paleozoic bimodal magmatism in the French Massif Central and of its further metamorphic evolution. Contributions to Mineralogy and Petrology 79(1), 1–12.

Pin, C., Paquette, J. L., 1997. A mantle-derived bimodal suite in the Hercynian Belt: Nd isotope and trace element evidence for a subduction-related rift origin of the Late Devonian Brévenne metavolcanics, Massif Central (France). Contrib. Mineral. Petrol. 129, 222-238.

Pin, C., Paquette, J. L., 2002. Le magmatisme basique calcoalcalin d'âge dévono-dinantien du nord du Massif Central, témoin d'une marge active hercynienne: arguments géochimiques et isotopiques Sr/Nd. Geodinamica Acta 15:1, 63-77.

Pin, C., Peucat, J.-J., 1986. Ages des épisodes de métamorphisme paléozoique dans le Massif central et le massif armoricain. Bulletin de la Societe Géologique de France 3, 461-169 (in French with English abstract).

Platt, J.P., 1986). Dynamics of orogenic wedges and the uplift of high-pressure metamorphic rocks. Geol. Soc. Am. Bull. 97, 1037-1053.

Polino, R., Dal Piaz, G. V., Gosso, G., 1990. Tectonic erosion at the Adria margin and accretionary processes for the Cretaceous orogeny of the Alps. Mem. Soc. géol. Fr. 156, 345-367.

Rampone, E.. 2002. Mantle dynamics during Permo-Mesozoic extension of the Europe-Adria lithosphere: insights from the Ligurian ophiolites. Periodico di Mineralogia 73, 215– 230.

Ranalli, G., Murphy, D. C., 1987. Rheological stratification of the lithosphere. Tectonophysics 132(4), 281–295.

Rebay, G., Riccardi, M. P., Spalla, M. I., 2015. Fluid rock interactions as recorded by Cl-rich amphiboles from continental and oceanic crust of Italian orogenic belts. Periodico di Mineralogia 84(3B), 751-777.

Regorda, A., Roda, M., Marotta, A. M., Spalla, M. I., 2017. 2-D numerical study of hydrated wedge dynamics from subduction to post-collisional phases. Geophysical Journal International 211, 974–1000.

Riklin, K., 1983. Kontaktmetamorphose permischer Sandsteine im Adamello-Massiv. Ph.D. thesis, ETH Zurich.

Roda, M., Marotta, A. M., Spalla, M. I., 2010. Numerical simulations of an ocean-continent convergent system: Influence of subduction geometry and mantle wedge hydration on crustal recycling. Geochemistry, Geophysics, Geosystems 11(5), 1-21.

Roda, M., Marotta, A. M., Spalla, M. I., 2011. The effects of the overriding plate thermal state on the slab dip in an ocean–continent subduction system. C. R. Acad. Sci. Paris 343, 323–330.

Roda, M., Spalla, M. I., Marotta, A. M., 2012. Integration of natural data within a numerical model of ablative subduction: a possible interpretation for the Alpine dynamics of the Austroalpine crust. J. Metamorphic Geol. 30(9), 973–996.

Roda, M., Regorda, A., Spalla, M. I., Marotta. A. M., 2018a. What drives Alpine Tethys opening: clues from the review of geological data and model predictions. Geological Journal, 1-19.

Roda, M., Zucali, M., Li, Z.-X., Spalla, M. I., Yao, W., 2018b. Pre-Alpine contrasting tectono-metamorphic evolutions within the Southern Steep Belt, Central Alps. Lithos 310-311, 31-49.

Rode, S., Rosel, D., Schulz, B., 2012. Constraints on the Variscan P-T evolution by EMP Th-U-Pb monazite dating in the polymetamorphic Austroalpine Oetzal-Stubai basement (Eastern Alps). Z. dt. Ges. Geowiss. 163(1), 43–68.

Rolland, Y., Rossi, M., Cox, S. F., Corsini, M., Mancktelow, N., Pennacchioni, G., Fornari, M., Boullier, A. M., 2008. ^{40}Ar/^{39}Ar dating of synkinematic white mica: insights from fluid – rock reaction in low-grade shear zones (Mont Blanc Massif) and constraints on timing of deformation in the NW external Alps. In: Wibberley, C. A. J., Kurz, W., Imber, J., Holdsworth, R. E., Collettini, C. (eds.), The Internal Structure of Fault Zones: Implications for Mechanical and Fluid-Flow Properties. The Geological Society, London, vol. 299, pp. 293-315.

Rosenbaum, G., Lister, G. S., 2005. The western Alps from the Jurassic to Oligocene: spatio-temporal constraints and evolutionary reconstructions. Earth Sci. Rev. 69, 281-306.

Rottura, A., Bargossi, G. M., Caggianelli, A., Del Moro, A., Visonà, D., Tranne, C. A., 1998. Origin and significance of the Permian high-K calc-alkaline magmatism in the central-eastern Southern Alps, Italy. Lithos 45, 329– 348.

Rubatto, D., Ferrando, S., Compagnoni, R., Lombardo, B., 2010. Carboniferous high-pressure metamorphism of Ordovician protoliths in the Argentera Massif (Italy), Southern European Variscan belt. Lithos 116, 65-76.

Sanchez, G., Rolland, Y., Schneider, J., Corsini, M., Oliot, E., Goncalves, P., Verati, C., Lardeaux, J. M., Marquer, D., 2011. Dating low-temperature deformation by 40 Ar/ 39 Ar on white mica, insights from the Argentera-Mercantour Massif (SW Alps). Lithos 125, 521– 536.

Sassi, R., Mazzoli, C., Miller, C., Konzett, J., 2004. Geochemistry and metamorphic evolution of the Pohorje Mountain eclogites from the easternmost Austroalpine basement of the Eastern Alps (Northern Slovenia). Lithos 78, 235-261.

Schmidt, M. W., Poli, S., 1998. Experimentally based water budgets for dehydrating slabs and consequences for arc magma generation. Earth and Planetary Science Letters 163, 361–379.

Schmid, S. M., Fügenschuh, B., Kissling, E., Schuster, R., 2004. Tectonic map and overall architecture of the Alpine orogen. Eclogae Geol. Helv. 97, 93-117.

Schulmann, K., Konopásek, J., Janoušek, V., Lexa, O., Lardeaux, J.-M., Edel, J. B., Štípská, P., Ulrich, S., 2009. An Andean type Palaeozoic convergence in the Bohemian Massif. Comptes Rendus Geoscience 341(2-3), 266-286.

Schulmann, K., Kroner, A., Hegner, E., Wendt, I., Konopasek, J., Lexa, O., Štípská, P., 2005. Chronological constraints on the Pre-Orogenic history, burial and exhumation of the Variscan orogen, Bohemian Massif, Czech Republic. American Journal of Science 305, 407-448.

Schulmann, K., Lexa, O., Janoušek, V., Lardeaux, J.-M., Edel, J. B., 2014. Anatomy of a diffuse cryptic suture zone: An example from the Bohemian Massif, European Variscides. Geology 42(4), 275-278.

Schulz, B., von Raumer, J. F., 2011. Discovery of Ordovician-Silurian metamorphic monazite in garnet metapelites of the Alpine External Aiguilles Rouges Massif. Swiss Journal of Geosciences 104(1), 67–79.

Schuster, R., Scharbert, S., Abart, R., Frank, W., 2001. Permo-Triassic extension and related HT/LP metamorphism in the Austroalpine-Southalpine realm. Mitteilungen der Gesellschaft der Geologie und Bergbaustudenten in Österreich 45, 111– 141.

Schweinehage, R., Massonne, H., 1999. Geochemistry and metamorphic evolution of metabasites from the Silvretta nappe, Eastern Alps. Memorie Scienze Geologiche 51(1), 191– 203.

Siletto, G. B., Spalla, M. I., Tunesi, A., Lardeaux, J.-M., Colombo, A., 1993. Pre-Alpine Structural and Metamorphic Histories in the Orobic Southern Alps, Italy. In: von Raumer, J. F., Neubauer, F. (eds.), Pre-Mesozoic Geology in the Alps. Springer-Verlag, Heidelberg, pp. 585-598.

Skrzypek, E., Schulmann, K., Tabaud, A.-S., Edel, J. B., 2014. Palaeozoic evolution of the Variscan Vosges Mountains. In: Schulmann, K., Martinez Catalan, J. R., Lardeaux, J.-M., Janoušek, V., Oggiano, G. (eds.), The Variscan Orogeny: Extent, Timescale and the Formation of the European Crust. Geological Society, London, vol. 405, pp. 45-75.

Spalla, M. I., Lardeaux, J.-M., Dal Piaz, G. V., Gosso, G., Messiga B., 1996. Tectonic significance of the Alpine eclogites. Journal of Geodynamics 21, 257-285.

Spalla, M. I., Carminati, E., Ceriani, S., Oliva, A., Battaglia, D., 1999. Influence of deformation partitioning and metamorphic re-equilibration on P-T path reconstruction in the pre-Alpine basement of central Southern Alps (Northern Italy). Journal of Metamorphic Geology 17(3), 319–336.

Spalla, M., Diella, V., Pigazzini, N., Siletto, G., Gosso, G., 2006. Significato tettonico della transizione Cld-And nelle metapeliti del Basamento Sudalpino (Alta Val Camonica). Rendiconti della Società Geologica Italiana 2, 182–183.

Spalla, M. I., Gosso, G., 1999. Pre-Alpine tectonometamorphic units in the central southern Alps; structural and metamorphic memory. Memorie di Scienze Geologiche Padova 51(1), 221–229.

Spalla, M. I., Marotta, A. M., 2007. P-T evolutions vs. numerical modelling: a key to unravel the Paleozoic to early-Mesozoic tectonic evolution of the Alpine area. Periodico di Mineralogia 76(2-3), 267-308.

Spalla, M. I., Zanoni, D., Gosso, G., Zucali, M., 2009. Deciphering the geologic memory of a Permian conglomerate of the Southern Alps by pebble P-T estimates. International Journal of Earth Sciences 98(1), 203–226.

Spalla, M. I., Zanoni, D., Marotta, A. M., Rebay, G., Roda, M., Zucali, M., Gosso, G., 2014. The transition from Variscan collision to continental break-up in the Alps: advice from the comparison between natural data and numerical model predictions. Geological Society, London, Special Publications 405(1), 363-400.

Spiess, R., Cesare, B., Mazzoli, C., Sassi, R., Sassi, F. P., 2010. The crystalline basement of the Adria microplate in the eastern Alps: a review of the palaeos- tructural evolution from the Neoproterozoic to the Cenozoic. Rendiconti Lincei Scienze Fisiche Naturali 21, 31-50.

Splendore, R., Marotta, A.M., Barzaghi, R., 2015. Tectonic deformation in the Tyrrhenian: A novel statistical approach to infer the role of the Calabrian Arc complex. JGR Solid Earth 120(11), 1-20.

Stähle, V., Frenzel, G., Hess, J. C., 2001. Permian metabasalt and Triassic alkaline dykes in the northern Ivrea zone: clues to the post-Variscan geodynamic evolution of the Southern Alps. Schweizerische Mineralogische und Petrographische Mitteilungen 81, 1– 21.

Stampfli, G. M., von Raumer, G. M., Borel, G. D., 2002. Paleozoic evolution of pre-Variscan terranes: From Gondwana to the Variscan collision. In: Martínez Catalán, J.R., Hatcher, R. D., Jr., Arenas, R., Díaz García, F. (eds.), Variscan-Appalachian dynamics: The building of the late Paleozoic basement. Geol. Soc. of America Special Paper, vol. 364, pp. 263-280.

Stöckhert, B., Gerya T. V., 2005. Pre-collisional high-pressure metamorphism and nappe tectonics at active continental margins: a numerical simulation. Terra Nova 17, 102-110.

Tait, J.A., Bachtadse, V., Franke, W., Soffel, H.C., 1997. Geodynamic evolution of the European Variscan fold belt: palaeomagnetic and geological constraints. Geol. Rundsch. 86, 585-598.

Thélin, P., Sartori, M., Burri, M., Gouffon, Y., Chessex, R., 1993. The pre-Alpine basement of the briançonnais (Wallis, Switzerland). In: von Raumer, J. F., Neubauer, F. (eds.), Pre-Mesozoic Geology in the Alps, Springer-Verlag, Heidelberg, pp. 297–315.

Thélin, P., Sartori, M., Lengeler, R., Schaerer, J.-P., 1990. Eclogites of Paleozoic or early Alpine age in the basement of the Penninic Siviez-Mischabel nappe, Wallis, Switzerland. Lithos 25, 71-88.

Thöni, M., 1981. Degree and evolution of the alpine metamorphism in the austroalpine unit west of the Hohe tauern in the light of K/Ar and Rb/Sr age determinations on micas. Jahrbuch der Geologischen Bundesanstalt 124, 111–174.

Thöni, M., 2002. Sm–Nd isotope systematics in garnet from different lithologies (Eastern Alps): age results, and an evaluation of potential problems for garnet Sm–Nd chronometry. Chemical Geology 185, 255–281.

Torsvik, T. H., 1998. Palaeozoic palaeogeography: A North Atlantic viewpoint. GFF 120, 109-118.

Trench, A., Torsvik, T. H., 1991. A revised Palaeozoic apparent polar wander path for Southern Britain (Eastern Avalonia). Geophysical Journal International 104, 227-233.

Tumiati, S., Thöni, M., Nimis, P., Martin, S., Mair, V., 2003. Mantle-crust interactions during Variscan subduction in the Eastern Alps (Nonsberg-Ulten zone): Geochronology and new petrological constraints. Earth and Planetary Science Letters 210(3-4), 509–526.

Turcotte, D. L., Schubert, G., 2002. Geodynamics. Second ed., Cambridge University Press, New York, 848 pp.

Vivier, G., Ménot, R. P., Giraud, P., 1987. Magmatismes et structuration orogenique Paleozoiques de la chaine de la Belledonne. Géologie Alpine 63, 25-53.

von Quadt, A., Guenther, D., Frischknecht, R., Zimmermann, R., Franz, G., 1997. The evolution of pre-Variscan ecloogites of the Tauern Window (Eastern Alps): a Sm/Nd, conventional and Laser ICP-MS zircon U-Pb study. Schweizerische Mineralogische und Petrographische Mitteilungen 77, 265–279.

von Raumer, J. F., 1974. Zur Metamorphose amphibolitischer Gesteine im Altkristallin des Mont-Blanc- und Aguilles-Rouges-Massivs. Schweizerische Mineralogische und Petrographische Mitteilungen 54, 471– 488.

von Raumer, J. F., 1998. The Palaeozoic evolution in the Alps: from Gondwana to Pangea. Geol. Rundsch. 87, 407-435.

von Raumer, J. F., Abrecht, J., Bussy, F., Lombardo, B., Ménot, R. P., Schaltegger, U., 1999. The Palaeozoic metamorphic evolution of the Alpine External Massifs. Schweizerische Mineralogische und Petrographische Mitteilungen 79(1), 5–22.

von Raumer, J. F., Bussy, F., Schaltegger, U., Schulz, B., Stampfli, G. M., 2013. Pre-Mesozoic Alpine basements - Their place in the European Paleozoic framework. GSA Bulletin 125(1-2), 89-108.

von Raumer, J. F., Stampfli, G. M., Bussy, F., 2003. Gondwana-derived microcontinents — the constituents of the Variscan and Alpine collisional orogens. Tectnophysics 365, 7-22.

Wessel, P., Smith, W. H. F., 1998. New, improved version of Generic Mapping Tools released. EOS Trans. AGU 79(47), 579.

Whitney, D., Roger, F., Rey, P., Teyssier, C., 2015. Exhumation of high-pressure rocks in a Variscan migmatite dome (Montagne Noire, France). Geophysical Research Abstracts 17, EGU2015-3266.

Will, T. M., Schmadicke, E., Ling, X.-X., Li, X.-H., Li, Q.-L., 2018. New evidence for an old idea: Geochronological constraints for a paired metamorphic belt in the central European Variscides. Lithos 302-303, 278-297.

Zanoni, D., Spalla, M. I., 2018. The Variscan evolution in basement cobbles of the Permian Ponteranica Formation by microstructural and petrologic analysis. Ital. J. Geosci. 137, 254-271.

Zanoni, D., Spalla, M. I., Gosso, G., 2010. Vestiges of lost tectonic units in conglomerate pebbles? A test in Permian sequences of the Southalpine Orobic Alps. Geological Magazine 147(1), 98–122.

Zimmermann, V. R., Franz, G., 1989. Die Eklogite der Unteren Schieferhülle; Frosnitztal/Südvenediger (Tauern, Österreich). Mittelungen der Östereichischen Geologischen Gesellschaft 81, 167–188.

Zucali, M., 2001. La correlazione nei terreni metamorfici: due esempi dall'Austroalpino occidentale (Zona Sesia-Lanzo) e centrale (Falda Languard-Campo/ Serie del Tonale). Ph.D. thesis, Università degli Studi di Milano.

Zucali, M., Spalla, M. I., 2011. Prograde lawsonite during the flow of continental crust in the Alpine subduction: Strain vs. metamorphism partitioning, a field-analysis approach to infer tectonometamorphic evolutions (Sesia-Lanzo Zone, Western Italian Alps). Journal of Structural Geology 33(3), 381–398.

APPENDIX A

Table A1 Details of the Variscan metamorphism in the Alps.

Table A2 Details of the Variscan metamorphism in the FMC.

Tables

Table 1 P_{max}-T estimates recorded in the crustal and mantle rocks of the Alps.

Helvetic domain (Hv): AR–Argentera; BD–Belledonne; P–Pelvoux; Ai–Aiguilles Rouges; MB–Mont Blanc. Penninic domain (Pv): LB–Ligurian Brianconnais; GP–Gran Paradiso; MR–Monte Rosa; GS–Grand ST. Bernardo; Ad–Adula; SU–Suretta; TW–Tauern window. Austroalpine domain (Av): SC–Speik Complex; Oe–Oetztal; TZ–Ulten Zone; Sil–Silvretta; LCN–Languard-Campo nappe; DB–Dent Blanche. Southapline domain (Sv): DCZ–Domaso-Cortafò Zone; VVB–Val Vedello basement; NEOB–NE Orobic basement; TVB–Tre Valli Bresciane; Ei–Eisecktal.

Table 2 P_{max}-T estimates recorded in the crustal and mantle rocks of the FMC. UGU–Upper Gneiss Unit; LGU–Lower Gneiss Unit; LAC–Leptyno-amphibolitic Complex; PAU–Para-autochthonous Unit; MN–Montagne Noire fold-and-thrust Belt; TPU–Thiviers-Payzac Unit.

Table 3 Material and rheological parameters used in the numerical modelling.

Figure captions

Fig. 1 Simplified tectonic sketch of the Variscan belt (modified after Delleani et al., 2018 and references therein). Arm–Armorican Massif; BCBF–Bristol Channel-Bray Fault; BM–Bohemian Massif; Ca–Cantabrian terrane; Cib–Central Iberian; Co–Corsica; FMC–French Massif Central; MT–Maures-Tanneron Massif; OM–Ossa Morena; Py–Pyrenees; Sa–Sardinia; Si–Sicilian-Apulian basements; SP–South Portuguese Zone; WL–West Asturian-Leonese.

Fig. 2 Tectonic map of the Alps with the localisation of the data listed in Table 1. Red lines are major tectonic lineaments.

Fig. 3 Tectonic map of the French Massif Central with the localisation of the data in Table 2. Red areas represent the Upper Gneiss Unit, blue areas the Lower Gneiss Unit, light blue areas the Para-autochthonous Unit, green areas the Thiviers-Payzac Unit, yellow represent the Montagne Noire and brown represent the Fold-and-Thrust belt.

Fig. 4 Setup, boundary conditions, initial thermal configuration and acronyms of the numerical models. The distances are not to scale. UP–upper plate; LP–lower plate.

Fig. 5 Markers distribution, isotherms 800 and 1100 K (dashed black lines) and streamline patterns (solid black lines in the insets) in the surrounding of the wedge area for models DS.1 (a), DS.2.5 (b) and DS.5 (c) at 25.5 Myr of evolution of the phase 1. Streamlines are curves tangent at the velocity of the fluid. The difference $\Delta\Psi$ of values between two streamlines is equivalent to the flow capacity per unit of thickness across the two streamlines. Curves that differ from each other by the same amount of $\Delta\Psi$ gather in areas where the flow has a higher velocity.

Fig. 6 Large-scale temperature field (colours) and streamline patterns (black lines) predicted by the models DS. t_r indicates the time relative to the beginning of phase 3 and t_0 indicates the time from the beginning of the evolution. Streamlines are curves tangent at the velocity of the fluid. The difference $\Delta\Psi$ of values between two streamlines is equivalent to the flow capacity per unit of thickness across the two streamlines. Curves that differ from each other by the same amount of $\Delta\Psi$ gather in areas where the flow has a higher velocity.

Fig. 7 Comparison between the isotherms 800 (continuous lines) and 1100 K (dashed lines) predicted by model SS.5 during phases 1 and 2 (green lines) and by models DS.1, DS.2.5 and DS.5 during phases 3 and 4 (black, red and blue lines, respectively). t_r indicates the time relative to the beginning of phase 2 for model SS.5 and of phase 4 for models DS; t indicates the time relative to the beginning of phase 1 for model SS.5 and of phase 3 for models DS.

Fig. 8 Markers distribution, isotherms 800 and 1100 K (dashed black lines) and streamline patterns (solid black lines in the insets) in the surrounding of the wedge area for models DS.1 (panels a_i), DS.2.5 (panels b_i) and DS.5 (panels c_i) at different times of evolution the of phase 3. t_r indicates the time relative to the beginning of phase 3 and t_0 indicates the time from the beginning of the evolution. Streamlines are curves tangent at the velocity of the fluid. The difference $\Delta\Psi$ of values between two streamlines is equivalent to the flow capacity per unit of thickness across the two streamlines. Curves that differ from each other by the same amount of $\Delta\Psi$ gather in areas where the flow has a higher velocity.

Fig. 9 Large-scale temperature field (colours) and streamline patterns (black lines) predicted by the models DS at 10 Myr (panels a_i) and 42 Myr (panels b_i) after the beginning of phase 4. t_r indicates the time relative to the beginning of phase 4 and t_0 indicates the time from the beginning of the evolution. Streamlines are curves tangent at the velocity of the fluid. The difference $\Delta\Psi$ of values between two streamlines is equivalent to the flow capacity per unit of thickness across the two streamlines. Curves that differ from each other by the same amount of ΔΨ gather in areas where the flow has a higher velocity.

Fig. 10 Comparison between the isotherms 800 (continuous lines) and 1100 K (dashed lines) predicted by model SS.5 (green lines) and by models DS.1, DS.2.5 and DS.5 (black, red and blue lines, respectively), at 72 Myr (a) and 130 Myr (b) from the beginning of the evolution.

Fig. 11 Fitting of natural P_{max}-T estimates of the Alps (a) and of the FMC (b) with model DS.2.5. Black bars represent the age of natural P-T estimates, while colour bars represent the fitting with the markers of the model, with different colours indicating the number of the marker showing the agreement. Red vertical lines identify the beginning of phases 2 and 4, while blue vertical lines identify the beginning of phase 3. Keys are the same as listed in Tables 1 and 2. Red keys represent geological ages, black keys represent radiometric ages.

Fig. 12 P_{max}-T estimates of data from the Helvetic domain (a), the Penninic domain (b), the Austroalpine domain (c), the Southalpine domain (d) and from the FMC (e). Different colours of the data indicate different lithological affinities as described in the legend. Dot lines represent very low subduction-zone geothermal gradient (5 °C/km).

Fig. 13 Comparison between model DS.2.5 and P_{max}-T estimates from the Alps for different times during phases 1 (a–d) and 2 (e). In agreement with notation in Fig. 2, red dots indicate fitting with data from the Helvetic domain, light blue dots fitting with data from the Penninic domain, yellow dots fitting with data from Austroalpine domain and blue dots indicate fitting with Southalpine domain. t_a indicates the absolute time relative to and t_0 indicates the time from the beginning of the evolution.

Fig. 14 Comparison between model DS.2.5 and P_{max}-T estimates from the FMC for different times during phases 1 (a–d) and 2 (e). In agreement with notations in Fig. 3, red dots indicate fitting with data from the UGU, blue dots indicate fitting with data from the LGU and light blue dots indicate fitting with data from the PAU t_a indicates the absolute time relative to and t_0 indicates the time from the beginning of the evolution.

Fig. 15 Comparison between model DS.2.5 and P_{max}-T estimates from the Alps for different times during phases 3 (a–c) and 4 (d and e). In agreement with notation in Fig. 2, red dots indicate fitting with data from the Helvetic domain, light blue dots fitting with data from the Penninic domain, yellow dots fitting with data from Austroalpine domain and blue dots indicate fitting with Southalpine domain. t_a indicates the absolute time relative to and t_0 indicates the time from the beginning of the evolution.

Fig. 16 Comparison between model DS.2.5 and P_{max}-T estimates from the FMC for different times during phases 1 (a–c) and 2 (d and e). In agreement with notations in Fig. 3, red dots indicate fitting with data from the UGU, blue dots indicate fitting with data from the LGU and light blue dots indicate fitting with data from the PAU, green dots indicate fitting with data from the TPU and yellow dots indicate fitting with data from MN. t_a indicates the absolute time relative to and t_0 indicates the time from the beginning of the evolution.

Fig. 17 Fitting of natural P_{max}-T estimates of the Alps (a) and of the FMC (b) with model SS.5. Black bars represent the age of natural P-T estimates, while colour bars represent the fitting with the markers of the model, with different colours indicating the number of the marker showing the agreement. Red vertical lines identify the beginning of phase 2. Keys are the same as listed in Tables 1 and 2. Red keys represent geological ages, black keys represent radiometric ages.

Fig. 18 Simplified tectonic sketch of the Variscan belt with the evolution for the FMC and the Alps as suggested by the fitting between natural P-T estimates and P-T predicted by the double subduction model (DS.2.5). Arm–Armorican Massif; FMC–French Massif Central; MT–Maures-Tanneron Massif.

Key	Location	Lithology	Paragenesis	T (°C)	P (GPa)	Age (Ma)	References
Hv1	AR: Tinèe; Gesso-Stura-Vésubie	Metabasite	Grt + Hbl + Cpx + Pl + Qtz	710–760	1.2–1.4	420–428 (U/Pb)	Latouche and Bogdanoff, 1987; Paquette et al., 1989
Hv2	AR: Frisson	Eclogitc gneiss	Grt + Hbl + Cpx + Pl + Qtz + Ru/Ilm	720–750	1.33–1.43	336–344 (U/Pb)	Ferrando et al., 2008; Rubatto et al., 2010
Hv3	BD: Allemont	Metapelite	Grt + St + Ky + Bt + Ms + Pl + Qtz + Rt/Ilm + Sill + Crd	500–600	0.9–1.1	Devonian (350–420)	Guillot and Ménot, 1999; Guillot et al., 2009
Hv3b	BD: Allemont	Metapelite	Grt + Bt + Ms + Pl + Qtz + Sil	660–680	0.68–0.87	330–344 (U/Pb)	Fréville et al., 2018
Hv4	BD: Livet	Metapelite	Grt + St + Bt + Pl + Qtz + Ilm + Mu	530–650	0.6–1.0	297–407 (K/Ar)	Ménot et al., 1987; Guillot and Ménot, 1999; Guillot et
Hv4b	BD: Riouperoux-Livet	Metapelite	Grt + Bt + Ms + Ky + Ab + Pl + Qtz	400–430	0.6–0.78	330–344 (U/Pb)	Fréville et al., 2018
Hv4c	BD: Riouperoux-Livet	Metapelite	Grt + St + Bt + Ms + Qtx	590–620	0.52–0.66	330–344 (U/Pb)	Fréville et al., 2018
Hv5	P: Romanche valley	Metabasite	Amph + Pl + Qtz + Ilm + Bt	650–785	0.45–0.7	311–335 (Ar/Ar)	di Paola, 2001
Hv6	P: Oisan	Metabasite	Amph + Pl + Opx + Cpx + Grt + Qtz + Ru/Ilm	775–994	0.9–1.7	Variscan (295–425)	di Paola, 2001
Hv7	P: La Lavey	Metabasite	Amph + Pl + Cpx + Grt	800–900	1.3–1.5	Early Variscan (375–425)	Le Fort, 1973; Guillot et al., 1998
Hv8	P: Peyre Arguet	Metabasite	Amph + Pl + Grt + Opx	750–850	0.3–0.7	Variscan (295–425)	Le Fort, 1973; Grandjean et al., 1996; Guillot et al., 1998
Hv9	BD: Lac de la Croix; Beaufortin	Metabasite	Grt + Cpx + Pl + Qtz + Ru + Zr Grt + Hbl + Cpx + Qtz + Ru + Zo	610–670	1.1–1.3	382–398 (U/Pb)	Paquette et al., 1989; Guillot et al.,1998
Hv10	Ai: Lac Cornu	Metabasite	Grt + Cpx + Hbl + Qtz + Ru	725–750	1.5–1.6	387–403 (U/Pb)	Liégeois and Duchesne, 1981; Paquette et al., 1989; von
Hv11	Ai: Lac Cornu; Col de Bérard	Metapelite	Grt + Bt + Ms + Sil + Pl + Qtz	625–675	1.2–1.4	> 330	Schulz and von Raumer, 2011
Hv12	Ai: Emosson lake	Metapelite	Grt + Bt + Ms + Sil + Pl + Qtz	525–575	0.8–1.0	> 320	Genier et al., 2008
Hv13	MB: Mont Blanc	Amphibolite Skarn	Amph + Grt + Qtz +Pl Grt + Cpx + Amph + Ep + Ap + Zr	499–590	0.61–0.76	307–335 (Ar/Ar)	Marshall et al., 1997
Pv1	LB: Savona Massif	Eclogite	Grt + Omp + Zo + Ru + Ky + Qtz + Phe + Pl + Cpx + Ol?	650–750	> 1.7	374–392 (U/Pb)	Messiga et al., 1992; Giacomini et al., 2007; Maino
Pv2	GP: Gran Paradiso	Metapelite	Grt + St + Ilm + Qtz	600–650	0.5–0.7	Variscan (295–425)	Le Bayon et al.,2006
Pv3	GP: Orco valley	Metapelite	Bt + Chl + Pl + Grt + Qtz + Pg	610–630	0.8–0.9	Variscan (295–425)	Gasco et al., 2010
Pv4	MR: Monte Rosa	Metapelite	Bt + Chl + Grt + Pl + Ms + Qtz + Pg + St	550–575	0.4–0.6	Variscan (295–425)	Gasco et al., 2011a
Pv5	GS: Ambin nappe (Clarea complex)	Metapelite	Grt + Ms + Bt + Qtz + Ru + Ky + St	550–650	0.8–1.1	340–360 (Ar/Ar)	Monié, 1990; Borghi et al., 1999
Pv6	GS: Mont Mort	Metapelite	Grt + Bt + Sil/And	550–600	0.5–0.8	328–332 (U/Pb)	Bussy et al., 1996; Giorgis et al., 1999
Pv7	GS: Siviez-Mischabel	Metabasite	Hbl + Pl + Qtz	550–650	0.5–0.6	Variscan (295–425)	Thélin et al., 1993
Pv8	Ad: Central part	Metabasite	Grt + Omp + Ky + Ms + Amph + Qtz + Dol + Ru Qtz + Ms + Pl + Bt + Grt + Ru	675–825	1.95–2.45	346–402 (U/Pb)	Dale and Holland, 2003; Liati et al., 2009
Pv9	Ad: Northern part	Metabasite	Grt + Omp + Ky + Ru + Ms + Ep + Pl + Qtz Pl + Qtz + Grt + Ms + Amph + Ep + Bt	565–715	1.45–1.95	304–354 (U/Pb)	Dale and Holland, 2003; Liati et al., 2009
Pv10	Su: Suretta	Metabasite	Grt + Hbl + Ep + Qtz + Cpx	617–750	> 2.0	Variscan (295–425)	Nussbaum et al., 1998
Pv11	TW: Frosnitztal	Metabasite	Grt + Omp + Qtz	400–500	0.8–1.2	400–437 (U/Pb)	Zimmermann and Franz, 1989; von Quadt et al., 1997
Pv12	TW: Doesenertal	Metabasite	Grt + Omp + Qtz	520–720	> 1.2	400–437 (U/Pb)	von Quadt et al., 1997; Droop, 1983
Av1	SC: Hochgrossen Massif	Metabasite	Amph + Cpx + Ab + Zo	650–750	2.0–2.2	389–405 (Ar/Ar)	Faryad et al., 2002; Melcher et al., 2002
Av2	Oe: Central Oetztal Stubai	Metabasite	Grt + Omp	700–800	2.5–2.9	340/370 (Rb/Sr)	Miller and Thöni, 1995; Thöni, 2002; Konzett et al.,
Av3	Oe: Oetztal Stubai	Metapelite	Grt + Qtz + Ky + Sil + St + Ms + Bt + Pl	550–650	1.1–1.3	350–360	Rode et al., 2012
Av4	TZ; Ultental	Metapelite	Grt + Bt + Pl + Kfs + Ky + Ms + Ru	650–750	1.0–2.0	365 (Pb/Pb)	Godard et al., 1996; Hauzenberger et al., 1996
Av5	TZ: Ultental	Metabasite	Grt + Omp + Qtz	640–700	1.2–1.6	360 (Ar/Ar)	Herzberg et al., 1977
Av6	TZ: Ultental	Ultramafite	Grt- bearing ultramafics	770–810	2.2–2.8	326–334 (Sm/Nd)	Herzberg et al., 1977; Tumiati et al., 2003; Morten et al.,
Av7	Sil: Ischgl	Metabasite	Grt + Omp + Qtz + Ru + Phe	620–670	2.3–2.9	> 387	Schweinehage and Massonne, 1999
Av8	Sil: Val Puntota	Metabasite	Grt + Omp + Qtz + Ru + Phe	400–500	2.5–2.7	> 387	Schweinehage and Massonne, 1999
Av9	LCN: Mortirolo	Metapelite	Dum + Qtz	750–850	> 2.0	Early Variscan (375–425)	Gosso et al., 1995
Av10	LCN: Mortirolo	Metabasite	Di + Grt + Scp + Pl + Qtz	750–950	0.65–0.9	314–370	Thöni, 1981; Zucali, 2001
Av11	DB: Valpelline	Metapelite	Bt + Qtz + Pl + Kfs + Grt + Zrn + Mnz + Ry + Ap + Sil	661–745	0.45–0.65	< 320	Zucali and Spalla, 2011; Manzotti and Zucali, 2013
Av12	DB: Valpelline	Metabasite	Bt + Qtz + Pl + Kfs + Grt + Zrn + Mnz + Ry + Ap + Sil	700–750	0.9–1.0	< 320	Gardien et al., 1994; Manzotti and Zucali, 2013
Sv1	Strrona Ceneri Zone	Metapelite	Hbl + Pl + Bt + Chl	590–690	0.6–0.8	307–359 (Ar/Ar)	Boriani and Villa, 1997; Giobbi et al., 2003
Sv2	DCZ: Upper Como lake	Metapelite	Grt + Bt + Ms + Qtz + Pl + St + Ky	560–650	0.7–1.1	300–400 (K/Ar)	Fumasoli, 1974; Mottana et al., 1985; di Paola and Spalla,
Sv3	Monte Muggio Zone	Metapelite	Grt + Bt + Ms + Ky + St	560–580	0.7–0.9	320–340 (K/Ar)	Mottana et al., 1985; Bertotti et al., 1993; Siletto et al., 1993
Sv4	VVB: Dervio Olgiasca	Metapelite	Grt + Bt + Ms + Pl + Qtz + Ky + St	550–630	0.7–0.9	320–340	Diella et al., 1992; Zanoni et al., 2010
Sv5	Val Vedello	Metapelite	Bt + Grt + St	590–668	0.7–1.1	320–340	Zanoni et al., 2010
Sv6	Val Vedello	Metapelite	Grt + Chl	470–550	0.35–0.75	< 320	Zanoni et al., 2010
Sv7	Valtellina NEOB Type A	Metapelite	Grt + St + Bt + Ms + Plg + Qtz + Cld	570–660	0.85–1.15	320–340	Spalla et al., 1999
Sv8	Valtellina NEOB Type B	Metapelite	Qtz + Ms + Chl + Ab + Grt + Bt	440–550	0.35–0.75	320–340	Spalla and Gosso, 1999; Zanoni et al., 2010
Sv9	Val Camonica NEOB Type A	Metapelite	Grt + St + Bt + Ms + Pl + Qtz + Cld	550–630	0.8–1.1	320–340	Spalla et al., 2006
Sv10	TVB: Val Trompia	Metapelite	Grt + Cld + Bt + Ms + Pl + Qtz	500–550	0.9–1.3	349–379 (Rb/Sr)	Giobbi and Gregnanin, 1983; Riklin, 1983; Spalla et al.,
Sv11	Ei: Eisecktal	Paragneiss	Crd + Sil + Bt	600–650	0.2–0.3	Devonian (350–420)	Benciolini et al., 2006
Sv12	Ei: Eisecktal	Metapelite	Qtz + Chl + Grt + Bt + Kfs + Ol	450–550	0.5–0.65	Devonian (350–420)	Benciolini et al., 2006

Key	Location	Lithology	Paragenesis	T (°C)	P (GPa)	Age (Ma)	References
HA1	Haut Allier	Eclogite (UGU)	Grt + Omp + Ky + Qtz + Ru + Zo	750–850	1.8–2.2	Middle to lower Devonian (380–416)	Ducrot et al., 1983; Ledru et al., 1989; Faure et al., 2005; Faure et al., 2008; Lardeaux, 2014; Paquette et al., 2017; Lotout et al., 2018
Ma1	Marvejols	Eclogite (UGU)	Grt + Omp + Ky + Qtz + Ru + Zo	800–850	1.8–2.0	Middle to lower Devonian (380–416)	Pin and Lancelot, 1982; Ledru et al., 1989; Mercier et al., 1991a; Faure et al., 2005; Faure et al., 2008; Lardeaux, 2014; Paquette et al., 2017; Lotout et al., 2018
Li1	Limousin	Migmatite (LGU)	Qtz + Pl + Kfs + Grt + Ky/Sil	600–700	0.8–1.1	370–385 (U/Th/Pb)	Faure et al., 2008; Faure et al., 2009
Li2	Limousin	Metapelite (UGU)	Ky + Bt + Ms + Pl + Grt	830	1.6–1.9	390–430	Bellot and Roig, 2007
Li3	Limousin	Migmatite (LGU)	Kfs + Sil + Grt + Pl + Qtz	760–780	0.5–0.6	349–359 (U/Th/Pb)	Gébelin et al., 2004, 2009
Li4	Limousin	Eclogite (LGU)	Zo + Grt + Omp + Ky + Ru	580–730	2.5–3.5	406–418 (U/Pb)	Berger et al., 2010
Li5	Limousin	Migmatite (UGU)	Qtz + Pl + Kfs + Grt + Ky/Sil	650–750	0.7–0.8	377–387 (U/Pb)	Lafon, 1986; Faure et al., 2005, 2008
LB1	La Bessenoits	Eclogite (UGU)	Grt + Qtz + Ru + Zo + Ap	600–710	1.6–1.9	401–415 (Sm/Nd)	Paquette et al., 1995; Faure et al., 2008; Lardeaux, 2014; Paquette et al., 2017
ML1	Mont du Lyonnais	Peridotite (UGU)	Spi-bearing lherzolite	880–950	< 2.0	Variscan (295–425)	Gardien et al., 1988
ML2	Mont du Lyonnais	Eclogite (UGU)	Grt + Omp + Qtz + Zo + Ky + Ph + Ru	730–780	1.5	Middle to lower Devonian (380–416)	Dufour et al., 1985; Feybesse et al., 1988; Lardeaux et al., 1989, 2001; Mercier et al., 1991a
ML3	Mont du Lyonnais	Metapelite (UGU)	Qtz + Pl + Kfs + Grt + Ky/Sil+ Bt	600–750	0.6–1.0	350–360 (Ar/Ar)	Lardeaux and Dufour, 1987; Costa et al., 1993; Faure et al., 2005, 2008, 2009
ML4	Mont du Lyonnais	Migmatite (UGU)	Qtz + Pl + Kfs + Sil + Bt	650–750	0.7–1.2	368–400 (Rb/Sr)	Dufour, 1982; Duthou et al., 1994
Ro1	Lévézou	Eclogite (UGU)	Grt + Omp + Ky + Qtz + Ru + Zo	680– 800	2.1–2.3	344–370	Burg et al., 1989; Mercier et al., 1991a; Lotout, 2017
Ro2	Najac	Eclogite (UGU)	Grt + Omp + Ky + Qtz + Zo	560– 630	1.5–2.0	376– 385	Burg et al., 1989; Mercier et al., 1991a; Lotout et al., 2018
Ro3	Le Vibal	Eclogite (UGU)	Grt + Ky + Qtz+ Omp	740–860	1.0–1.4	Variscan (295–425)	Burg et al., 1989;
Ar1	Artense	Eclogite (UGU)	Grt + Cpx + Qtx + Ru + Zo	700–750	1.4–1.6	Variscan (295–425)	Mercier et al., 1989, 1991a
Ar2	Artense	Paragneiss (LGU)	Qtz + Pl + Bt + Sil + Grt	670–750	0.6–0.82	Variscan (295–425)	Mercier et al., 1992
PA1	Plateau d'Aigurande	Metapelite (UGU)	Grt + Ky + Qtz	650–750	1.0–1.2	376–397 (Ar/Ar)	Faure et al., 1990, 2008; Boutin and Montigny, 1993
PA2	Plateau d'Aigurande	Micaschist (PAU)	Ms + Chl + Grt+ Qtz	550–650	0.6–0.8	350–380 (Ar/Ar)	Faure et al., 1990
Mc1	Maclas	Eclogite (UGU)	Grt + Cpx + Qtz + Ru + Zo	700–770	1.4–1.6	Variscan (295–425)	Gardien and Lardeaux, 1991; Ledru et al., 2001
VD1	Velay Dome	Migmatite (LGU)	Kfs + Bt + Sil ± Co	675–725	0.4–0.5	309–319 (U/Pb)	Ledru et al., 2001; Barbey et al., 2015

VD2	Velay Dome (Cévennes)	Micaschist (PAU)	Ms + Chl + Grt + Qtz	475–525	0.4–0.6	335–340 (Ar/Ar)	Ledru et al., 2001
MN1	Montagne Noire	Eclogite (MN)	Grt + Omp + Rt + Qtz	700–800	2.1	309–317 (U/Th/Pb)	Demange, 1985; Faure et al., 2014; Whitney et al., 2015
MN2	Montagne Noire	Metabasite (MN)	Spi-bearing ultramafite	800–900	0.5–1.0	326–333	Demange, 1985
TP1	Quercy	Metapelite (TPU)	Qtz + Pl + Ms + Bt + Grt + Rt + Ap + Mo	400–500	0.4–0.6	350–360 (Ar/Ar)	Duguet et al., 2007; Faure et al., 2009

	Rheology	E (kJ/mol)	n	μ_0 (Pa·s)	ρ_0 (kg/m^3)	K (W/(m·K))	H_c (μW/m^3)	References
Continental Crust	Dry Granite	123	3.2	3.47×10^{21}	2640	3.03	2.5	Ranalli and Murphy, 1987; Haenel et al., 1988; Dubois and Diament, 1997; Best and Christiansen, 2001
Upper Oceanic Crust	-	-	-	10^{19}	2961	2.10	0.4	Dubois and Diament, 1997; Best and Christiansen, 2001; Gerya and Yuen, 2003; Afonso and Ranalli, 2004; Gerya and Stockhert, 2006; Roda et al., 2012;
Lower Oceanic Crust	Diabase	260	2.4	1.61×10^{22}	2961	2.10	0.4	Kirby, 1983; Ranalli and Murphy, 1987; Dubois and Diament, 1997; Best and Christiansen, 2001; Afonso and Ranalli, 2004
Mantle	Dry Dunite	444	3.41	5.01×10^{20}	3200	4.15	0.002	Chopra and Peterson, 1981; Kirby, 1983; Haenel et al., 1988; Dubois and Diament, 1997; Best and Christiansen, 2001; Roda et al., 2012
Serpentine	-	-	-	10^{19}	3000	4.15	0.002	Haenel et al., 1988; Dubois and Diament, 1997; Schmidt and Poli, 1998; Best and Christiansen, 2001; Roda et al., 2011; Gerya and Stockhert, 2006

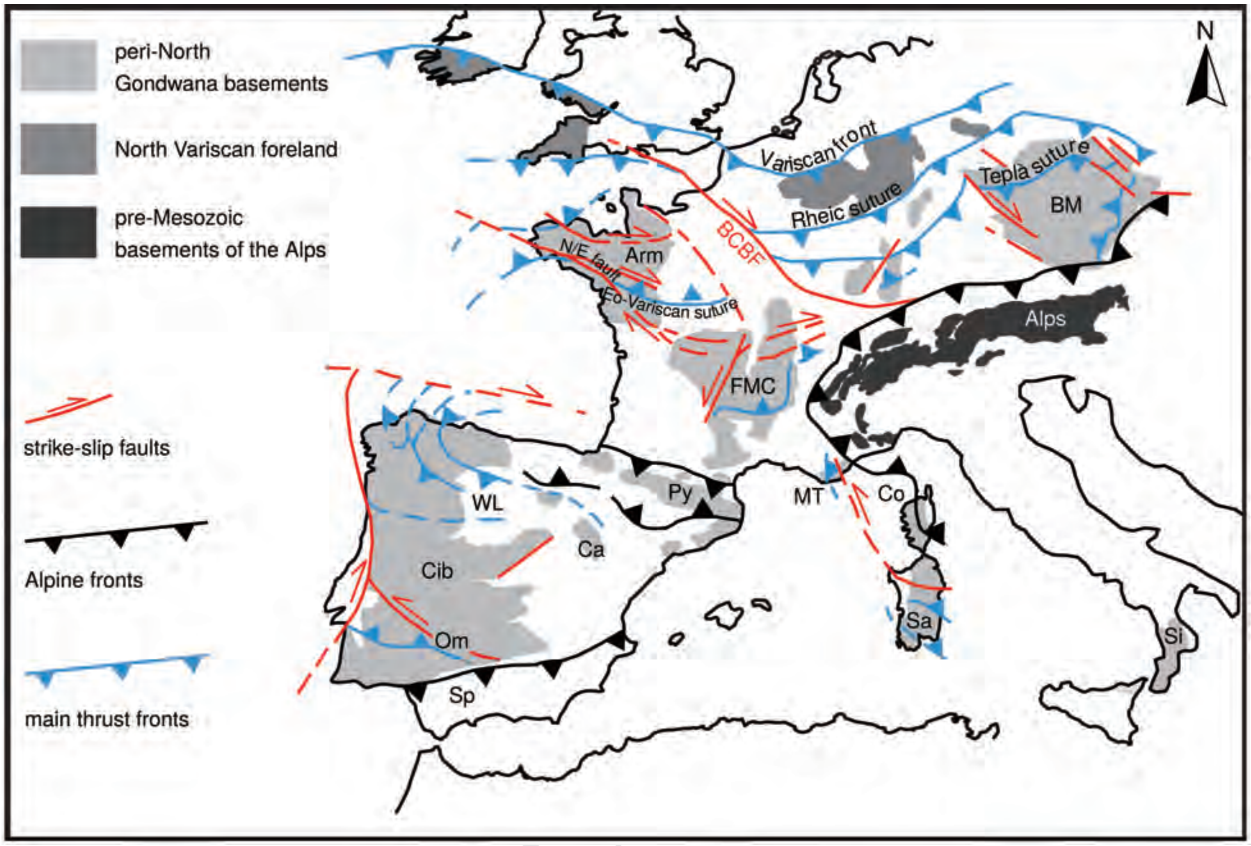
peri-North Gondwana basements
North Variscan foreland
pre-Mesozoic basements of the Alps
strike-slip faults
Alpine fronts
main thrust fronts
N
Variscan front
Rheic suture
Tepla suture
BM
BCBF
N/E fault
Arm
Eo-Variscan suture
Alps
FMC
WL
Py
Ca
Cib
Om
Sp
MT
Co
Sa
Si

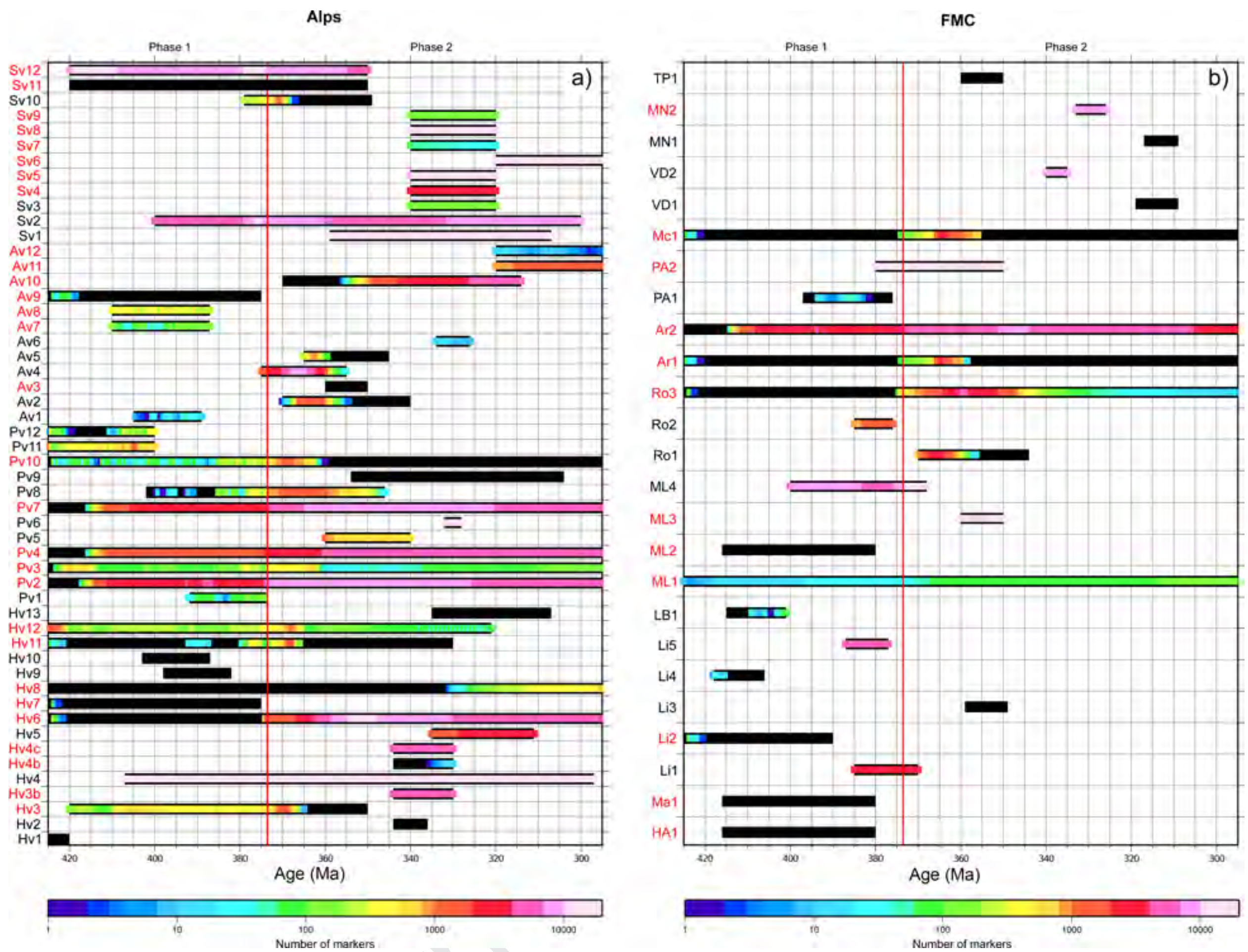

Alps
Phase 1
Phase 2
a)
Sv12
Sv11
Sv10
Sv9
Sv8
Sv7
Sv6
Sv5
Sv4
Sv3
Sv2
Sv1
Av12
Av11
Av10
Av9
Av8
Av7
Av6
Av5
Av4
Av3
Av2
Av1
Pv12
Pv11
Pv10
Pv9
Pv8
Pv7
Pv6
Pv5
Pv4
Pv3
Pv2
Pv1
Hv13
Hv12
Hv11
Hv10
Hv9
Hv8
Hv7
Hv6
Hv5
Hv4c
Hv4b
Hv4
Hv3b
Hv3
Hv2
Hv1
420
400
380
360
340
320
300
Age (Ma)
1
10
100
1000
10000
Number of markers
FMC
Phase 1
Phase 2
b)
TP1
MN2
MN1
VD2
VD1
Mc1
PA2
PA1
Ar2
Ar1
Ro3
Ro2
Ro1
ML4
ML3
ML2
ML1
LB1
Li5
Li4
Li3
Li2
Li1
Ma1
HA1
420
400
380
360
340
320
300
Age (Ma)
1
10
100
1000
10000
Number of markers

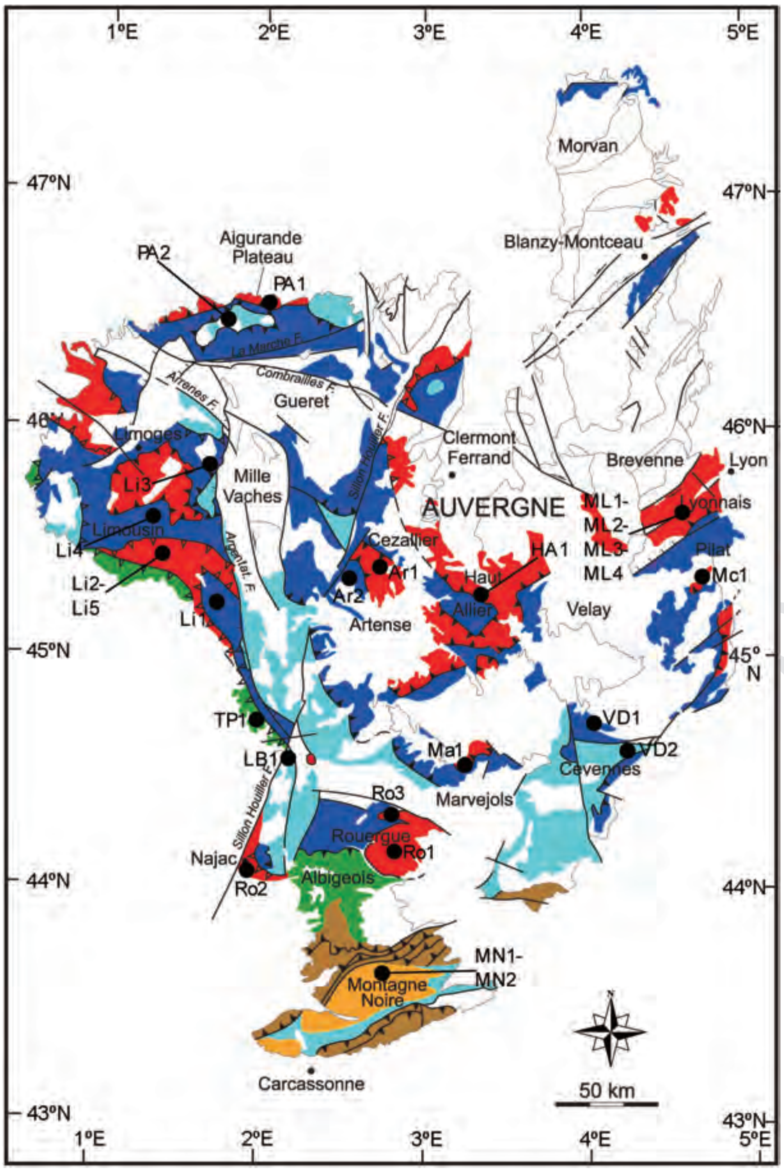

1ºE
2ºE
3ºE
4ºE
5ºE
47ºN
46ºN
45ºN
44ºN
43ºN
Morvan
Blanzy-Montceau
Aigurande
Plateau
PA2
PA1
La Marche F.
Combrailles F.
Arrenes F.
Gueret
Limoges
Li3
Mille
Vaches
Limousin
Li4
Li2-
Li5
Li1
Argentat F.
Sillon Houiller F.
Clermont
Ferrand
AUVERGNE
Brevenne
Lyon
Lyonnais
Pilat
ML1-
ML2-
ML3-
ML4
Mc1
Cezallier
Ar1
Ar2
Artense
HA1
Haut
Allier
Velay
TP1
LB1
Ma1
Marvejols
VD1
VD2
Cevennes
Ro3
Rouergue
Ro1
Najac
Ro2
Albigeois
MN1-
MN2
Montagne
Noire
Carcassonne
50 km

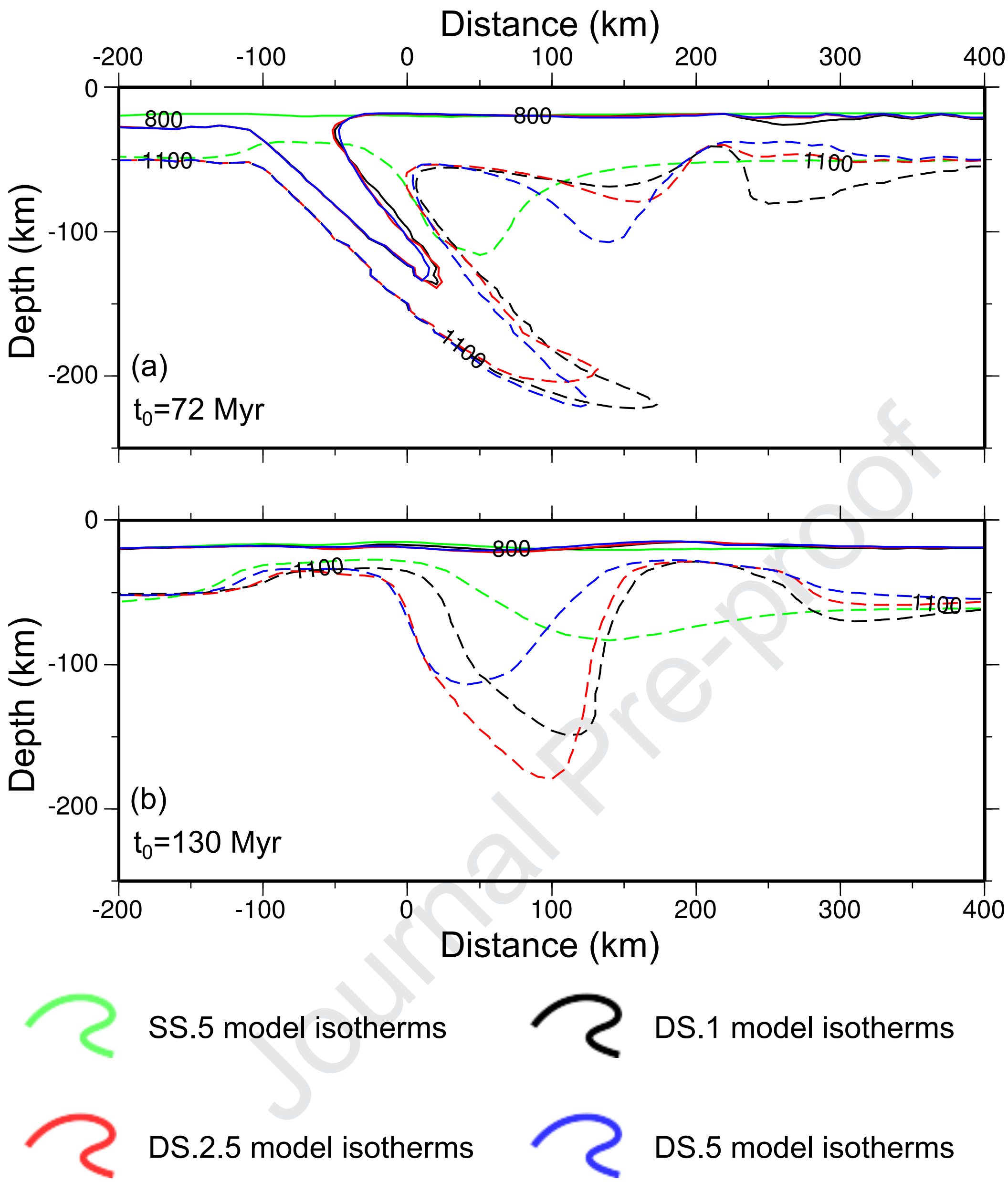
Distance (km)
-200
-100
0
100
200
300
400
0
-100
-200
Depth (km)
800
1100
(a)
t0=72 Myr
800
1100
(b)
t0=130 Myr
Distance (km)
SS.5 model isotherms
DS.1 model isotherms
DS.2.5 model isotherms
DS.5 model isotherms

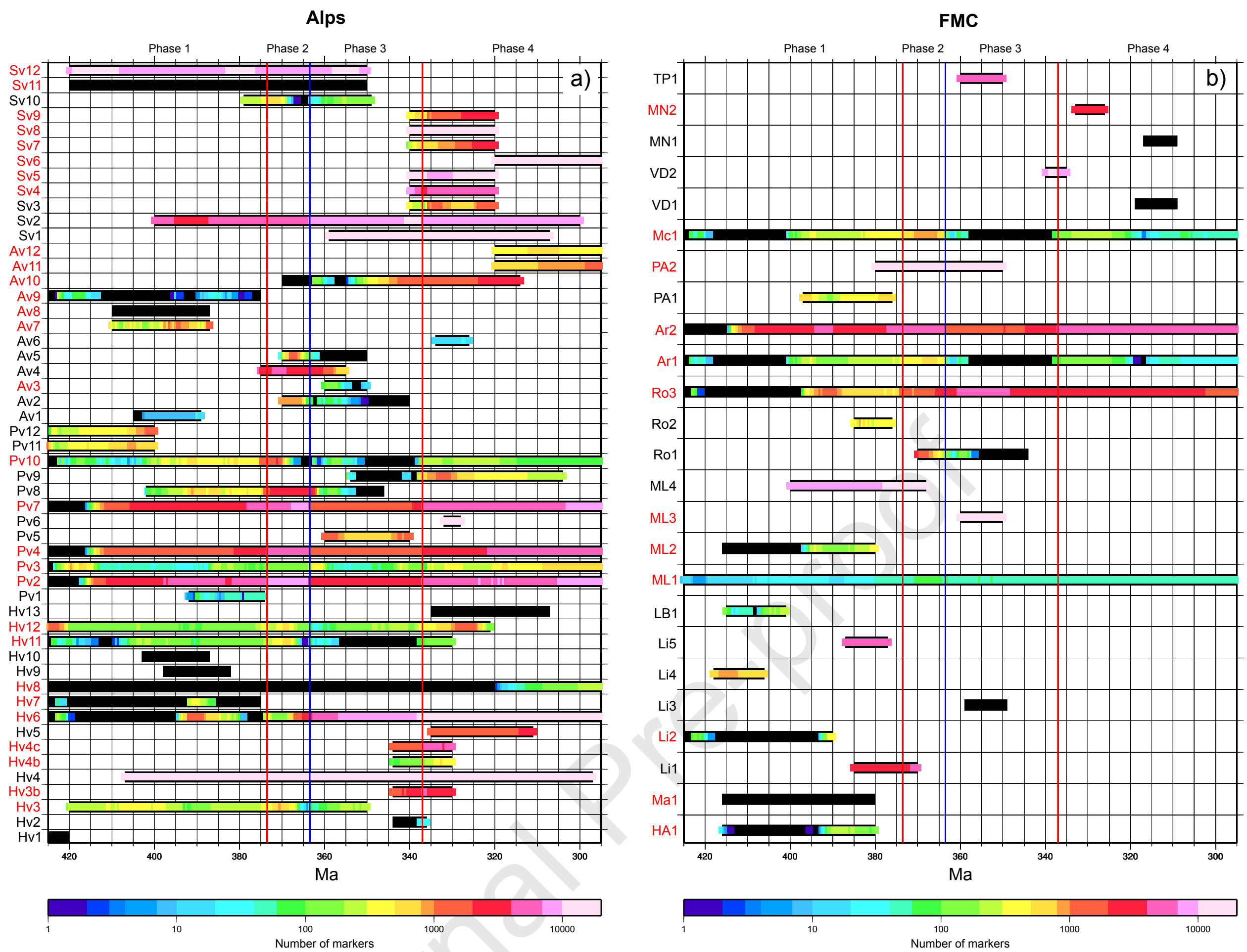
Alps
Phase 1
Phase 2
Phase 3
Phase 4
a)
Sv12
Sv11
Sv10
Sv9
Sv8
Sv7
Sv6
Sv5
Sv4
Sv3
Sv2
Sv1
Av12
Av11
Av10
Av9
Av8
Av7
Av6
Av5
Av4
Av3
Av2
Av1
Pv12
Pv11
Pv10
Pv9
Pv8
Pv7
Pv6
Pv5
Pv4
Pv3
Pv2
Pv1
Hv13
Hv12
Hv11
Hv10
Hv9
Hv8
Hv7
Hv6
Hv5
Hv4c
Hv4b
Hv4
Hv3b
Hv3
Hv2
Hv1
420
400
380
360
340
320
300
Ma
1
10
100
1000
10000
Number of markers
FMC
Phase 1
Phase 2
Phase 3
Phase 4
b)
TP1
MN2
MN1
VD2
VD1
Mc1
PA2
PA1
Ar2
Ar1
Ro3
Ro2
Ro1
ML4
ML3
ML2
ML1
LB1
Li5
Li4
Li3
Li2
Li1
Ma1
HA1
420
400
380
360
340
320
300
Ma
1
10
100
1000
10000
Number of markers

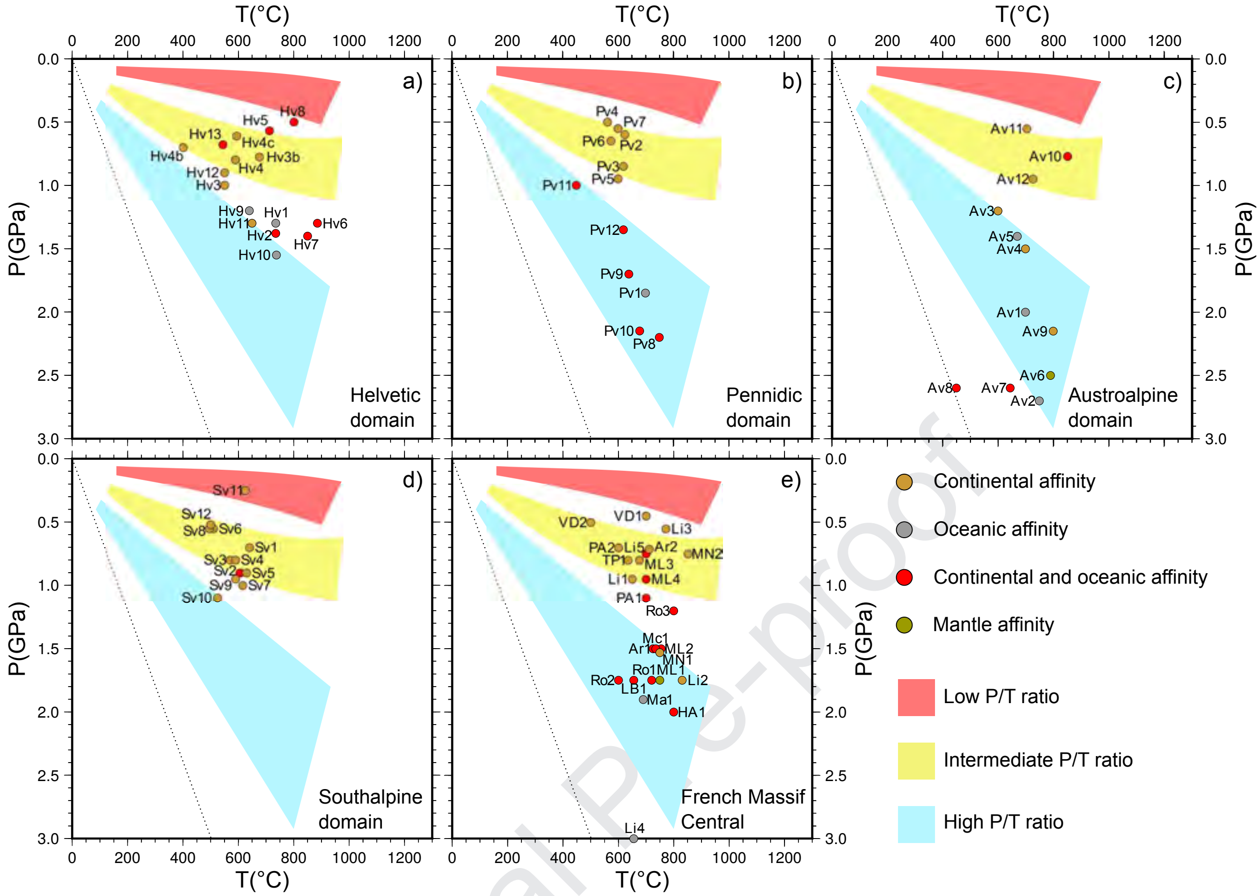
T(°C)
P(GPa)
a)
Helvetic domain
b)
Pennidic domain
c)
Austroalpine domain
d)
Southalpine domain
e)
French Massif Central
Continental affinity
Oceanic affinity
Continental and oceanic affinity
Mantle affinity
Low P/T ratio
Intermediate P/T ratio
High P/T ratio

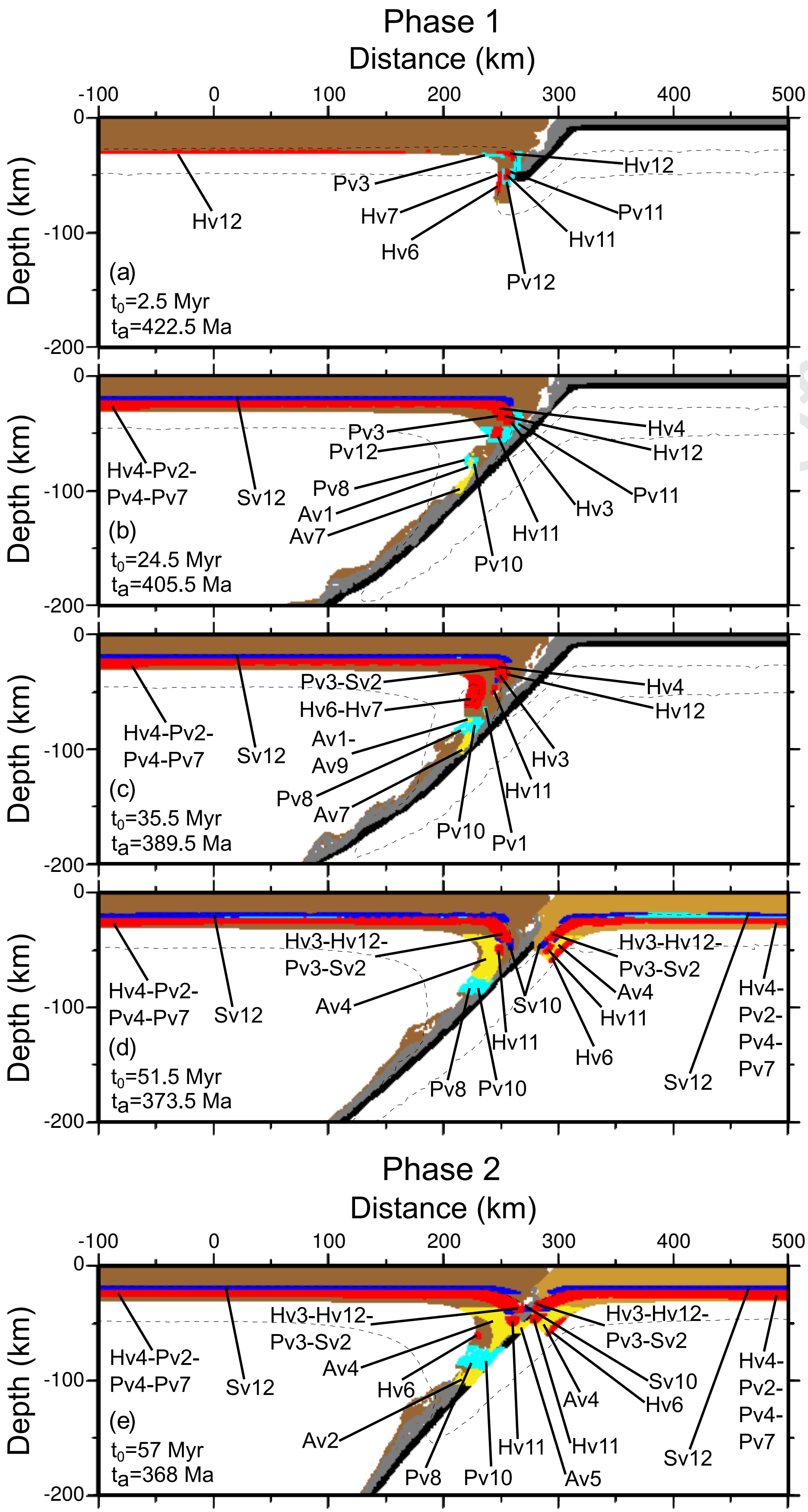
Phase 1
Distance (km)
-100
0
100
200
300
400
500
Depth (km)
0
-100
-200
Hv12
Pv3
Hv7
Hv6
Hv12
Pv11
Hv11
Pv12
(a)
t_0=2.5 Myr
t_a=422.5 Ma
Hv4-Pv2-
Pv4-Pv7
Sv12
Pv3
Pv12
Pv8
Av1
Av7
Hv4
Hv12
Hv3
Pv11
Hv11
Pv10
(b)
t_0=24.5 Myr
t_a=405.5 Ma
Hv4-Pv2-
Pv4-Pv7
Sv12
Pv3-Sv2
Hv6-Hv7
Av1-
Av9
Pv8
Av7
Hv4
Hv12
Hv3
Hv11
Pv10
Pv1
(c)
t_0=35.5 Myr
t_a=389.5 Ma
Hv4-Pv2-
Pv4-Pv7
Sv12
Hv3-Hv12-
Pv3-Sv2
Av4
Pv8
Pv10
Hv11
Sv10
Hv3-Hv12-
Pv3-Sv2
Av4
Hv11
Hv6
Sv12
Hv4-
Pv2-
Pv4-
Pv7
(d)
t_0=51.5 Myr
t_a=373.5 Ma
Phase 2
Distance (km)
Hv4-Pv2-
Pv4-Pv7
Sv12
Hv3-Hv12-
Pv3-Sv2
Av4
Hv6
Av2
Pv8
Pv10
Hv11
Hv3-Hv12-
Pv3-Sv2
Sv10
Hv6
Av4
Hv11
Av5
Sv12
Hv4-
Pv2-
Pv4-
Pv7
(e)
t_0=57 Myr
t_a=368 Ma

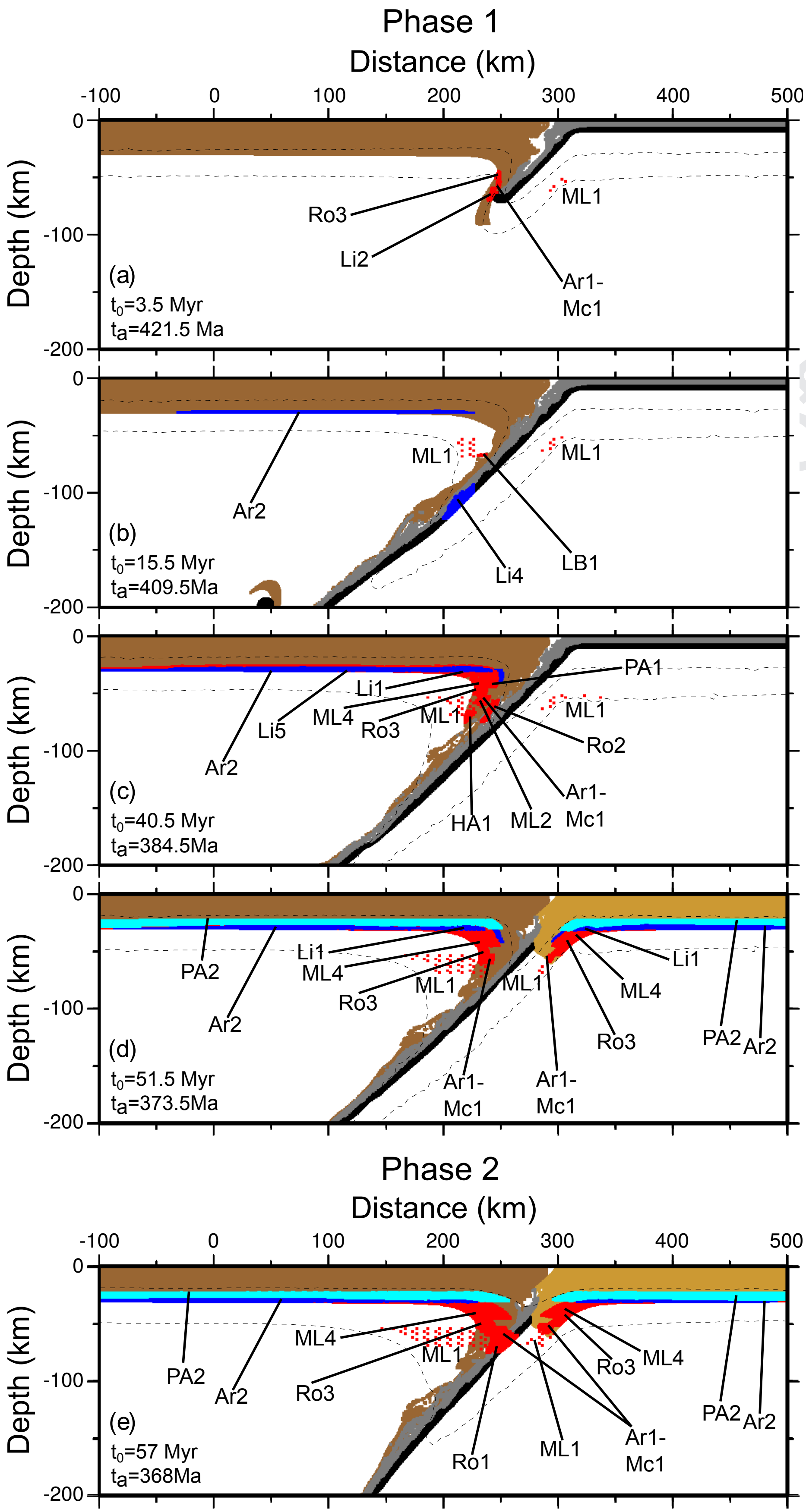

Phase 1
Distance (km)
Depth (km)
(a)
t_0=3.5 Myr
t_a=421.5 Ma
Ro3
Li2
ML1
Ar1-Mc1
(b)
t_0=15.5 Myr
t_a=409.5Ma
Ar2
ML1
Li4
LB1
(c)
t_0=40.5 Myr
t_a=384.5Ma
PA1
Li1
Li5
ML4
Ro3
ML1
Ro2
Ar2
HA1
ML2
Ar1-Mc1
(d)
t_0=51.5 Myr
t_a=373.5Ma
PA2
Li1
ML4
Ar2
Ro3
ML1
ML4
Ro3
PA2
Ar2
Ar1-Mc1
Phase 2
Distance (km)
Depth (km)
(e)
t_0=57 Myr
t_a=368Ma
ML4
ML1
PA2
Ar2
Ro3
Ro1
ML1
Ar1-Mc1
PA2
Ar2

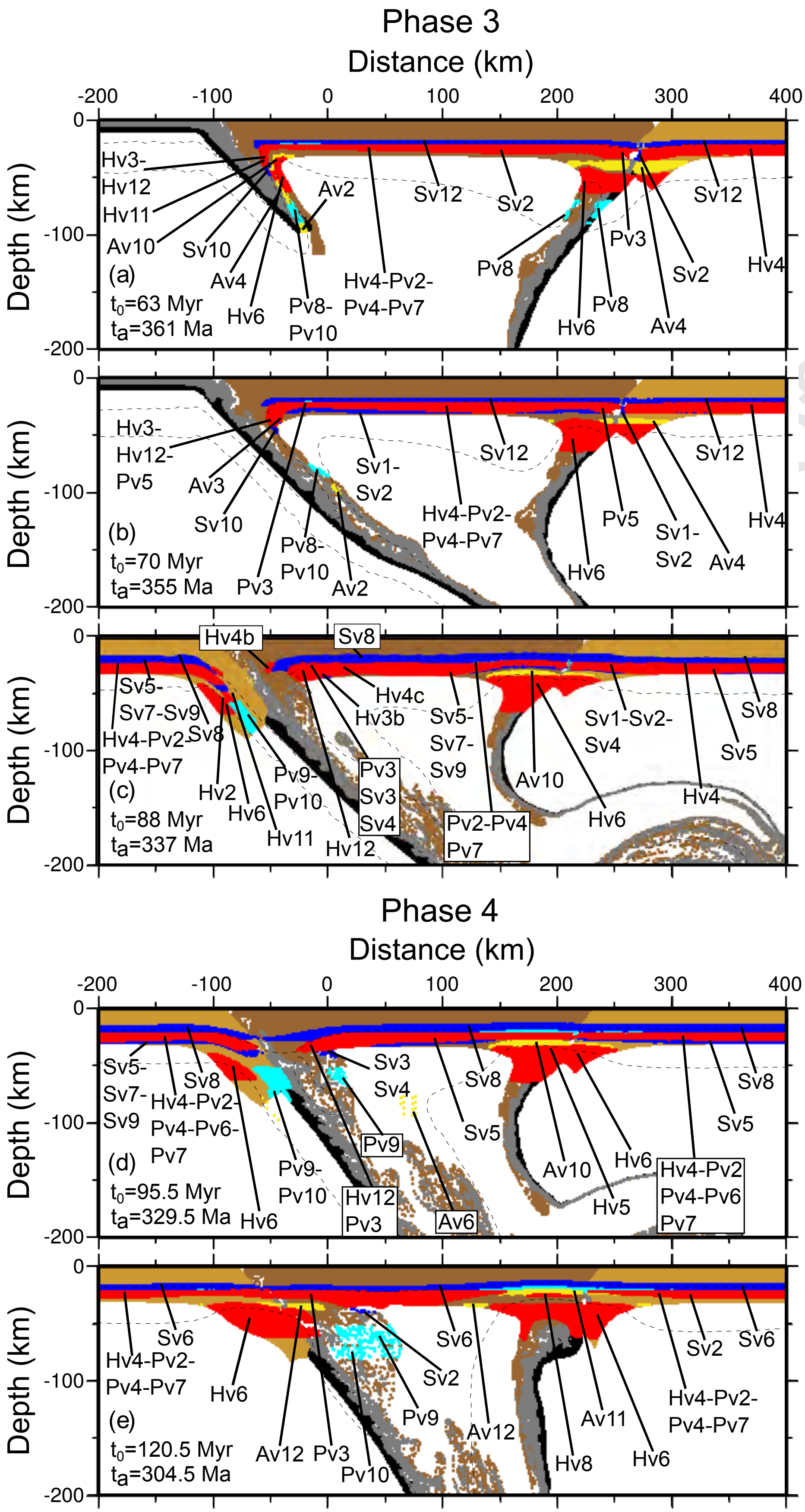
Phase 3
Distance (km)
-200
-100
0
100
200
300
400
Depth (km)
0
-100
-200
Hv3-
Hv12
Hv11
Av10
Sv10
Av4
Hv6
Av2
Pv8-
Pv10
Hv4-Pv2-
Pv4-Pv7
Sv12
Sv2
Pv8
Hv6
Pv8
Pv3
Av4
Sv2
Sv12
Hv4
(a)
t_0=63 Myr
t_a=361 Ma
Hv3-
Hv12-
Pv5
Av3
Sv10
Pv3
Pv8-
Pv10
Av2
Sv1-
Sv2
Hv4-Pv2-
Pv4-Pv7
Sv12
Hv6
Pv5
Sv1-
Sv2
Av4
Sv12
Hv4
(b)
t_0=70 Myr
t_a=355 Ma
Hv4b
Sv8
Sv5-
Sv7-Sv9
Hv4-Pv2-
Pv4-Pv7
Sv8
Hv2
Hv6
Hv11
Pv9-
Pv10
Hv12
Hv4c
Hv3b
Pv3
Sv3
Sv4
Sv5-
Sv7-
Sv9
Pv2-Pv4
Pv7
Av10
Hv6
Sv1-Sv2-
Sv4
Hv4
Sv5
Sv8
(c)
t_0=88 Myr
t_a=337 Ma
Phase 4
Distance (km)
Sv5-
Sv7-
Sv9
Sv8
Hv4-Pv2-
Pv4-Pv6-
Pv7
Hv6
Pv9-
Pv10
Hv12
Pv3
Sv3
Sv4
Pv9
Av6
Sv5
Sv8
Av10
Hv5
Hv6
Hv4-Pv2
Pv4-Pv6
Pv7
Sv5
Sv8
(d)
t_0=95.5 Myr
t_a=329.5 Ma
Sv6
Hv4-Pv2-
Pv4-Pv7
Hv6
Av12
Pv3
Pv10
Pv9
Sv2
Sv6
Av12
Hv8
Av11
Hv6
Hv4-Pv2-
Pv4-Pv7
Sv2
Sv6
(e)
t_0=120.5 Myr
t_a=304.5 Ma

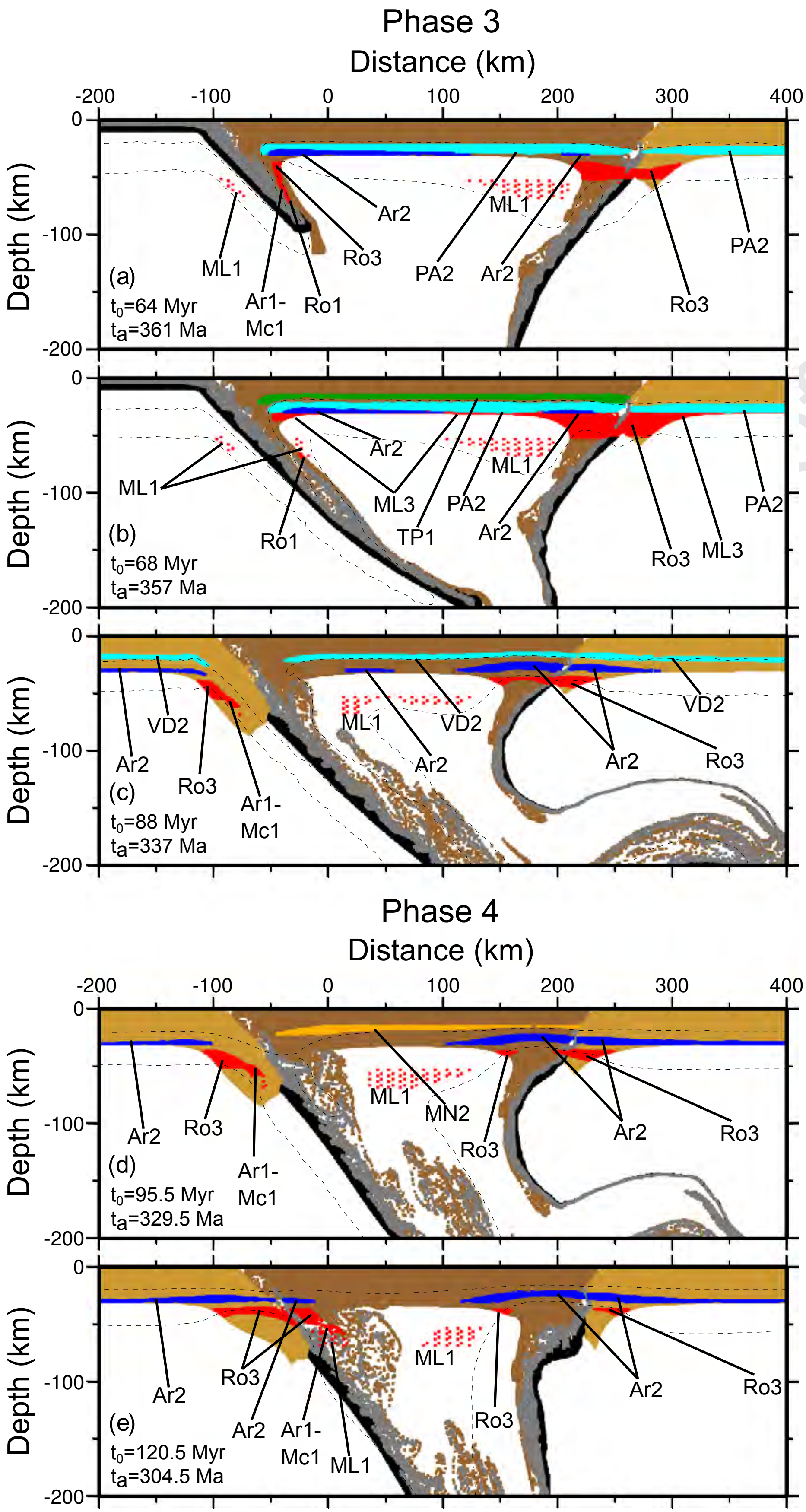
Phase 3
Distance (km)
-200
-100
0
100
200
300
400
Depth (km)
(a)
t_0=64 Myr
t_a=361 Ma
ML1
Ar1-
Mc1
Ro1
Ro3
Ar2
PA2
Ar2
ML1
Ro3
PA2
(b)
t_0=68 Myr
t_a=357 Ma
ML1
Ro1
Ar2
ML3
TP1
PA2
ML1
Ar2
Ro3
ML3
PA2
(c)
t_0=88 Myr
t_a=337 Ma
Ar2
VD2
Ro3
Ar1-
Mc1
ML1
Ar2
VD2
Ar2
Ro3
VD2
Phase 4
Distance (km)
(d)
t_0=95.5 Myr
t_a=329.5 Ma
Ar2
Ro3
Ar1-
Mc1
ML1
MN2
Ro3
Ar2
Ro3
(e)
t_0=120.5 Myr
t_a=304.5 Ma
Ar2
Ro3
Ar2
Ar1-
Mc1
ML1
ML1
Ro3
Ar2
Ro3

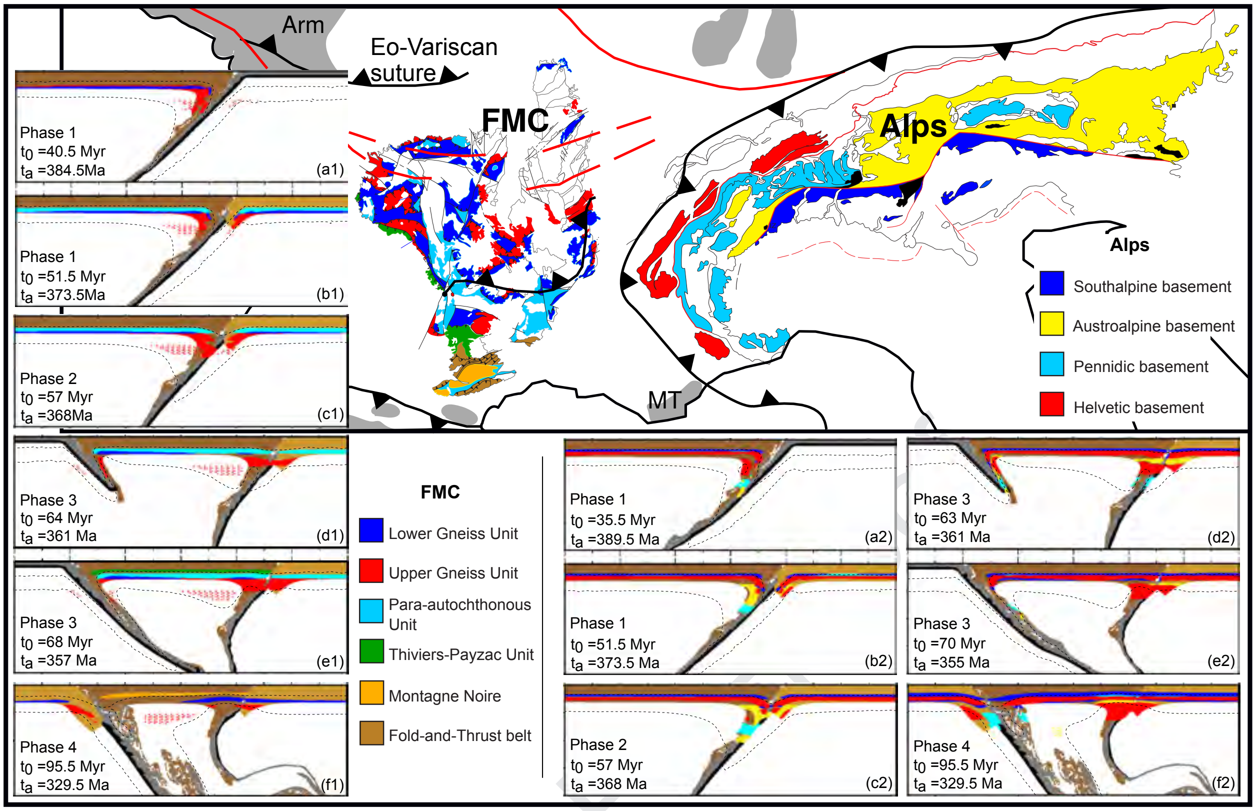
Arm
Eo-Variscan suture
FMC
Alps
MT
Alps
Southalpine basement
Austroalpine basement
Pennidic basement
Helvetic basement
FMC
Lower Gneiss Unit
Upper Gneiss Unit
Para-autochthonous Unit
Thiviers-Payzac Unit
Montagne Noire
Fold-and-Thrust belt
Phase 1 t_0 =40.5 Myr t_a =384.5Ma (a1)
Phase 1 t_0 =51.5 Myr t_a =373.5Ma (b1)
Phase 2 t_0 =57 Myr t_a =368Ma (c1)
Phase 3 t_0 =64 Myr t_a =361 Ma (d1)
Phase 3 t_0 =68 Myr t_a =357 Ma (e1)
Phase 4 t_0 =95.5 Myr t_a =329.5 Ma (f1)
Phase 1 t_0 =35.5 Myr t_a =389.5 Ma (a2)
Phase 1 t_0 =51.5 Myr t_a =373.5 Ma (b2)
Phase 2 t_0 =57 Myr t_a =368 Ma (c2)
Phase 3 t_0 =63 Myr t_a =361 Ma (d2)
Phase 3 t_0 =70 Myr t_a =355 Ma (e2)
Phase 4 t_0 =95.5 Myr t_a =329.5 Ma (f2)

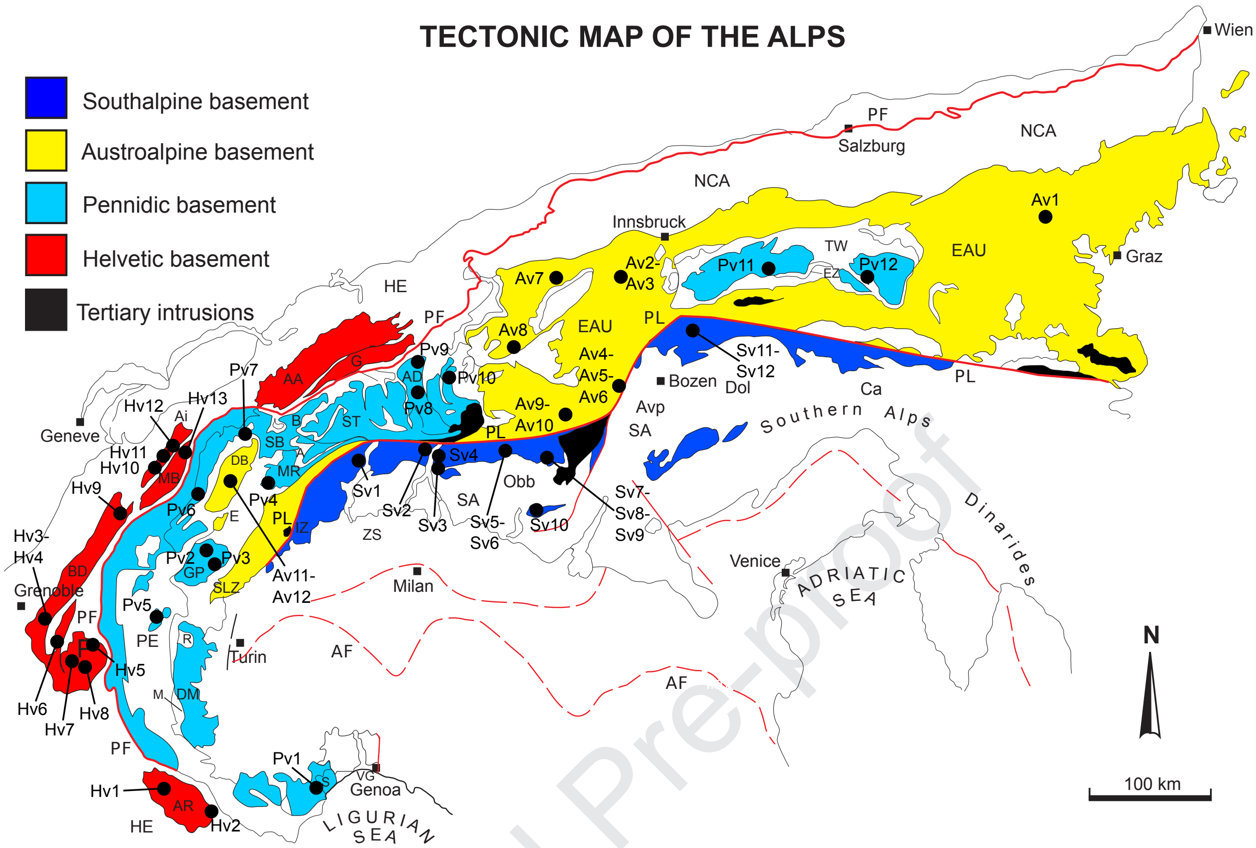
TECTONIC MAP OF THE ALPS
Southalpine basement
Austroalpine basement
Pennidic basement
Helvetic basement
Tertiary intrusions
Wien
PF
Salzburg
NCA
Innsbruck
Graz
TW
EAU
Av1
Av7
Av2-
Av3
Pv11
Pv12
HE
PF
Av8
EAU
PL
Sv11-
Sv12
Bozen
Dol
Ca
PL
Av4-
Av5-
Av6
Pv9
Pv10
AD
Pv8
G
AA
Pv7
Hv13
Hv12
Ai
Geneve
Hv11
Hv10
Hv9
ST
SB
B
DB
MR
Av9-
Av10
PL
Avp
SA
Southern Alps
Sv4
Sv1
Sv2
Sv3
Obb
SA
Sv5-
Sv6
Sv10
Sv7-
Sv8-
Sv9
Dinarides
Pv6
Pv4
PL
E
IZ
ZS
Hv3-
Hv4
Pv2
Pv3
GP
SLZ
Av11-
Av12
Milan
Venice
ADRIATIC SEA
Grenoble
BD
PF
Pv5
PE
R
Turin
AF
AF
Hv5
Hv6
Hv7
Hv8
DM
PF
Pv1
Genoa
Hv1
AR
Hv2
HE
LIGURIAN SEA
N
100 km

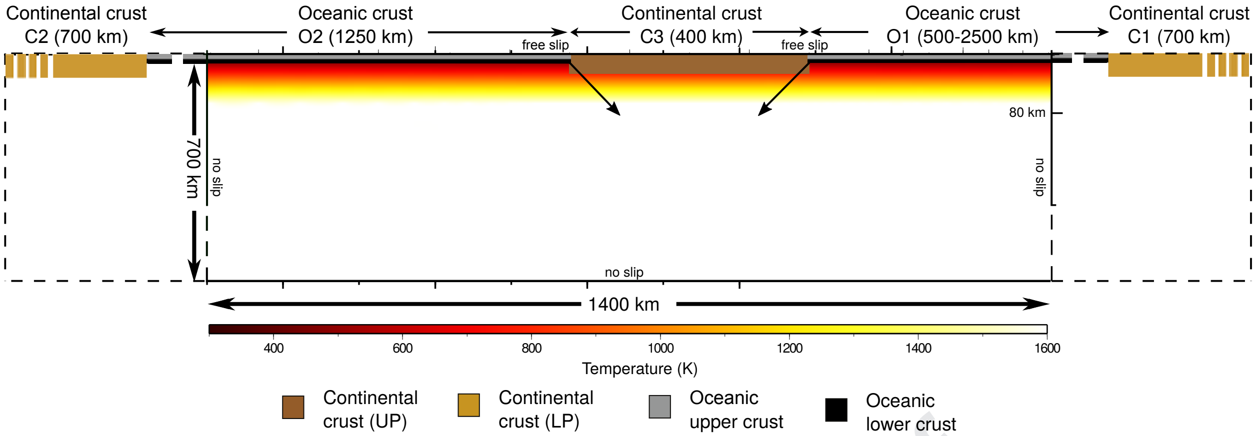

Model	DS.1	DS.2.5	DS.5	SS.5
Velocity - phase 1 (cm/yr)	1	2.5	5	5
Dimension of the ocean – phase 1 (km)	500	1250	2500	2500
Velocity - phase 3 (cm/yr)	5	5	5	-
Dimension of the ocean – phase 3 (km)	1250	1250	1250	-

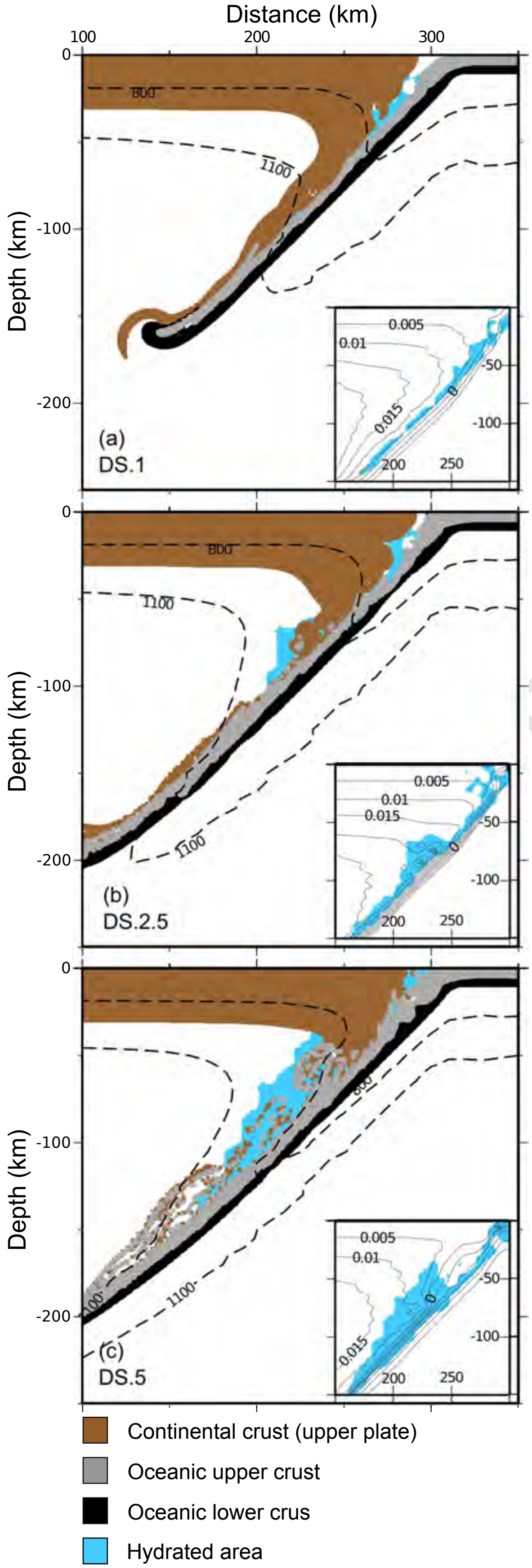
Distance (km)
100
200
300
Depth (km)
0
-100
-200
800
1100
0.005
0.01
0.015
-50
-100
200
250
(a)
DS.1
(b)
DS.2.5
(c)
DS.5
Continental crust (upper plate)
Oceanic upper crust
Oceanic lower crus
Hydrated area

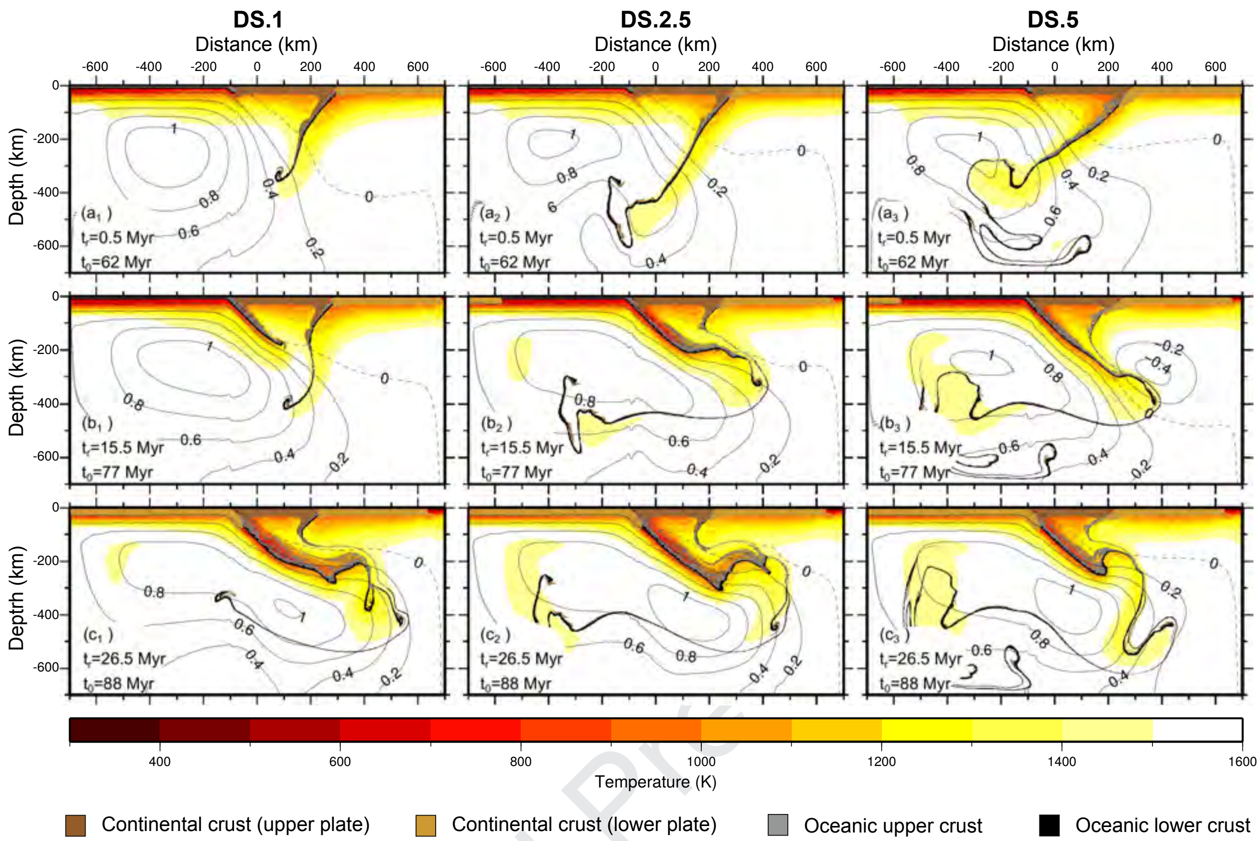

DS.1
DS.2.5
DS.5
Distance (km)
Depth (km)
(a1) t_r=0.5 Myr t_0=62 Myr
(a2) t_r=0.5 Myr t_0=62 Myr
(a3) t_r=0.5 Myr t_0=62 Myr
(b1) t_r=15.5 Myr t_0=77 Myr
(b2) t_r=15.5 Myr t_0=77 Myr
(b3) t_r=15.5 Myr t_0=77 Myr
(c1) t_r=26.5 Myr t_0=88 Myr
(c2) t_r=26.5 Myr t_0=88 Myr
(c3) t_r=26.5 Myr t_0=88 Myr
Temperature (K)
Continental crust (upper plate)
Continental crust (lower plate)
Oceanic upper crust
Oceanic lower crust

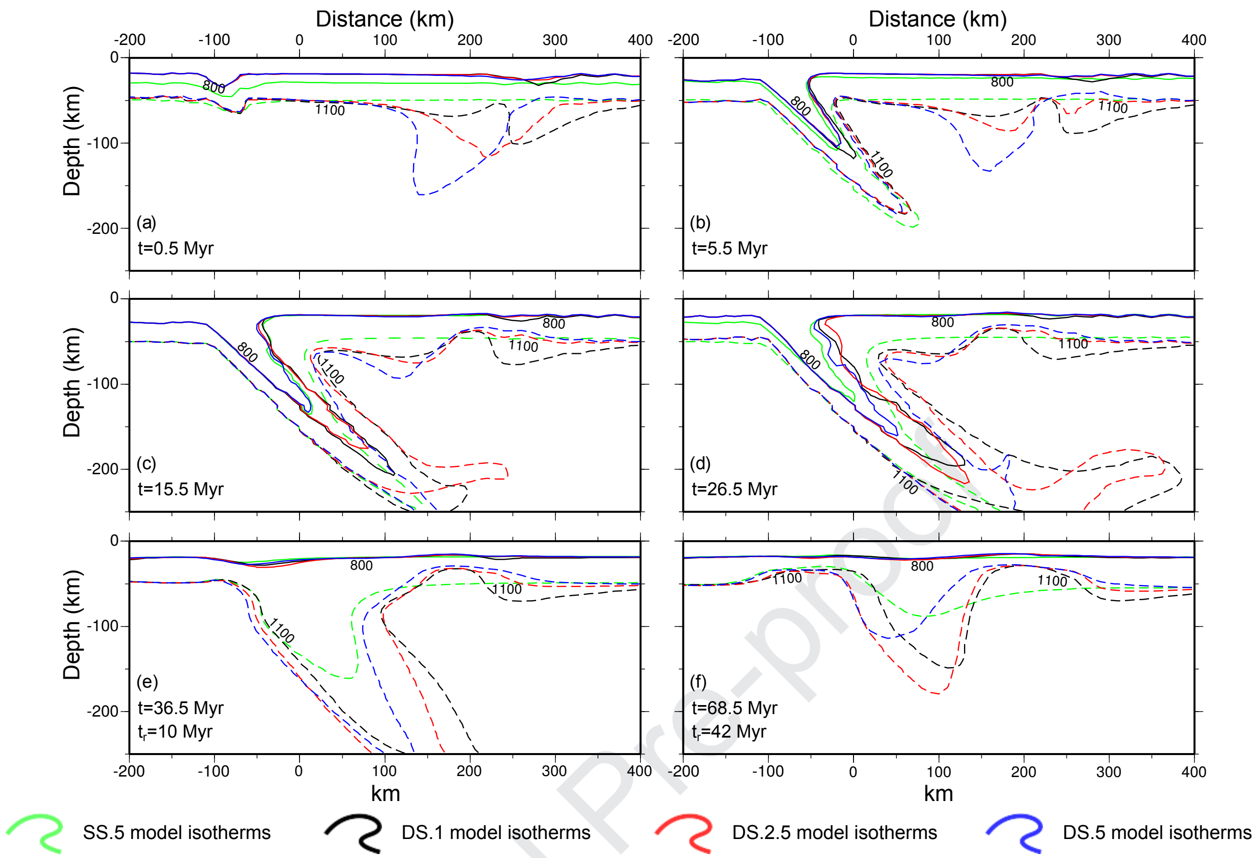

Distance (km)
Depth (km)
(a) t=0.5 Myr
(b) t=5.5 Myr
(c) t=15.5 Myr
(d) t=26.5 Myr
(e) t=36.5 Myr t_r=10 Myr
(f) t=68.5 Myr t_r=42 Myr
800
1100
km
SS.5 model isotherms
DS.1 model isotherms
DS.2.5 model isotherms
DS.5 model isotherms

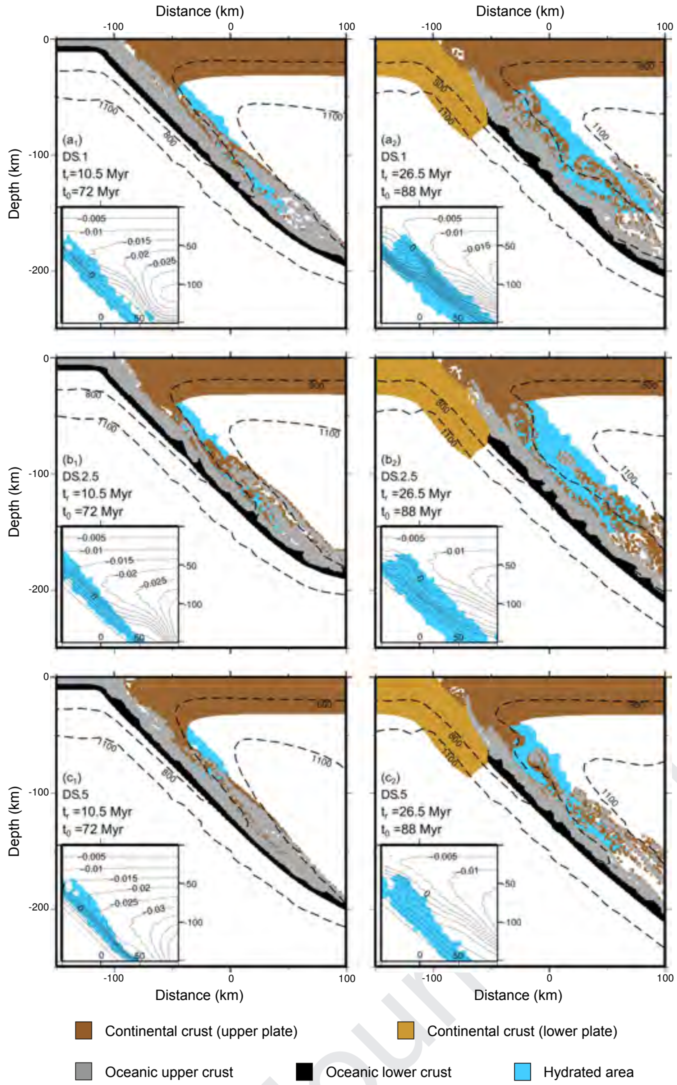

Distance (km)
Depth (km)
(a1) DS.1 tr=10.5 Myr t0=72 Myr
(a2) DS.1 tr =26.5 Myr t0 =88 Myr
(b1) DS.2.5 tr =10.5 Myr t0 =72 Myr
(b2) DS.2.5 tr =26.5 Myr t0 =88 Myr
(c1) DS.5 tr =10.5 Myr t0 =72 Myr
(c2) DS.5 tr =26.5 Myr t0 =88 Myr
Continental crust (upper plate)
Continental crust (lower plate)
Oceanic upper crust
Oceanic lower crust
Hydrated area

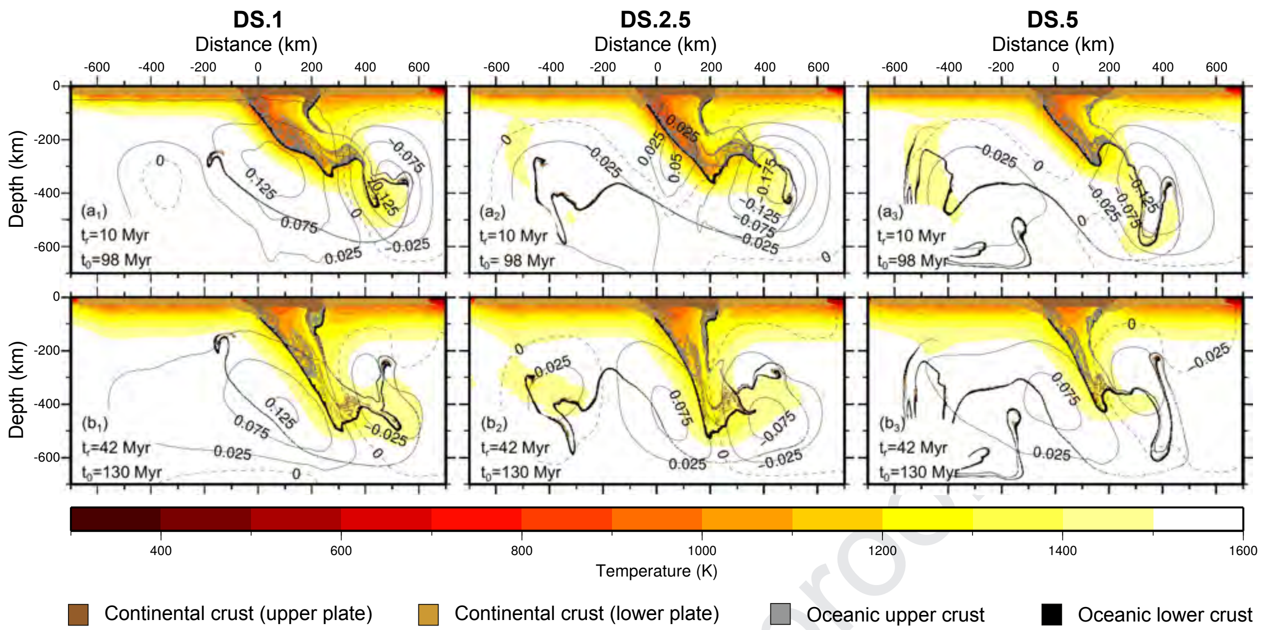

DS.1
DS.2.5
DS.5
Distance (km)
Depth (km)
(a1) tr=10 Myr t0=98 Myr
(a2) tr=10 Myr t0= 98 Myr
(a3) tr=10 Myr t0=98 Myr
(b1) tr=42 Myr t0=130 Myr
(b2) tr=42 Myr t0=130 Myr
(b3) tr=42 Myr t0=130 Myr
Temperature (K)
Continental crust (upper plate)
Continental crust (lower plate)
Oceanic upper crust
Oceanic lower crust

- In a double subduction complex, the second subduction is colder than the first
- Data from the Alps with high P/T ratios fit well with both hot and cold subductions
- Data from the French Massif Central have a better compatibility with hot subductions
- Polycyclic models better fit with Variscan data from the Alps
- Rocks from Upper Gneiss Unit could derive from the ablative erosion of the upper plate